Mechanics of 2D Material Thin Films with Applications to Health and Nanofabrication Technologies

by

Dong Li

B. Eng., Dalian University of Technology, 2014

M. Eng., Dalian University of Technology, 2017

M. Sc., Brown University, 2020

A dissertation submitted in partial fulfillment of the

requirements for the Degree of Doctor of Philosophy

in the School of Engineering at Brown University

Providence, Rhode Island

October 2021

This dissertation by Dong Li is accepted in its present form

by the School of Engineering as satisfying the

dissertation requirement for the degree of Doctor of Philosophy

Date _____ _____

Huajian Gao, Advisor

Recommended to the Graduate Council

Date _____ _____

Kyung-Suk Kim, Reader

Date _____ _____

Robert H. Hurt, Reader

Date _____ _____

Lei Wei, Reader

Approved by the Graduate Council

Date _____ _____

Andrew G. Campbell, Dean of the Graduate School

Curriculum Vitae

Dong Li obtained his B. Eng. Degree in Engineering Mechanics in June 2014 at Dalian University of Technology, and was then enrolled by Dalian University of Technology as a postgraduate student with entrance examination waiver. He was engaged in research on structural optimization and mechanics of bionic materials, and awarded the M. Eng. Degree in Solid Mechanics in June 2017. He started the Mechanics of Solids Ph.D. program at Brown University in September 2017. His research mainly focuses on mechanics of thin film systems as well as advanced functional fibers. He was awarded the transitional M. Sc. Degree in Engineering in May 2020 at Brown University.

Publications:

1. **Li, D.**, Wang, Z., Chen, M., Wei, L., Gao, H. Mechanics of controlled fragmentation in cold drawing. *Journal of the Mechanics and Physics of Solids*, Under review.
2. Castilho, C. J., **Li, D.**, Xie, Y., Gao, H., & Hurt, R. H. (2021). Shear failure in supported two-dimensional nanosheet van der Waals thin films. *Carbon*, 173, 410-418.
3. Castilho, C. J., **Li, D.**, Liu, M., Liu, Y., Gao, H., Hurt, R. H. (2019). Mosquito bite prevention through graphene barrier layers. *Proceedings of the National Academy of Sciences*, 116(37), 18304-18309.

Acknowledgements

First, I would like to thank my advisor during my PhD program, Prof. Huajian Gao, who provided me so much help and guidance in my research in the last few years. I have learned a lot from Prof. Gao, on aspects not only of academic research, but also of the attitude to life and dealing with people. He is so wise and brilliant that a few words can point out the key to problems that puzzle me for a long time. He is always mild to people and has the magic to make students feel encouraged yet relaxed in the group.

I also acknowledge the members of my dissertation committee, Prof. Kyung-Suk Kim, Prof. Robert H. Hurt and Prof. Lei Wei, who spent time reading my dissertation manuscript and provided valuable advice. Prof. Hurt and Prof. Wei also gave me many useful suggestions and comments in our previous collaborations. Besides, I have benefitted a lot in my research from the discussions with our group members at Brown University and at Nanyang Technological University when I was visiting Singapore. Special thanks go to Cintia Castilho, Muchun Liu and Yiheng Xie who did the experiment parts, as well as Bin Ding, Bo Ni, Yue Liu, and Zhixun Wang who provided significant help and discussion to the works in this dissertation.

I want to thank the faculty in the School of Engineering at Brown University for giving courses and lectures where I learned so much useful knowledge, and thank all the staff who provided excellent service and guidance to my PhD program.

Finally, I would like to express my deepest gratitude to my parents and my fiancée for their support and accompany all the time in the past years. All my achievements and awards were due to their encouragement and assistance.

I dedicate this dissertation to my Parents and Dear Fiancée.

Table of Contents

List of Tables

List of Figures

Chapter 1 Introduction

Materials with submicron or nanoscale dimensions exhibit superior electronic, magnetic, chemical and mechanical properties, benefitting from their large surface-to-volume ratios, the quantum size effects and the limitation on defect size [1, 2]. Various advanced nanomaterials characterizing minute feature sizes can play essential roles in the development of intelligent wearable devices with specific functions. Low dimensional materials are a broad class of nanomaterials with extremely reduced sizes in some dimensions, represented by zero-dimensional nanoparticles, one-dimensional (1D) carbon nanotubes and two-dimensional (2D) materials. In this dissertation, mechanical behavior of 2D material thin films in applications targeting functional wearable devices will be focused. Theoretical modeling and numerical simulation investigations will be conducted to understand the mechanics of these film systems together with existing experiment results.

Two-dimensional materials, the ultrathin layers of atomic lattice with thickness of single or a few atoms, have experienced a global research boom since the seminal research on graphene in 2004 [3], highlighted by the 2010 Nobel Prize in Physics to Geim and Novoselov "for groundbreaking experiments regarding the two-dimensional material graphene". With great potential future in broad fields including physics, chemistry, biology, medicine, mechanics and electronics [4-9], 2D materials have now grown into a large family consisting of hundreds of members with various atomic structures, chemical compositions and physical properties. Different synthesis approaches have been developed for 2D materials, such as micromechanical exfoliation, ultrasonic exfoliation and chemical vapor deposition (CVD). These 2D materials are exploited in more and more practical applications,

including energy storage [10, 11], flexible electronics [12], semi/super-conductors [13, 14] and water purification [15-17].

1.1 2D Material Thin Films

Monolayer and multilayer 2D materials are both typical thin film systems. For example, monolayer graphene is a membrane with single-atom thickness, composed of sp^2 hybridized carbon atoms within hexagonal lattice (Fig. 1.1a); monolayer hexagonal boron nitride (hBN) is also single-atom thick, but each boron atom is surrounded by three nitrogen atoms and vice versa (Fig. 1.1b); whereas monolayer transition metal dichalcogenide (TMD, e.g., MoS_2, $MoSe_2$) has a staggered structure with the metal atom plane sandwiched by two chalcogen atom planes (Fig. 1.1c). Atoms in the monolayer 2D materials are covalently bonded, leading to large in-plane stiffness and strength. The out-of-plane stiffness, however, is much smaller due to extremely small thickness and weak interlayer interaction.

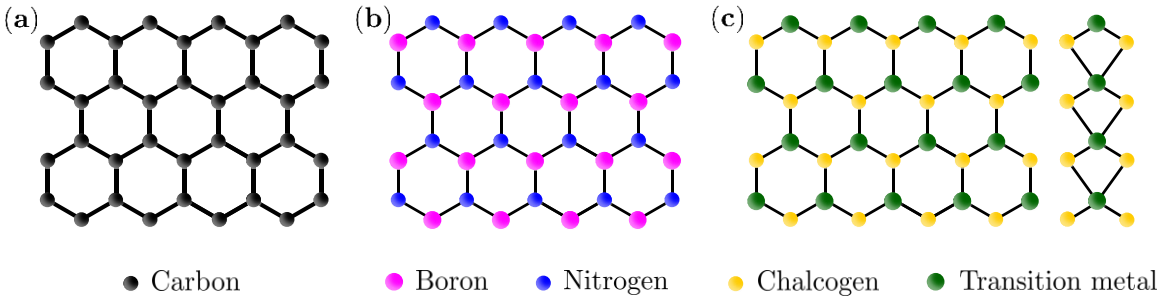

Fig. 1.1. Atomic structure of different 2D material monolayers. (**a**) Graphene. (**b**) Hexagonal boron nitride. (**c**) Transition metal dichalcogenide. Left: top view; right: side view.

The out-of-plane bending stiffness can be enhanced by stacking multiple monolayers in the normal direction. The 2D nanosheets are linked mainly by van der Waals (vdW)

interaction which is much weaker than covalent bonds. The multilayer 2D material thin films of mm-level or above sizes contain large number of monolayers not only in the out-of-plane direction but also in the in-plane directions (Fig. 1.2a). For example, GO thin film, which is the first reported paper-like 2D material thin film, consists of hundreds to thousands of stacked GO nanosheet layers with the brick-and-mortar structure (Fig. 1.2b) [18]. Limited by the current preparation techniques, the stacking order is always random and uncontrolled. The intralayer interactions are also dominated by vdW force, whereas small amount of covalent bonds and hydrogen bonds exists between the edges of neighbor nanosheets in some 2D material thin films.

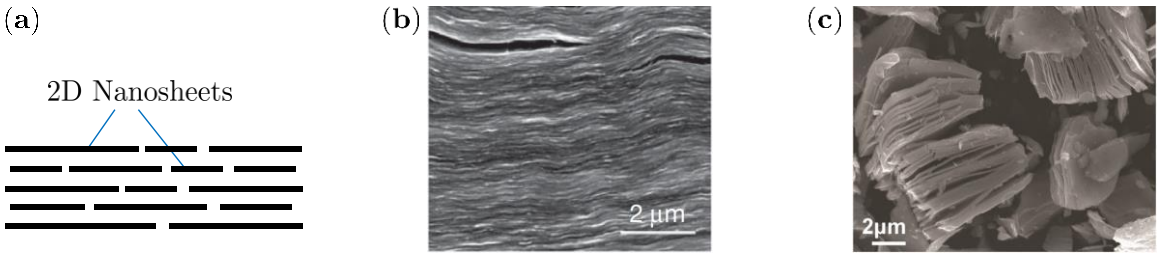

Fig. 1.2. Microscopic structures of multilayer 2D material thin films. (**a**) Schematic diagram. (**b**) GO [18]. (**c**) exfoliated Ti_2CO_x [23].

Multilayer 2D material thin films also include those with only a few layers in the normal direction. Compared with the monolayer counterparts, some interesting behavior like stick-slip shear [19], Moiré pattern [20] and superconducting magic angle [14] may occur in few-layer systems. However, these systems are not the objective of the research in this dissertation, and multilayer 2D material thin films ONLY refer to the paper-like films with many layers in thickness, unless stated otherwise.

Multilayer 2D material thin films usually inherit superior mechanical properties of their monolayer building blocks and particularly exhibit outstanding in-plane stiffness and strength. Benefiting from the excellent properties of GO monolayers as well as the interlocked laminate structure, the average tensile modulus and fracture strength of GO thin films can reach 32GPa and 120MPa, respectively, outperforming many conventional thin film materials [18]. Other examples of 2D material thin films include graphene film, reduced GO (rGO) film, MXene film and MoS_2 film, each possessing its own advantageous properties. For example, graphene thin film is intrinsically hydrophobic and resistant to water intercalation into the gallery between graphene nanosheets, resulting in strong stability in water solutions [6, 21]; MXene thin films (Fig. 1.2c) are transition metal carbides, nitrides, or carbonitrides layers that combine metal conductivity and hydrophilicity [11, 22, 23]. Compared with the strict requirements of high-quality 2D monolayers synthesis on defect density and crystal growth control, properties of multilayer 2D material thin films are insensitive to defects and grain boundaries in nanosheets and thus they can be produced at lower costs and in larger scale.

1.2 Synthesis Methods

Since graphene was first prepared through mechanical cleavage in 2004 [3], a wide variety of synthesis methods have been developed. As more and more types of 2D materials are discovered, some synthesis methods are designed to target some specific types of 2D materials, while others are found to be much more general. Although each method has its merits, unfortunately, no “perfect” method has been found to produce high-quality, high-purity and large-area monolayer 2D materials in low cost and large scale. Nevertheless,

remarkable advances have been made in the past years and new methods are still emerging to satisfy different requirements and resolve different issues in 2D material synthesis.

Multilayer 2D material thin films can be prepared by assembling 2D monolayers in some standard ways. Generally, the production of multilayer films is easier to enlarge, even to the industry scale, compared with that of monolayer films.

1.2.1 Synthesis of 2D Monolayers

As to 2D monolayers, the synthesis of graphene might be the one that has attracted the most attention and is investigated most widely. Synthesis methods for graphene can be divided into two classes: top-down and bottom-up methods [24, 25], according to the strategy transferring carbon precursors into graphene monolayers (or few layers). The top-down methods start from carbon assemblies such as graphite (graphene layers stacked and assembled by vdW force) and create delamination between nanosheets, while the bottom-up methods deposit carbon atoms onto a substrate to form graphene.

The top-down methods mainly include graphite exfoliation path and graphene oxide (GO) reduction path by mechanical, chemical, thermal or electrochemical means. The earliest method adopted by Geim and Novoselov uses scotch tape to cleavage graphitic planes from graphite [3]. This mechanical exfoliation can be repeated until monolayer graphene is obtained on the tape. The graphene flakes obtained by this method show strong electric field effect and high mobility in room temperature. However, mechanical exfoliation cannot control the layer numbers of resulting graphene precisely, and the production yield is low. A more efficient mechanical exfoliation method is taking advantage of large shear force produced by high blending shear rate ($>10^{-4}s^{-1}$) in stabilizing liquids [26], which is simple and easy to scale up. The problems are the decreasing yield with shear rate and

the limited sizes of the resulting nanosheets. A similar strategy is breaking up the interlayer interaction by sonication [27], which is usually conducted in suitable solvent and also known as liquid phase exfoliation (LPE). After sonication, the graphene nanosheets tend to re-stack together due to the vdW force. Surfactants or dispersing agents can be therefore added to avoid the re-stacking [28]. Besides, other exfoliation methods include chemical exfoliation (by intercalating alkali metal ions between nanosheets) [29], supercritical fluid exfoliation (by intercalating supercritical fluid such as supercritical CO_2) [30] and electrochemical exfoliation (by applying voltage to dissolve graphite) [31].

The alternative approach to mechanical cleavage is to reduce graphene oxide (GO) to obtain graphene nanosheets. Graphene oxide powders are composed of nanosheets with the same structure to graphene nanosheets except that a large amount of oxygen-containing functional groups exist on the surfaces of GO nanosheets. Due to the functional groups, the interlayer spacing in GO can be larger than that in graphene and the stacked assembly is easier to be exfoliated by sonication. Reducing agents like ascorbic acid [32] can be used to reduce GO in solvent, or alternatively, the reduction can be achieved by thermal modification [33]. While the reduction method is easy to operate and scale up, high-purity graphene nanosheets without functional groups are difficult to obtain. In addition, some surface defects may be introduced during the reduction process.

There are some other top-down methods to synthesize graphene monolayers, such as pyrolysis method which produces graphene by pyrolyzing the solid solvothermal product of sodium and ethanal [34]. Basically, top-down methods are appropriate for large-scale production of graphene without high requirements on the crystalline structure control and microscale defects.

The bottom-up methods to synthesize graphene mainly include chemical vapor deposition (CVD) and epitaxial growth. The CVD method uses gas-phase carbon precursors which are prone to adsorb onto the surface of transition metal substrate, such as nickel [35] and copper [36] substrates, where carbon atoms will dissolve and diffuse into the metal in high temperatures above the melting point. Upon decreasing the temperature to lower the solubility of the metal, carbon atoms will precipitate out and deposit on the surface to form single-layer or few-layer graphene. Large-area, single-crystal graphene can be obtained with CVD method, but the synthesis process must be operated in high vacuum, making the CVD method expensive. The epitaxial growth method uses silicon carbide (SiC) substrate as the carbon source [37]. The SiC substrate is heated to a high temperature in vacuum until SiC decomposes. With subsequent annealing, silicon atoms will form a thin layer between the substrate and the carbon atoms that form the graphene layers. The epitaxial growth method can produce graphene that remains good electronic properties, yet it suffers the same problem in cost.

The other 2D materials, excluding graphene, can be classified as elemental, binary, ternary and multi-element molecules. Synthesis methods of elemental 2D materials such as borophene (boron monolayer), silicene (silicon monolayer), germanene (germanium monolayer), stanine (tin monolayer) and phosphorene (phosphorous monolayer) vary according to the physical and chemical properties of the element as well as the selected precursor types. The common strategies include mechanical cleavage, physical vapor deposition (PVD), CVD [38] and epitaxial growth [39]. Transition metal dichalcogenides (TMD), regarded as good platforms to explore semiconductor physics, are a typical class of binary 2D materials, and have been reported to be synthesized by molten-salt-assisted

CVD [40] and epitaxial growth [41, 42]. Another representative binary 2D material, hexagonal boron nitride (hBN), has been synthesized through exfoliation methods [43, 44], CVD [45] and epitaxial growth [46]. Ternary TMD (e.g., $Mo_xW_{2-x}S_2$, $Cr_2Ge_2Te_6$) and metal phosphorous trichalcogenides (MPT, e.g., $MnPS_3$, $CrPS_4$) are mainly prepared using CVD [47] and chemical vapor transport (CVT) methods [48, 49]. MXenes are also ternary 2D materials and their synthesis usually adopts a strategy of selectively etching out some layers in the MAX phase precursor [22], where "M" denotes an early transition metal, "A" a group IIIA or IVA element, and "X" the carbon or nitrogen. Alternatively, preparation of ternary MXene has also been explored using CVD [50]. By comparison, the synthesis of multi-element 2D materials are underexplored. Notwithstanding, there are works showing that some multi-element 2D materials can be effectively prepared by CVD [40].

1.2.1 Preparation of Multilayer 2D Thin Films

Synthesized 2D monolayers are usually deposited on substrates or dispersed in liquid or solvent, whereas multilayer 2D material thin films composed of hundreds to thousands of monolayers in thickness direction can be fabricated into freestanding devices. Dmitriy et al. first proposed flow-directed assembly of GO nanosheets to prepare paper-like GO thin films [18]. The interlocking-tile structure of GO nanosheets makes the film outperform many other thin film materials in stiffness (32GPa in average) and strength (~120MPa). Since then, a wide variety of multilayer 2D material thin films have been prepared and studied. For example, reduced graphene oxide (rGO) thin films with thickness of about 6.5μm were obtained by reducing the prepared GO paper with HI and acetic acid [51]; the hBN thin films with thickness from 10μm to 100μm were produced by vacuum filtration of the hBN solution prepared by liquid exfoliation [52]. Besides, introducing functional

groups in the nanosheets in multilayer 2D thin films can be of interest in improving thermal or chemical properties of the films [17, 53].

The approaches to preparing multilayer 2D material thin films mainly include drop-casting, spin-coating and vacuum filtration. The drop-casting method is simple and easily operated. Some amount of 2D material solution is dropped onto the substrate and heated to evaporate the water, forming films with micron-sized thickness [54]. However, one problem in this method is that the film thickness is not strictly uniform after the film is dried, due to the "coffee ring" effect that causes thicker edges of a dried coffee drop. Appropriate selection of the substrate may alleviate this effect by suppressing the concentration of nanosheets on the edge [55]. In the spin-coating method, 2D material nanosheet solutions are spin-coated in high spinning speed for $0.5\sim2\text{mins}$ and dried in an oven in appropriate temperature [56, 57]. This method can prepare films with small thickness and high uniformness. The vacuum filtration method uses nanoporous membrane to filtrate 2D material solutions based on that the liquid can permeate through the membrane while 2D nanosheets are obstructed ending up with forming a thin film [58]. In this method, the thickness of the resulting film can be precisely controlled by both the solution concentration and filtration volume. Apart from the methods mentioned above, spray-coating [59] and dip-coating [60] are also used to prepare large-area 2D material thin films.

During the preparation process, introducing ions, molecules and micro-components as crosslinkers into multilayer 2D material thin films is a significant and effective tool to tune mechanical properties of the film. For example, a small amount of divalent alkaline earth metal ions (Mg^{2+} and Ca^{2+}) can tightly bind to carboxylic acid groups at the edges of 2D nanosheets and effectively enhance the strength of the thin film [61]. This strategy needs

the participation of oxygen-containing functional groups and can be readily applied to GO and MXene films. Alternatively, polymer can induce esterification reactions which create strong crosslinks between nanosheets. There are many options for polymer crosslinkers such as poly(vinyl alcohol) (PVA) [62]. An important parameter that influences crosslinking is the length of the polymer chain, as too short chains may not bridge adjacent nanosheets while too long chains cannot induce sufficient esterification [63]. Furthermore, one-dimensional (1D) materials (e.g., carbon nanotube, silver nanowire) can be introduced to reinforce 2D nanosheet films through shear interaction and entanglement forces [64, 65]. This strategy does not necessarily require functional groups on the basal plane of nanosheets and can be applied to a broad variety of 2D materials including rGO films.

1.3 Mechanical Test and Modeling

Mechanical characterization of 2D material thin films is the primary concern of engineers when these films are used in applications with complicated and extreme mechanical environments such as flexible electronic devices, ion sieving (desalination) and strain sensors. The performance of 2D monolayers is basically determined by their elastic modulus, failure strength and fracture toughness, whereas multilayer thin films also need to bear shear loading and interfacial interaction in some cases. Some common tests for characterizing mechanical properties of 2D material thin films will be discussed in this section.

1.3.1 Uniaxial Tension Test

Uniaxial tension test is the simplest and most basic one to measure elastic modulus and fracture properties of a specimen in engineering. When applied to ultrathin 2D materials, however, the usual uniaxial tension tester is difficult to firmly grip the thin films. Besides,

due to the small dimensions of 2D material specimen, testers of high precision in measuring film deformation and reaction force are also required.

To characterize fracture behavior of graphene, Zhang et al. used a homemade platform consisting of a micromechanical device and a nano-indenter to apply tensile loading on the graphene sample with a central pre-crack cut by focused ion beam (FIB) [66]. The testing process can be closely monitored by real-time scanning electron microscope (SEM) observation. The test results show that classic Griffith fracture theory can be applied to the brittle fracture of graphene, and the measured fracture toughness and facture energy of graphene are $K_{Ic} = 4.0\text{MPa}\sqrt{\text{m}}$ and $G_c = 15.9\text{Jm}^{-2}$, respectively. Although the film used in this work was bilayer graphene, the measured results are expected to be consistent with those for monolayer graphene due to the weak interlayer interaction. Cao et al. used a push-to-pull micromechanical device to test intact single-crystal graphene monolayer (without pre-crack) synthesized by CVD [67]. The measured Young's modulus is about 1TPa which is close to the theoretical limit, with high fracture tensile strength $50\sim60\text{GPa}$ and wide elastic strain up to $\sim6\%$. These results indicate that large-area single-crystal graphene, even with edge defects, can display near ideal mechanical performance. With the similar experimental devices, researchers also tested Ag nanowire/graphene hybrid films [68] and multilayer graphene films ($10\sim1000$ layers) [69]. The fracture strength of multilayer graphene films is found to decrease with film thickness, presumably resulting from increasing number of defects and the weak interfacial interaction between graphene nanosheets.

1.3.2 Bulge Test

Bulge test, also known as blister test, is a method to measure mechanical properties of homogeneous thin films in tension, such as Young's modulus, Poisson's ratio, adhesion

energy and residual stresses (eigenstress). In bulge test, uniform pressure (gas/liquid pressure) is applied on a thin film window over a hole in substrate (Fig. 1.3a, b). The deflection of the thin film approximately obeys power laws with respect to the applied pressure. Mechanical properties of the thin film can be obtained by fitting experiment data based on the known scaling laws. In contrast to the uniaxial tension test, the bulge test measures averaged in-plane properties of the thin film and is usually applied to homogeneous materials. For ultrathin films, especially 2D monolayers, the gripping problem in uniaxial tension test will no longer be a concern in the bulge test, since the interfacial adhesion is much larger than film bending stiffness (per volume) so that interfacial sliding can be neglected.

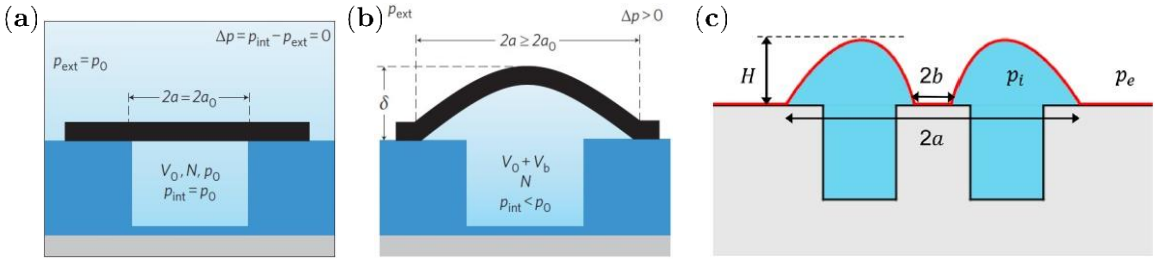

Fig. 1.3. Bulge tests. (**a**) The initial configuration [70]. (**b**) The bulged configuration [70]. (**c**) The partially bulged configuration in the island/post bulge test [73].

Koenig et al. designed a bulge test device where a silicon oxide chamber was sealed by a graphene film with the initial internal and external pressures being both equal to p_0 [70]. Then the device was moved to an environment with the pressure below p_0 so that the graphene would bulge up. Due to the impermeability of graphene to gases [71, 72], the number of gas molecules in the chamber can be considered as constant during the bulging process. By minimizing the free energy of the system and applying ideal gas law, the graphene/substrate adhesion energy can be obtained as a function of the film deflection. A variant of this

bulge test, with an additional island in the chamber center (Fig. 1.3c), was developed to study bulge state instability when the external pressure changed [73]. With the external pressure being below a critical pressure, the graphene film bulges into an annular blister. If the pressure continues to decrease, the central part of graphene film will delaminate from the island and a common spherical blister will form. Before the pressure difference across the film is large enough to cause further delamination on the outer edge of the chamber, the transition from annular to spherical blister is reversible [74]. This method can also be applied to other 2D material thin films, for both monolayer and multilayer [75, 76].

Note that the method to estimate adhesion energy through bulge test does not need the knowledge of elastic modulus of the film. After the central deflection is measured, the elastic modulus can be calculated according to the Hencky's solution [77].

1.3.3 Membrane Indentation Test

The membrane indentation test is such that an indenter (usually with a spherical or flat tip) is pressed onto a freestanding thin film/membrane clamped on the edge, as shown in Fig. 1.4a. For the convenience of operation and theoretical analysis, the thin film is usually chosen to be circular, and the indentation position is in the center of the film.

Theoretical study on this problem was done by E. Schwerin in 1929 following the works of A. Föppl and H. Hencky on the deformation of membrane under uniform pressure. For linear elastic thin films under small load or large pretension, a linear stage dominates where the indentation force is linear in the deflection of the thin film (i.e., $F \sim \delta$); otherwise, the applied indentation force is found to be cubic in the deflection, i.e., $F \sim \delta^3$ [78-82]. To fully solve the stress and deformation distributions in the indented film, the Föppl-Hencky-von Kármán equations for membrane and plate with large-deflection should be used.

The spherical tip indenter problem was solved for incompressible, hyperelastic membrane materials allowing large rotation and large strains [83]. This problem is governed by three first-order ordinary differential equations and only numerical solutions can be obtained. For substantially thick or soft films, however, local deformation of the thin film near the indenter tip should also be taken into account. Basically, this part can be approximated by superimposing the Hertz contact solution to the Schwerin deflection solution to obtain the total indenter displacement [84].

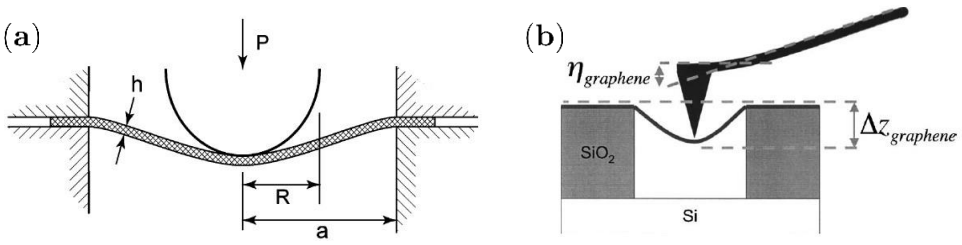

Fig. 1.4. Membrane indentation test. (**a**) A membrane indented by a spherical tip indenter [84]. (**b**) Suspended graphene sheet indented by AFM tip [85].

The membrane indentation test can be used to measure in-plane homogeneous mechanical properties of 2D material thin films indented by microscopic tip (Fig. 1.4b). Since the indentation force and central deflection can be measured in experiment, material properties like Young's modulus can be obtained by fitting experiment data with the established models. C. Lee et al. used the fitting equation combining the linear with the cubic stages in the deflection process to determine the 2D elastic modulus and pretension of graphene monolayer [5]. The Young's modulus was found to be as high as $E = 1.0 \pm 0.1$ TPa. The ultimate strength and third-order elastic modulus can be accordingly obtained as $\sigma_{\mathrm{m}} = 130 \pm 10\mathrm{GPa}$ and $D = -2.0 \pm 0.4\mathrm{TPa}$, respectively. Few-layer graphene with thickness between

2 and 8nm was tested using the same method, and an averaged elastic modulus of 0.5TPa was obtained for eight different samples [85]. As monolayer and few-layer 2D materials are ultrathin and their bending stiffness is negligible, the deformation due to the interaction between the indenter tip and suspended 2D nanosheets can be substantial and will affect the estimation on second- and third-order moduli by membrane indentation test [86]. However, for paper-like multilayer 2D material thin films, the effect of interfacial interaction can be neglected compared with that of film bending stiffness.

1.3.4 Lap Shear Test

Lap shear test is a common experimental method to measure the adhesive properties between two bonded strips (i.e., the adherends) under shear loading. Sometimes the thickness of the adhesive layer is so small that it can be neglected, so the two strips are considered to interact through adhesive interfaces. There are mainly two types of lap shear test configurations: double lap joint and single lap joint (Fig. 1.5a, b). Theoretically, the double lap joint can be regarded as two single lap joints bonded in mirror if the two adherends have the same geometry and are made of the same material. In this case, the single lap joint setup is more convenient for theoretical analysis and thus more widely adopted.

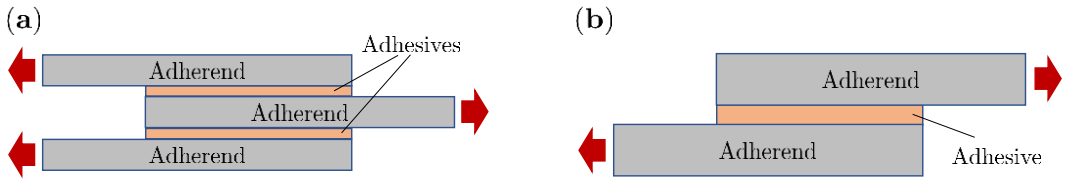

Fig. 1.5. Lap shear test. (**a**) Double lap shear configuration. (**b**) Single lap shear configuration.

The lap shear problem was first systematically investigated by M. Goland and E. Reissner [87] considering the pure elastic adherends. Forces applied on the joint and stress

distributions in the joint were solved for two extreme cases: thin adhesive layer and thick adhesive layer. Hahn then extended the classic problem to the one with dissimilar adherends [88]. By considering the plasticity of the adhesive, Hart-Smith obtained explicit closed-form solution to the adhesive shear stress distribution [89]. Three failure modes can be identified: adherend bending failure due to eccentricity in load path, peel failure due to transverse tension and shear failure of the adhesive. M. Tsai and J. Morton corrected some errors in the Goland-Reissner theory and took the Poisson effect into account [90].

Like the bulge test discussed in subsection 1.3.2, the lap shear test is another effective method to measure the interfacial adhesion between 2D nanosheets and the substrate. However, applying lap shear test to monolayer 2D materials is very challenging, because it is difficult to attach both sides of the 2D nanosheet to the adherends firmly without large area of gaps. Nevertheless, it is feasible to conduct lap shear test for 2D material composite thin films (e.g., polymer-graphene composite). For example, the graphene-embedded composite adhesives have been widely tested and studied using the lap shear method [91-93]. On the other hand, lap shear tests using multilayer GO and $MoSe_2$ thin films as adhesives have also been implemented to measure the fracture energy of multilayer 2D material thin films [94]. The fracture energy was found to exceed that needed to delaminate ordered stacks of continuous 2D nanosheets, presumably due to energy dissipation and chaotic crack motion during nanosheet film disassembly at the crack tip.

1.3.5 Peeling Test

Peeling test is another method that can be used to measure interfacial properties like interfacial strength and toughness. The standard configuration of peeling test contains a thin film adhered to a flat substrate and peeled by a force on the end (Fig. 1.6a). The peel force

is usually within the plane perpendicular to the crack front and may orients with different peeling angles which are the angle between the peel force and substrate surface. For pure elastic thin films, K. Kendall developed a classical model describing the steady state peeling process from the energy point of view [95]. Dissipation energy due to plastic bending of the thin film was then considered to extend Kendall's model to the case of elastic-plastic thin film [96, 97]. One result of the plastic term is that the minimum peel force for an elastic-plastic thin film will occur with a peeling angle less than 180°, while in Kendall's model the peel force is minimum with the peeling angle of 180°. The reason for this difference lies in that, large peeling angle basically results in large moment on the crack front and small critical peel force, while in the case of elastic-plastic thin film, it also induces more plastic dissipation and less change in adhesive energy. The two competing factors contribute to a minimum peel force at the peeling angle less than 180°. Except the classic configuration, the peeling test has some other variants, like the T peeling test and double cantilever beam peeling test, which will not be discussed in detail here.

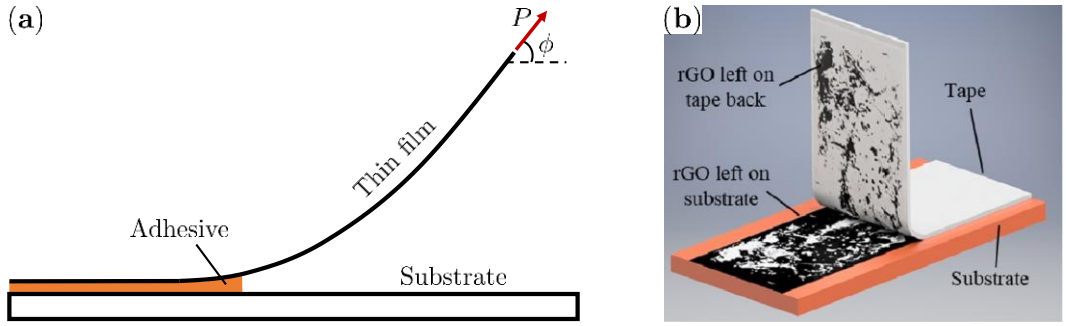

Fig. 1.6. Peeling test. (**a**) Schematic diagram of the peeling of an elastic thin film on substrate. (**b**) Peeling of a tape from the substrate with rGO paper as the adhesive [100].

It is difficult to prepare apparatus of the standard peeling test for monolayer 2D materials, as the peel force that can be applied on the edge of 2D nanosheets is too small to peel the film off the substrate. To avoid this problem, the configuration with a multiwalled carbon nanotube attached on graphene was adopted [98]. The end of the carbon nanotube was attached to an atomic force microscope (AFM) cantilever and peeled off from graphene. In another configuration, with the assistance of a scanning electron microscope (SEM) nanoprobe and a metal disk, MoS_2 multilayers were peeled to form a circular truncated cone [99]. This method, however, might not be applicable to the 2D monolayers attached to the substrate more tightly than to the metal disk. For paper-like multilayer 2D material thin films, the standard peeling test becomes feasible. For example, thermally reduced graphene oxide layers were peeled off from polymer substrate in the mixed mode of rGO-rGO cohesive failure and rGO-substrate adhesive failure (Fig. 1.6b) [100]. The percentage of the two failure modes can be measured with image processing technique, and the corresponding failure energies can be determined based on established mathematical models.

1.4 Numerical Investigation Tools

There are a variety of numerical approaches that have been used to study mechanical, electronic, magnetic and thermal properties and behavior of 2D material thin films. These tools are suitable for different systems in different scales.

In the atomic scale, density functional theory (DFT) simulations can be utilized to obtain electronic structures, properties of crystal lattice, and mechanical deformation of monolayer or few-layer 2D materials under static loading. DFT simulations are based on first principles and quantum mechanical modeling, and powerful in predicting the intrinsic

properties of nanoscale 2D materials when experimental data are difficult to obtain [101]. However, the computational cost increases amazingly with the number of simulated atoms due to the curse of dimensionality. Therefore, for larger systems with more atoms or large molecules, molecular mechanics (MM) and molecular dynamics (MD) methods find their applications in simulating deformed configuration and movement as well as predicting dynamic properties of the systems [102, 103].

When the scale further increases, MM and MD simulations will encounter the same problem of rapidly increasing computational cost as DFT method does. On the other hand, the behavior of individual atom or molecule becomes insignificant to the whole system, and instead the averaged meso- or macro-scale response is of primary concern. In this situation, phase field method can be a good choice, especially for problems with complex material morphologies and interfaces, such as grain growth and coarsening, as well as crack propagation [104-106]. In this method, grain boundaries and crack surfaces in 2D materials, which are difficult to deal with in continuum models, can be represented by a phase field that smoothens the discontinuities over a small region [107-109]. Evolution of the discontinuities is governed by a system of partial differential equations. The phase field method is sometimes combined with finite element methods (FEM). The latter turn out to be effective and powerful tools to study the macroscale behavior of 2D material thin films.

1.5 Outline of the Present Work

In the light of the excellent performance of 2D materials in various fields, novel applications combining with superior properties of 2D materials are worth more scientific and engineering attentions. In this dissertation, the potential applications of 2D material thin

films in functional wearable devices is focused and a specific function of concern is mosquito bite prevention. Theoretical modeling and numerical simulation were taken, together with existing experiment results, to reveal the capability of the graphene-based thin films in preventing mosquito bite as well as the underlying mechanisms. These tools and testing methods provide effective protocols for searching 2D material candidates for mosquito/insect bite prevention.

One prospective feature of functional wearable devices is the integration of flexible photovoltaics and electronics to achieve visual interaction interface, telecommunication and real-time health sensing, among others. In this aspect, the application of graphene has been limited due to the lack of electronic bandgap, but graphene nanoribbon was found to exhibit tunable bandgap the size of which inversely scales with the ribbon width [110]. Although many efforts have been done to synthesize nanoribbons of graphene and its derivative heterolayers using different strategies [111-113], it is still difficult to achieve the production in large scale for practical applications. This problem will be discussed in this dissertation by developing effective theories and models for the novel mechanical nanofabrication technologies that were developed recently and potential to produce 2D nanoribbons in large scale.

The rest of this dissertation will be organized as follows.

In Chapter 2, graphene-based thin film barriers were proposed to prevent mosquito bites. Mechanical properties and breathability of two graphene-based thin films (GO and rGO) in both dry and wet states were investigated through theoretical modeling and simulations, together with experiment results. The capability of the two films in preventing mosquito biting includes the effects of molecular and mechanical barriers. How to balance

the strength and breathability of the barriers in both dry and wet environments is the key problem to design feasible wearable devices with mosquito bite prevention.

In Chapter 3, the shear stability of two kinds of 2D material thin films, i.e., multilayer GO and $MoSe_2$ films, was studied through the lap shear test. The 2D material thin films of different thickness were sandwiched between two polymer adherends which were applied with lap shear loading. Based on a cracked lap shear model and finite element calculation, a shear-to-tensile failure mode transition was proposed to explain the experiment phenomenon that the critical shear forces for GO and $MoSe_2$ films exhibit distinct dependence on film thickness in the studied range. The modeling and simulation also imply that the extraordinary fracture energies of the multilayer films are associated with the mixed cohesive and interfacial failure mode. This study is useful for us to understand the mechanical behavior of 2D material thin films under shear when embedded in wearable devices.

In Chapter 4, a necking-affected shear lag model was developed to explain the controlled fragmentation of monolayer 2D materials embedded in a fiber cladding or attached on a substrate, both made of ductile polymer. By applying uniaxial tension, the neck localized in the cladding/substrate will propagate and cause ordered fragmentation of 2D nanosheets near the necking zone. It turns out that the stress distribution in nanosheets predicted by conventional shear lap model will be affected by the neck, and a peak tension will occur near the neck front, leading to sequential fragmentation in nanosheets. The fragmentation size can be tuned by changing the interfacial shear strength and geometrical dimensions. This study provides a potential solution to the large-scale production of 2D material nanoribbons which may promote development of flexible electronics in wearable devices.

In Chapter 5, the works introduced in this dissertation will be summarized and the key messages from the results obtained in these studies will be reviewed. Based on the completed works, some extended potential directions that are undergoing and to be done will be briefly introduced.

Chapter 2 Strong and Breathable Graphene Barriers for Mosquito Bite Prevention

2.1 Introduction

The experiment parts in this chapter were designed and performed by our collaborator Prof. Robert H. Hurt group (including Cintia Castilho and Muchun Liu) at Brown University.

Mosquitos are one of the world's most important and dangerous vectors for the transmission of infectious diseases such as malaria, zika, yellow fever and dengue fever [114-116]. Mosquito-borne illnesses affect nearly 700 million people with over 1 million global deaths each year. According to the World Health Organization (WHO), more than 400,000 deaths were caused by malaria in 2015 alone. The dengue cases and associated deaths in many regions like Southeast Asia and South America have witnessed new highs in the past few years.

Mosquito is naturally endowed with capabilities of sensing, biting and sucking blood through human skin: 1) it can detect carbon dioxide plume from human breathing as far as 10 to 50 meters away; 2) at closer distance, it takes volatile chemical substances from human sweat as clues for tracking; 3) within about 20 centimeters the thermal and moisture plume can be detected by mosquito [117, 118]. Mosquito's long and sharp fascicle can bite through thin fabric and even soft polymer membranes. People are often bitten by mosquitos carrying viruses without any awareness until symptoms appear. At present, mosquito bite prevention relies almost exclusively on various categories of chemical repellents (e.g., diethyltoluamide (a.k.a. DEET), Icaridin and Ethyl butylacetylaminopropionate), most of which are to different degrees toxic to human, especially pregnant females and babies, as

well as to the ecosystem. Another problem is that mosquitos can develop resistance to chemical repellents and reduce the efficacy of chemical repellents [119].

In contrast, a physical-based approach to mosquito bite prevention has the advantages of being less toxic, more environmentally friendly, sustainable and cost effective without the need to address the drug resistance problem. However, many fabrics are not physically protective to mosquito bite due to the sparse yarns and insufficient mechanical property to resist mosquito biting. Considering the physical features of functional wearable devices and outstanding mechanical properties of 2D materials, it is of great interest to explore if graphene-based thin films can serve as barriers to prevent mosquito fascicle penetration.

Two graphene-based thin films, i.e., GO and rGO film, were prepared as candidates for mosquito bite prevention. The freestanding GO thin films were obtained through drop-casting [54] of homogenous colloidal suspensions of GO nanosheets prepared by a modified Hummers' method [120]. The dispersed GO nanosheets have lateral sizes $\sim 1\mu m$ and a C/O atomic ratio of ~ 2.1. The polymer substrates were cut into squares, washed with ethanol and treated with pure oxygen plasma to facilitate wetting. The GO suspension was drop-cast onto substrates which were then dissolved in DCM, and the freestanding GO films were used after washed with DCM, acetone and ethanol in sequence. The rGO thin films were obtained by reducing the prepared GO films. The reduction was carried out by exposing the GO films to HI vapor at $85°C$ for 1 to 5 minutes. The exposure time was varied according to the thickness of the film. A beaker with $2mL$ of HI was heated to the specified temperature and the films were then placed on a layer of cheesecloth on top of the beaker and exposed to HI vapor. The films were rinsed with ethanol to remove residual HI and dried in an oven at $60°C$.

2.2 Breathability of Graphene-Based Thin Films

A significant consideration for wearable materials is the breathability which measures how fast the water vapor permeates through the material under specific conditions. A well breathable thin film allows fast evaporation of sweat secreted by human skin and does not bring uncomfortable feeling to the wearer. Since the paper-like graphene-based thin films have the brick-and-mortar structure where the nanosheets are stacked in an interlocked way, the interlayer gallery spacing makes it possible for water molecules to permeate across the films. Furthermore, it turns out that the interlayer spacing of GO films in wet environment can be expanded to some extent [17], promoting the passing of water molecules. The graphene-based thin films with high water permeation above a critical value are considered as breathable films in this study.

To measure the permeation rate of water molecules (and toxicant molecules in the air) across graphene-based thin films, a breathability measurement device (Fig. 2.1a) was designed where water vapor concentration gradients on the two sides of the thin film could be controlled [121]. This device consists of an inner vessel containing water as the receptacle for collecting soluble molecules. The inner vessel is capped with an opened glass cover and a copper plate with a 1cm hole for the GO films placed in between the vessel and the cover. O-rings are used to further seal the system. An outer vessel creates the simulated atmosphere and is placed in a thermostatic bath to control temperature during the experiment. The outer vessel is mechanically stirred using a fan while the inner vessel is mechanically stirred using a magnetic stir bar (stir plate is shown in black under the vessels in Fig. 2.1a), ensuring that the transport resistances are minimized and only the film resistance is measured. The simulated atmosphere in the outer vessel is created by passing

dry air through a column of water. The water permeation is measured gravimetrically. The thin film is supported by a copper plate and fixed on the plate using an adhesive. A layer of aluminum foil is then used to further seal the system. No mass loss was detected after 6 hours at $T = 20°C$, confirming the lack of cracks and holes in the graphene films as well as the quality of the seals in the device.

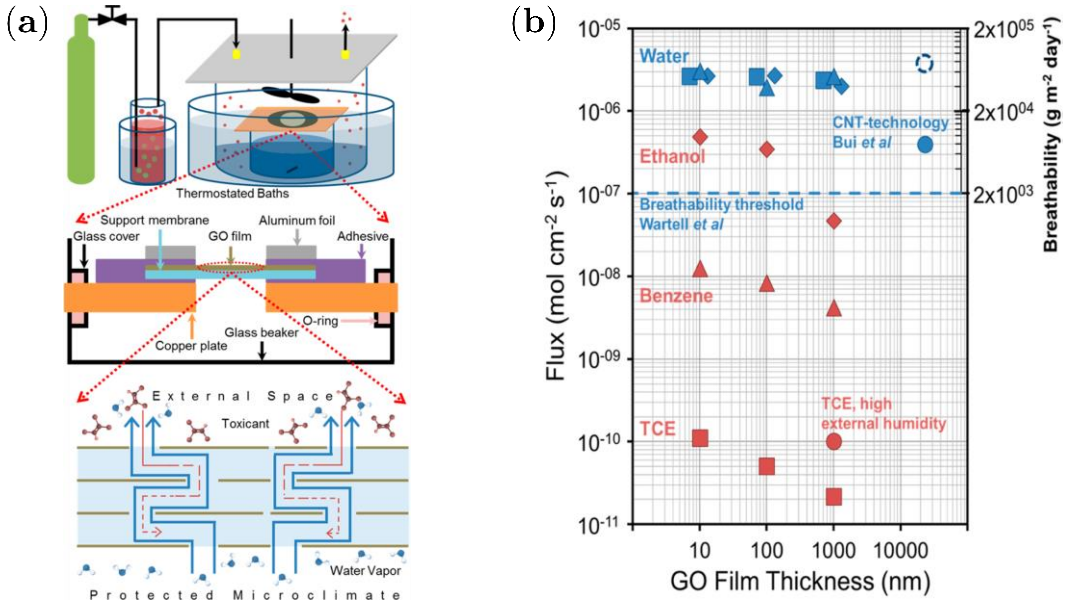

Fig. 2.1. Breathability measurement of GO thin films [121]. (**a**) The home-made devices for breathability measurement (the top and middle) and the diagram showing the molecule permeation paths (the bottom). The inner vessel in the top contains a liquid water inventory and serves the source of simulated perspiration. (**b**) Breathability of GO films with different thicknesses. Toxicant molecules can be obstructed in most cases while water molecules can pass through GO films freely with a much larger breathability than the standard (the dashed line).

By using the permeation measurement device, one can measure the breathability for different 2D material thin films. Note that the water permeation rate value of $2000\ \mathrm{g\ m^{-2} \cdot day^{-1}}$ is the commonly cited minimum standard to define a breathable fabric [122]. The experiment results show that in wet state GO films with thickness ranging from $10\mathrm{nm}$ to

10μm have a thickness-independent breathability, more than one order higher than the standard value (Fig. 2.1b) [121].

2.3 Experimental Tests for Biting Resistance

To test whether GO and rGO thin films are effective barriers to mosquito biting and also to reveal the underlying mechanisms, we conducted mosquito biting test and microneedle penetration test. The former test provides phenomenological results, which will be analyzed by combining the thin film mechanical response obtained from the latter test with the mathematical modeling results which will be introduced in detail in section 2.4.

2.3.1 Mosquito Biting Test

In the mosquito biting test, captive pathogen-free *Aedes aegypti* mosquitos were raised in a homemade mosquito enclosure with the environment of controlled temperature and humidity. During the test, rectangular skin patches of typical area $4\sim6\text{cm}^2$ were exposed for 5-min intervals to batches of ~100 mosquitos in the enclosure while being monitored by video microscopy and macrophotography. Mosquito behavior (landings, residence times, head positions indicating penetration, and abdominal swelling/red coloration indicating blood feeding) were observed for bare and graphene-coated skin patches (Fig. 2.2a-c). Bite numbers were determined by postexposure skin examination confirmed by video review of head positions and abdominal swelling.

Fig. 2.2d shows example raw data on bite counts (bites per 5-min experiment) presented in the order in which the randomized trials were performed. Bare skin and cheesecloth-covered skin experiments were conducted as controls, with the cheesecloth (a thin, loose-weave fabric) being used to hold graphene films directly against the skin. Compared with

the control groups, no bites were recorded during any experiment with dry GO films. Basically, the results for dry rGO films are the same as those for dry GO films. These results imply that in dry state (equilibrated with laboratory room air measured at 51% relative humidity) GO and rGO thin films can effectively prevent mosquito bites.

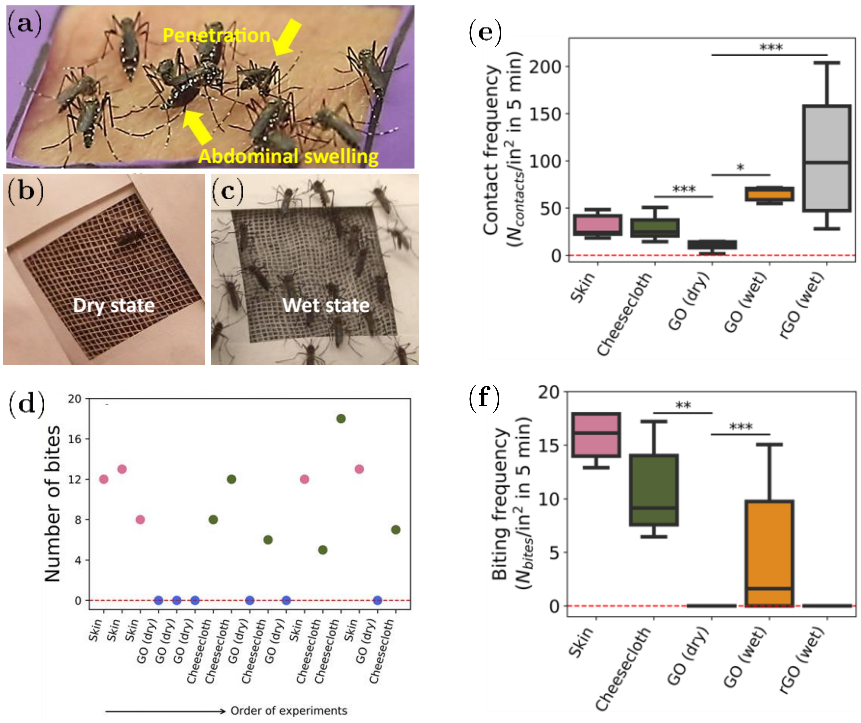

Fig. 2.2. Mosquito biting tests for bare skin, cheesecloth, GO and rGO thin films. (**a**) Typical mosquito behavior observed during bare skin control experiments. (**b, c**) Mosquito landing behavior on GO thin films in dry and wet states, respectively. (**d**) Example raw data on bite counts presented in the order in which the randomized trials were performed. (**e**) Experimental statistics on mosquito contact frequency on dry and wet graphene films compared to control experiments. (**f**) Plot of mosquito biting frequency on dry and wet graphene films compared to control experiments.

However, when the GO and rGO thin films were in wet state (smeared with human sweat or water), this barrier effect failed to protect the skin from detection of mosquito. On the contrary, mosquitos contacted the films with frequencies even higher than those in the controls, as shown in Fig. 2.2e. This is because human sweat and water can be attractive to

mosquitos. Mosquitos have olfactory and gustatory receptors that can sense the chemical attractants from human sweat, which were trapped beneath the impermeable graphene-based thin films in dry state. Nevertheless, from the biting frequency data shown in Fig. 2.2f, the wet rGO films could still resist mosquito biting probably due to their good mechanical strength. The GO films after absorbing water, however, converted to mechanically soft hydrogels that became nonprotective.

2.3.2 Microneedle Penetration Test

To explore the mechanism of persistent resistance of wet rGO films to mosquito bite, the microneedle penetration test was implemented. In this test, a microneedle was driven to indent and penetrate the film suspended over a hole of 0.5cm in diameter and clamped between two plexiglass supports. The movement of the needle was stopped after the film was penetrated. The penetration force and tip displacement were tracked during the test. The critical penetration force (CPF), defined as the maximum indentation force during the loading, indicates the resistance of the film to the tip indentation. Since the loading was assumed to be quasi-static and the radius of needle tip was much smaller than the film size, a membrane indentation model [79-83] (Fig. 2.3a) could be adopted to relate the measured CPF to the insertion force associated with mosquito bite.

Fig. 2.3b shows an example indentation force data in terms of indenter displacement. The initial part is characterized by a load-free stage with small fluctuation, because there are always some imperceptible gaps between the indenter tip and the surface of thin film. Once the tip contacts the film surface, the indentation force increases in a power-law way. After the point of the CPF, the load drops immediately and remains at a small value due to

friction. This phenomenon shows that the graphene-based thin films fail and fracture in quite a brittle way.

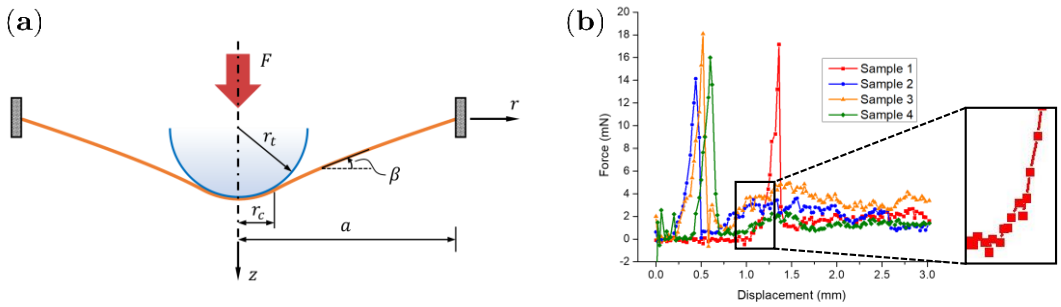

Fig. 2.3. Microneedle penetration test and experiment results. (**a**) Schematic diagram of the microneedle penetration model. (**b**) The histories of indentation force with respect to tip displacement for four samples.

2.4 Modeling and Simulation

To help understand the mechanical response of GO/rGO films in needle penetration tests and to validate the mechanical barrier hypothesis, we adopted a continuum membrane model where a circular, elastic membrane with clamped edges was indented by a rigid spherical indenter at the center (Fig. 2.3a). Both mathematical formulation and finite element simulations were implemented for the membrane indentation model.

2.4.1 Membrane Indentation Model

In the membrane indentation model, the membrane is assumed to be linearly elastic until failure occurs when the maximum tensile stress in the membrane reaches a critical value. To reduce the complexity of the problem and to be consistent with experiment setups, the following simplifications were made without losing essential features: (1) In modeling the GO/rGO films as a thin membrane, we neglected the effect of bending which is insignificant compared to membrane tension since the thickness of thin films in test was at least

two orders smaller than the other dimensions; (2) The membrane boundary was assumed to be perfectly clamped, which is expected to provide a lower bound to the CPF in case some boundary sliding occurs; (3) The indenter tip was assumed to be rigid as the deformation of the tip is usually negligible compared to that of a flexible membrane.

Even though the size of the indenter tip is much smaller than the membrane radius, its effect on the membrane stress distribution cannot be ignored. By assuming that the indenter tip has the radius r_t, the membrane can be divided into two regions: the contact region $0 \leq r \leq r_c$ where r_c is the radius of contact area, and the free region $r_c < r \leq a$ (Fig. 4b) with a being the membrane radius. The contact region is loaded by the pressure $p(r)$ from the indenter tip, and the outer edge of the free region is clamped.

Table 2.1. Dimensional and dimensionless quantities in the membrane indentation model.

Dimensional variables	Dimensionless variables
Radial coordinate r	$\rho = r/a$
Radius of indenter tip r_t	$\rho_t = r_t/a$
Radius of contract area r_c	$\rho_c = r_c/a$
Membrane thickness h	$H = h/a$
Axial deflection w	$W = w/a$
Radial displacement u	$U = u/a$
Stress components σ_r, σ_θ	$S_r = \sigma_r/E$, $S_\theta = \sigma_\theta/E$
Indentation/Penetration force F, F_p	$\bar{F} = F/(Ea^2)$, $\bar{F}_p = F_p/(Ea^2)$
Pressure in contact area P	$P = p/E$

Föppl-Hencky membrane theory [77], which can also be obtained from von Kármán equations by neglecting the bending terms, was adopted to model the indented membrane. With the introduction of dimensionless variables listed in Table 2.1, the out-of-plane/axial equilibrium equation and the compatibility equation can be expressed as [78, 79]:

$$-HS_r(\rho)\frac{\mathrm{d}W(\rho)}{\mathrm{d}\rho}=\frac{1}{\rho}\int_0^{\rho}P(\rho)\rho\mathrm{d}\rho, \tag{2.1}$$

$$\rho\frac{\partial}{\partial\rho}\left\{\frac{1}{\rho}\frac{\partial}{\partial\rho}[\rho^2S_r(\rho)]\right\}+\frac{1}{2}\left[\frac{\mathrm{d}W(\rho)}{\mathrm{d}\rho}\right]^2=0. \tag{2.2}$$

The normalized circumferential stress component S_θ can be obtained through the in-plane/radial equilibrium equation:

$$S_\theta(\rho)=\frac{\mathrm{d}}{\mathrm{d}\rho}[\rho S_r(\rho)]. \tag{2.3}$$

Then the normalized radial displacement U can be calculated as

$$U(\rho)=\rho\varepsilon_\theta(\rho)=\rho[S_\theta(\rho)-\nu S_r(\rho)] \tag{2.4}$$

where ε_θ is the circumferential strain component and ν the in-plane Poisson's ratio.

In the contact region $0\le\rho\le\rho_c$, the normalized membrane deflection W is determined by the indenter tip profile which is commonly assumed to be spherical:

$$W(\rho)=\bar{d}+\sqrt{\rho_t^2-\rho^2},\qquad 0\le\rho\le\rho_t, \tag{2.5}$$

where $\bar{d}$ is the normalized downward displacement of the indenter tip (by membrane radius a). Actually, the tip profile can be of a more complex form using the present method, the case of which will be discussed in subsection 2.5.4. Substituting Eq. (2.5) into Eq. (2.2) and integrating the resulting equation twice yield

$$S_r(\rho)=-\frac{\rho_t^2-\rho^2}{8\rho^2}\ln(\rho_t^2-\rho^2)+\frac{4c_1-1}{8}+\frac{c_2}{\rho^2} \tag{2.6}$$

where c_1 and c_2 are constants. Since the radial stress component is finite at the center of the membrane, we have the condition $S_r(0)<\infty$, which leads to

$$c_2=\frac{\rho_t^2\ln\rho_t}{4}. \tag{2.7}$$

In the free region $\rho_c<\rho\le1$, the axial equilibrium Eq. (2.1) can be expressed as

$$-HS_r(\rho)\frac{\mathrm{d}W(\rho)}{\mathrm{d}\rho}=\frac{\bar{F}}{2\pi\rho} \tag{2.8}$$

where the normalized indentation force $\bar{F}=\int_0^{\rho_c}P(\rho)\cdot 2\pi\rho\mathrm{d}\rho$. Combining Eq. (2.8) and Eq. (2.2) yields

$$S_r^2(\rho)\rho^3\frac{\partial}{\partial\rho}\left\{\frac{1}{\rho}\frac{\partial}{\partial\rho}[\rho^2 S_r(\rho)]\right\}=-\frac{1}{8}\left(\frac{\bar{F}}{\pi H}\right)^2. \tag{2.9}$$

The solution to Eqs. (2.8) and (2.9) can be written in the form of polynomial series as

$$W(\rho)=Q^{\frac{1}{3}}\sum_{n=0}^{\infty}a_n\left(1-\rho^{\frac{4n+2}{3}}\right), \tag{2.10a}$$

$$S_r(\rho)=\frac{3}{2}Q^{\frac{2}{3}}\sum_{n=0}^{\infty}b_n\rho^{\frac{4n-2}{3}} \tag{2.10b}$$

where $Q=\bar{F}/(2\pi H)$ is a dimensionless loading variable. $\{a_n\}$ and $\{b_n\}$ are coefficients whose values can be determined through Eqs. (2.8) and (2.9) together with the boundary condition on the outer edge of the membrane. For the clamped boundary condition,

$$U(1)=\left[(1-\nu)\rho S_r(\rho)+\rho^2\frac{\partial S_r(\rho)}{\partial\rho}\right]_{\rho=1}=0. \tag{2.11}$$

The corresponding values of the first few entries in the coefficient arrays $\{a_n\}$ and $\{b_n\}$ are listed in the Table 2.2 for two values of Poisson's ratio.

Table 2.2. Values of coefficient series $\{a_n\}$ and $\{b_n\}$ for different Poisson's ratios.

$\nu=0.17$				$\nu=0.30$			
a_0	1.817	b_0	5.50×10^{-1}	a_0	1.817	b_0	5.50×10^{-1}
a_1	6.05×10^{-2}	b_1	-5.50×10^{-2}	a_1	1.45×10^{-2}	b_1	-1.31×10^{-2}
a_2	5.18×10^{-3}	b_2	-2.35×10^{-3}	a_2	2.96×10^{-4}	b_2	-1.35×10^{-4}
a_3	5.75×10^{-4}	b_3	-2.00×10^{-4}	a_3	7.87×10^{-6}	b_3	-2.74×10^{-6}
a_4	7.21×10^{-5}	b_4	-2.14×10^{-5}	a_4	2.36×10^{-7}	b_4	-7.00×10^{-8}

At the boundary between the contact and free regions, three continuity conditions should be satisfied:

$$\left[\frac{\mathrm{d}W}{\mathrm{d}\rho}\right]^{-}_{\rho=\rho_c} = \left[\frac{\mathrm{d}W}{\mathrm{d}\rho}\right]^{+}_{\rho=\rho_c}, \tag{2.12a}$$

$$[W]^{-}_{\rho=\rho_c} = [W]^{+}_{\rho=\rho_c}, \tag{2.12b}$$

$$[S_r]^{-}_{\rho=\rho_c} = [S_r]^{+}_{\rho=\rho_c} \tag{2.12c}$$

where $(-)$ and $(+)$ represent quantities on the point within the contact and free regions, respectively. The Eq. (2.12a-c) is used to determine the values of the normalized contact radius ρ_c, constants $\bar{d}$ in Eq. (2.5) and c_1 in Eq. (2.6). Once these variables are obtained, the displacement and stress fields in the contact and free regions can be calculated from Eqs. (2.3) - (2.7) and (2.10).

In the present membrane indentation problem, it turns out that the radial stress component monotonically decreases from the center to the edge of the membrane. Eq. (2.3) indicates that S_θ is smaller than S_r everywhere except at the center where we have $S_r = S_\theta$. Therefore, the maximum tensile stress in the membrane corresponds to the radial stress at the center $S_r(0)$. According to the maximum tensile stress criterion, we have

$$S_r(0) \leq S_t \tag{2.13}$$

where $S_t = \sigma_t/E$ is the normalized tensile strength of the membrane. The corresponding indentation force is taken as the CPF of the membrane.

It can be verified that the above solution to our membrane indentation problem converges to the classical Schwerin's solution [80] to the problem under a point load. Fig. 2.4a compares Schwerin's solution, finite element (FE) results and our analytical solution.

Relevant FE setups will be introduced in the subsection 2.4.2. Note that FE simulations will encounter convergence problems as the tip radius becomes very small. In Fig. 2.4b, the penetration forces predicted by the analytical solution are in good agreement with the FE results. There is some difference in radial stress in the large deformation regime due to the intrinsic approximations of Föppl-Hencky membrane theory.

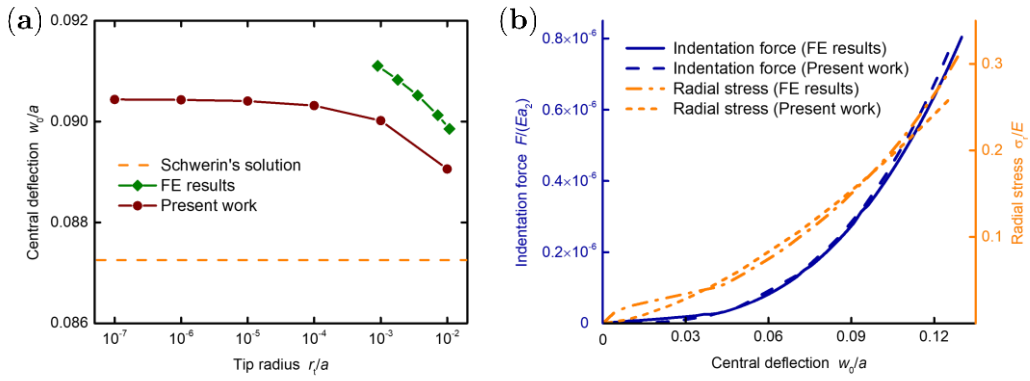

Fig. 2.4. Responses of an indented freestanding membrane. (**a**) The central deflection of the membrane for different tip radii. The solution converges as the tip radius goes to zero. (**b**) The histories of indentation force and radial stress at the center obtained from the analytical model and FE simulations.

Note that, in the analytical solution, Eq. (2.12a-c) does not ensure smoothness in the radial stress and continuity in the radial displacement at the edge of the contact area. The reason lies in that the polynomial series in Eq. (2.10) are approximate solutions to the governing equations. Nevertheless, the present analytical solution should be applicable for the problem in hand since the radial displacement is expected to be very small in our cases.

2.4.2 Finite Element Simulation

FE analysis was performed to verify the mathematical modeling and take more sophisticated configurations into account. An axisymmetric FE model (Fig. 2.5a) was implemented in the commercial FE analysis software Abaqus (Dassault Systèmes Simulia Corp.,

Providence, RI) to investigate the effect of a hyperelastic substrate, which mimics human skin, on the CPF F_p. The bottom of the substrate was fixed, while the lateral boundaries of the substrate and edges of the membrane were free. A spherical indenter tip moved downward at the center of the membrane. Hard contact in the normal direction and frictionless interaction in the tangential direction were applied to the interfaces between the tip and the membrane as well as between the membrane and the substrate.

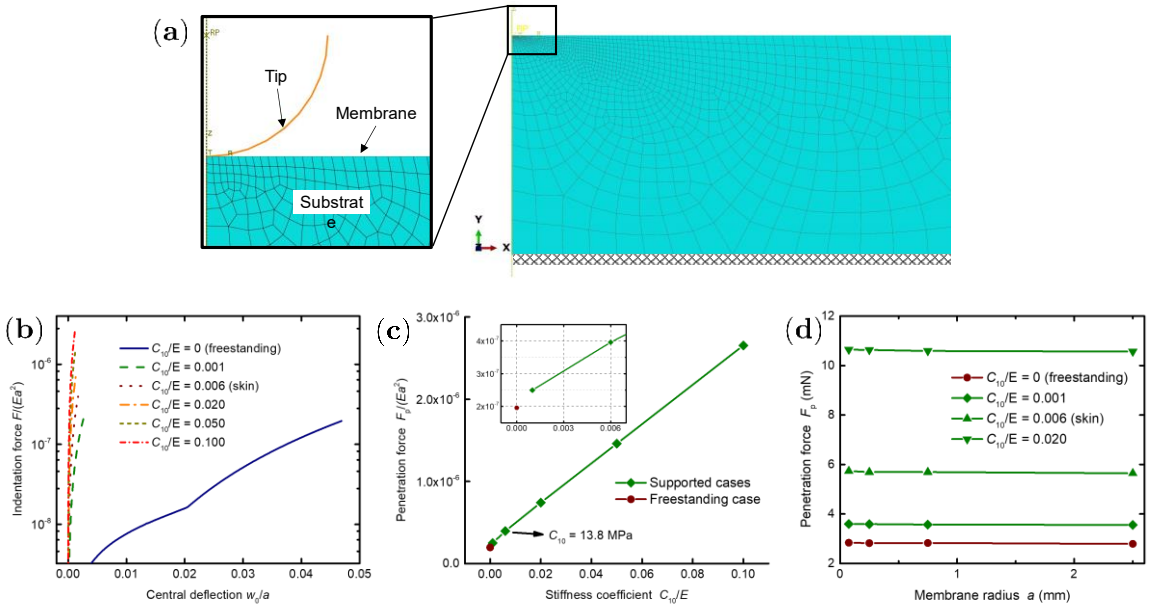

Fig. 2.5. Effects of hyperelastic substrate on the indentation force of thin film. (**a**) The FE model of the tip-membrane-substrate system (**b**) Indentation force for different substrate stiffness coefficients. The values of $C_{10} = 0$ and $C_{10}/E = 0.006$, where E is the membrane Young's modulus, correspond to the cases without and with substrate, respectively. (**c**) Critical penetration forces for different substrate stiffness coefficients. The inset shows the details when C_{10} is small. The membrane thickness is assumed to be $h/a = 0.002$, where a is the membrane radius, in all cases in (**b**) and (**c**). (**d**) Changes of critical penetration force with truncations on the membrane size.

The Young's modulus E of the membrane was estimated by nonlinear fitting with microneedle penetration experiment data. A cubic power law between the CPF and central deflection can be identified in the theoretical model [79-80], and then utilized for the fitting

process. The average fitted Young's moduli of GO/rGO films (2.28GPa/2.55GPa) are lower than previously reported values [18, 123-125] probably due to differences in GO/ rGO nanosheet sizes, drying conditions and reduction conditions (for rGO films). The Poisson's ratio for GO/rGO films was taken as $\nu = 0.17$, and small deviation from this value has been shown to have limited influence on the results (see subsection 2.5.3).

The membrane element with zero bending stiffness was used to mesh the thin membrane, and the indenter tip was treated as a rigid object. Other model parameters were taken from the needle penetration experiment for dry GO/rGO films (Table 2.3). The substrate was assumed to obey the following Neo-Hookean constitutive law for an incompressible hyperelastic material:

$$U = C_{10}(\bar{I}_1 - 3) \tag{2.14}$$

where U is the strain energy per unit volume in the reference configuration, C_{10} is a coefficient associated with the stiffness of the substrate, and $\bar{I}_1 = \bar{\lambda}_1^2 + \bar{\lambda}_2^2 + \bar{\lambda}_3^2$ is the first invariant of the deviatoric strain tensor where $\bar{\lambda}_i, i = 1,2,3$ are deviatoric principal stretches in the substrate. The stiffness coefficient of stratum corneum of human skin $C_{10} = 13.8$ MPa [126] was used in this study. The freestanding membrane model serves as a reference to be compared with the model with substrate.

Table 2.3. Parameters in the needle penetration tests and membrane indentation model.

	Young's modulus (GPa)	Poisson's ratio	Membrane thickness (μm)	Membrane radius (mm)	Tip radius (μm)
GO film	2.28*	0.17†	0.5–5.0	2.5	9.0
rGO film	2.55*	0.17†	0.5–5.0	2.5	9.0

* Obtained by fitting experimental data

† Values reported in literature [127]

Fig. 2.5b shows the comparison between the freestanding membrane case and supported membrane cases with the membrane tensile strength taken to be $\sigma_t/E = 0.05$. The central membrane deflection of the substrate in all supported membrane cases is only $1/16$ or less of that in the freestanding membrane case. The corresponding CPFs are plotted in Fig. 2.5c. The freestanding membrane case has the lowest penetration force, implying that the membrane without support of substrate is the most vulnerable to penetration of a sharp tip. The CPF in supported cases decreases approximately linearly with the stiffness coefficient C_{10} of the substrate, and the point representing the freestanding case also lies close to this line. In particular, the penetration resistance of the thin membrane with human skin is almost twice that in the freestanding case. Fig. 2.5d confirms that the predicted penetration force is not sensitive to the selected membrane size in the model as along as the membrane radius is sufficiently large compared with the tip radius.

2.5 Results and Discussion

2.5.1 Fitting Young's modulus of GO/rGO films

Young's modulus of GO/rGO film is a significant material parameter and may vary in a broad range due to different preparation conditions [18, 123-125]. The value of Young's modulus of GO/rGO film can be estimated by fitting the microneedle penetration experiment data and taking advantage of the membrane penetration theoretical model.

In the indentation force plot of a GO film sample shown in Fig. 2.6a, the loading process starts from the contact between the indenter tip and the membrane, indicated by the abrupt increase in indentation force, and ends with the failure of the membrane. However,

it is difficult to identify when the indenter tip touches the membrane surface directly from the plot. Here, we utilize the scaling law between indentation force F and membrane central deflection w_0 to determine the moment of contact. For a thin membrane, the indentation force scales with the central deflection following the law [79, 80]

$$\frac{F}{Ea^2} = g(E, \nu, a, h, r_t)\left(\frac{w_0}{a}\right)^{\xi} \tag{2.15}$$

where $\xi = 3$ and the function g depends on material and geometrical parameters of the membrane as well as the tip radius. Our membrane indentation model and FE simulations (Fig. 2.4b) also support this scaling law, with the fitted exponents $\xi = 3.01$ and $\xi = 2.94$, respectively. Therefore, for each force curve, we can adjust the starting point such that the curve fits best with that predicted by the cubic scaling law, as shown in Fig. 2.6b-d.

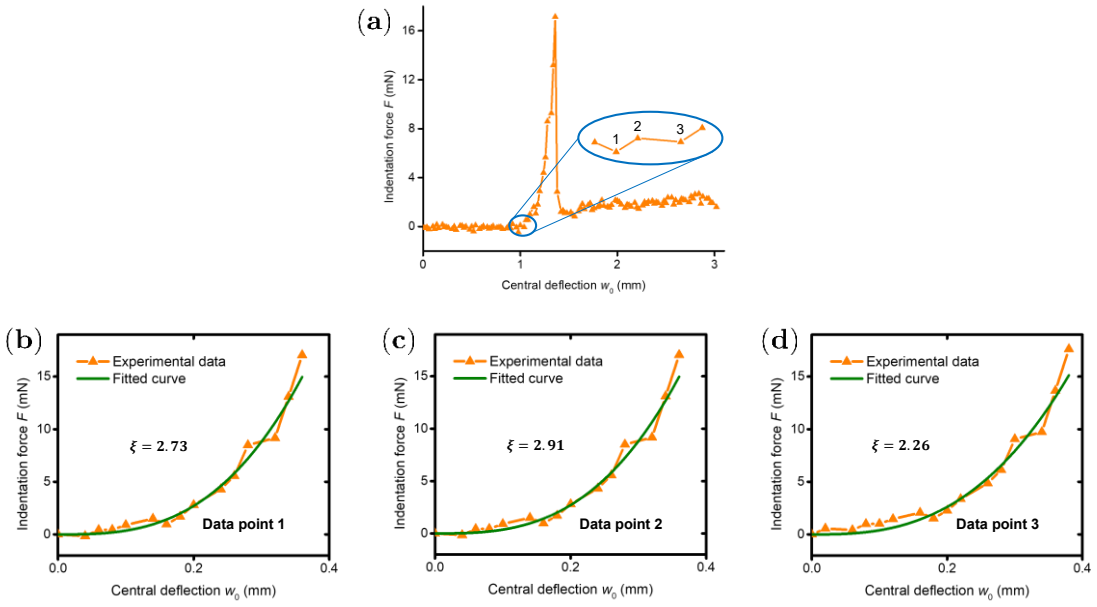

Fig. 2.6. Scaling laws in the indentation force from microneedle penetration experiment. (**a**) Indentation force for GO paper with thickness $h = 1\mu m$. Data points 1, 2, 3 are three potential starting points of the loading process. (**b-d**) Loading processes with points 1, 2, 3 taken as starting points, respectively. The exponents ξ are obtained by fitting experimental data with Eq. (2.15). Point 2 with $\xi = 2.91$ is the closest point to the true starting point of the loading process.

After the starting and ending points of the loading process have been determined, the experimental data of indentation force versus central deflection can be used to estimate the Young's modulus of GO/rGO film through the following least square fitting:

$$\begin{aligned} &\text{Find} \quad E_{\text{fit}} \\ &\text{Min.} \quad S = \sum_{i=1}^{k} [w_{0i}^{*} - w_0(F_i^{*}; E_{\text{fit}})]^2 \\ &\text{s.t.} \quad w_0 = M(F), \ i = 1, \ \ldots k \end{aligned} \tag{2.16}$$

where E_{fit} denotes the fitted Young's modulus and S the sum of squared residue between the measured and calculated values of central deflection. (F_i^{*}, w_{0i}^{*}) represents the i-th pair of indentation force versus central deflection data extracted from experiment, and k is the number of data points in the loading process. The membrane central deflection w_0 in response to the indentation force F is predicted by the membrane indentation model denoted as $M(\cdot)$. The final value of Young's modulus is taken as the average of the fitted values for samples with different thicknesses. The fitting results of Young's modulus for GO/rGO film are listed in Table 2.3.

2.5.2 Results on Penetration Force

With the micromechanical model introduced above, we can extrapolate the CPFs from the measured values for microscale needles to the values expected for the submicron mosquito fascicle. From our analytical and FE results, the CPF behaves linearly with tip radius under the same membrane strength (Fig. 2.7a). Further, the lines in Fig. 2.7a should pass through the origin if considering the limit of tip radius approaching zero. The slopes of these lines can be determined from needle penetration experiment data for at least one tip radius. Then

the insertion force of mosquito to penetrate the same membrane can be extrapolated using the tip radius of mosquito fascicle. Based on the results from our needle penetration experiment, the insertion force of mosquito to penetrate a 1.0μm thick GO/rGO film is estimated to fall in the range of 100~500μN assuming the tip radius of mosquito fascicle to be 0.1~0.5μm [128]. Considering the idealization of the clamped boundaries in our model, the real forces needed in practice could be even larger. Since the insertion forces of mosquito to penetrate human skin are only 10~20μN [126], the above calculation suggests that the 1μm thick GO/rGO films can prevent fascicle insertion of mosquito and accordingly supports the mechanical barrier hypothesis.

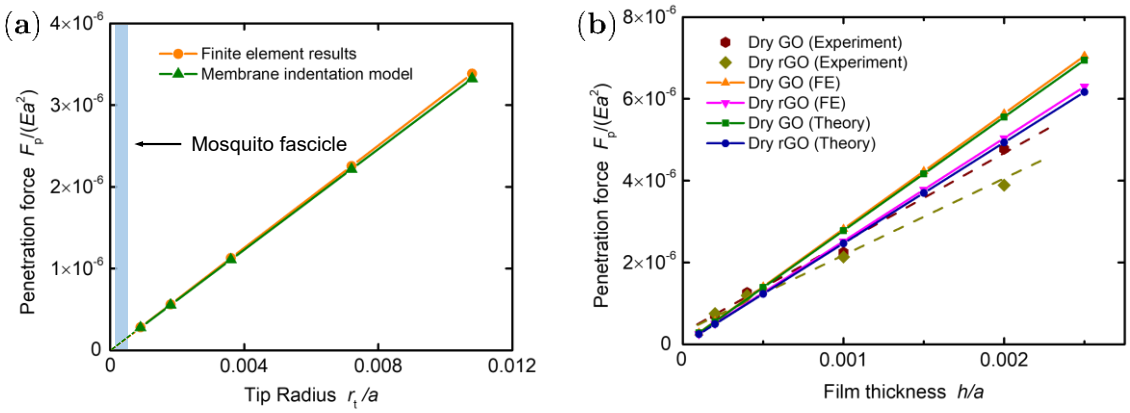

Fig. 2.7. Results from the theoretical membrane penetration model and finite element simulations. (**a**) Linear relationships between the critical penetration force and indenter tip size. The membrane thickness is taken as $h/a = 4 \times 10^{-4}$. (**b**) Variations of penetration force with different film thicknesses for GO-rGO films in the dry state. Dashed lines for experimental data are used for reference to show the linear relationships.

Membrane thickness is an important parameter for designing smart fabrics against mosquito bites. Under the assumption of a thin membrane with negligible bending stiffness, the CPF predicted from our membrane indentation model is linearly proportional to the film thickness, in agreement with the needle penetration experiments and FE simulations

(Fig. 2.7b). This can be understood from the fact that the indentation force F and membrane thickness h can be grouped into a dimensionless variable $q = \frac{1}{2\pi Ea}\left(\frac{F}{h}\right)$, where a is the membrane radius. With the help of such a linear relationship and the experiment results for 1.0μm thick GO/rGO films, the required force for mosquito to penetrate a 0.5 μm thick film is estimated to be within $50\sim250$ μN, which is still far above the typical range of force that mosquito exerts in penetrating human skin.

In some situations, GO/rGO films may be supported directly on the skin rather than in freestanding state. FE simulations have shown that the penetration forces in the presence of skin support are significantly larger than that in the freestanding case. Therefore, the freestanding model provides a safe, lower bound design for graphene-based protective wearable devices. Overall, this membrane indentation model provides theoretical support for the experimental observation that dry GO/rGO films of 0.5∼5.0μm thickness can be sufficiently stable mechanical barriers to mosquito fascicle insertion.

2.5.3 Effect of Poisson's Ratio

In our FE simulations and theoretical analysis, we have taken the Poisson's ratio of GO/rGO film to be $\nu = 0.17$ [127]. It will be shown in this subsection that the detailed choice of ν will not significantly affect our conclusions.

Different Poisson's ratios are considered in both FE and theoretical models with the freestanding membrane (Fig. 2.8a, b). The relationships between indentation force and central deflection are shown in Fig. 2.8a with the membrane tensile strength of $S_t = 0.19$. It can be observed that the maximum difference in central deflection between the cases of Poisson's ratios $\nu = 0.1$ and $\nu = 0.4$ is less than 10% in both FE and theoretical results.

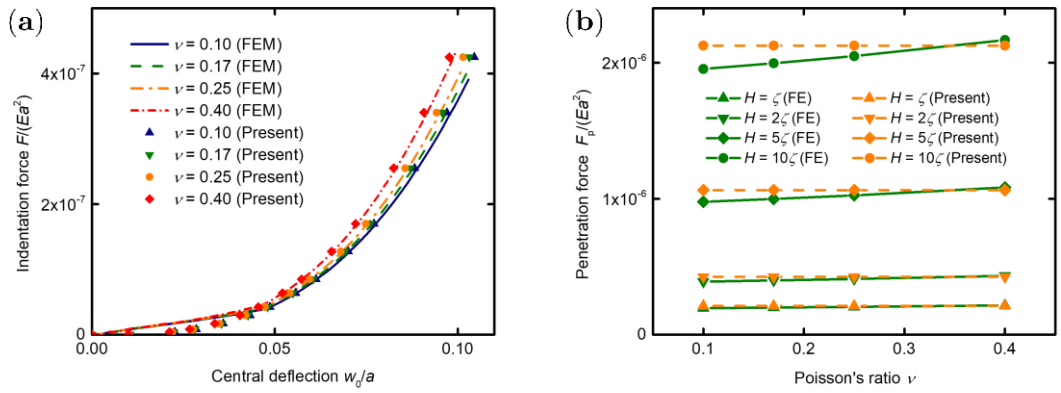

Fig. 2.8. Effect of Poisson's ratio on mechanical responses of a freestanding membrane under indentation. (**a**) Indentation force for different Poisson's ratios. The normalized membrane thickness is taken as $H = h/a = 2\zeta$ where $\zeta = 2 \times 10^{-4}$ is the reference thickness. (**b**) Effect of Poisson's ratio on the penetration force for different membrane thicknesses.

Fig. 2.8b shows that the CPFs do not exhibit significant dependence on Poisson's ratio. This insensitivity can be clearly found in the FE results for membrane thicknesses of $H = \zeta$ and 2ζ. For relatively large thicknesses of $H = 5\zeta$ and 10ζ, the CPFs increase slightly with Poisson's ratios. However, compared with the results for $\nu = 0.1$, the increases in CPF are all within 10%.

2.5.4 Effect of Indenter Tip Shape

If the indentation depth is much smaller than the radius of indenter tip, the tip profile can be approximated by a spherical or hyperbolic shape with the same radius of curvature at the apex of the tip. However, in the large indentation deformation cases, the contact region will cover a large portion of the indenter tip, and the stress distribution under the indenter tip will be sensitive to the shape of the tip. Compared with the existing solutions [78, 82, 129], the solution introduced in subsection 2.4.1 can be easily extended to indenter tip profiles of more complex forms without too many additional efforts.

Here we assume the tip profile to have a power-law shape:

$$f(\rho) = \frac{\rho^n}{n\Lambda}, \qquad 0 \le \rho \le \rho_t, \tag{2.17}$$

where n is a positive real number and Λ is a shape factor. When $n = 1$ and Λ is a positive constant, the tip in Eq. (2.17) reduces to a conical indenter; when $n = 2$ and $\Lambda = \rho_t$, the tip becomes a hyperbolic or approximately spherical shape; and when $n \to \infty$ and $\Lambda = \rho_t^{n-1}$, flat punch indenter can be obtained (Fig. 2.9a). For some irregular tip profiles, certain number of power-law terms in Eq. (2.17) with different n values can be superimposed to fit the given profiles. However, the present solution only allows the contact region to expand continuously starting from the center, which means that the tip profile must be described by a convex function.

By adopting the tip profile in Eq. (2.17), the deflection of the membrane in the contact region $0 < \rho < \rho_c$ can be written as

$$W = \bar{d} - \frac{\rho^n}{n\Lambda} \tag{2.18}$$

and the radial stress in the membrane as

$$S_r = \frac{c_1}{2} - \frac{\rho^{2n-2}}{8n(n-1)\Lambda^2}. \tag{2.19}$$

In the noncontact region, the deflection and radial stress are of the forms

$$W = q^{\frac{1}{3}} \sum_{m=0}^{\infty} a_{2m-1} \left(1 - \rho^{\frac{4m+2}{3}}\right), \tag{2.20}$$

$$S_r = \frac{3}{2} q^{\frac{2}{3}} \sum_{m=0}^{\infty} b_{2m-1} \rho^{\frac{4m-2}{3}}, \tag{2.21}$$

respectively. Like the derivation process in subsection 2.4.1, applying the boundary and continuity conditions Eqs. (2.11) and (2.12) results in the following system of equations which can give a closed-form solution:

$$\begin{cases} \sum_{m=0}^{\infty}(4m+1-3v)b_{2m-1}=0, \\ \frac{2}{3}q^{\frac{1}{3}}\Lambda\sum_{m=0}^{\infty}(2m+1)a_{2m-1}\rho_c^{(4m-3n+2)/3}=1, \\ \bar{d}=W^{+}(\rho_c)+\frac{\rho_c^{n}}{n\Lambda}, \\ c_1=2S_r^{+}(\rho_c)+\frac{\rho_c^{2n-2}}{4n(n-1)\Lambda^2}. \end{cases} \tag{2.22}$$

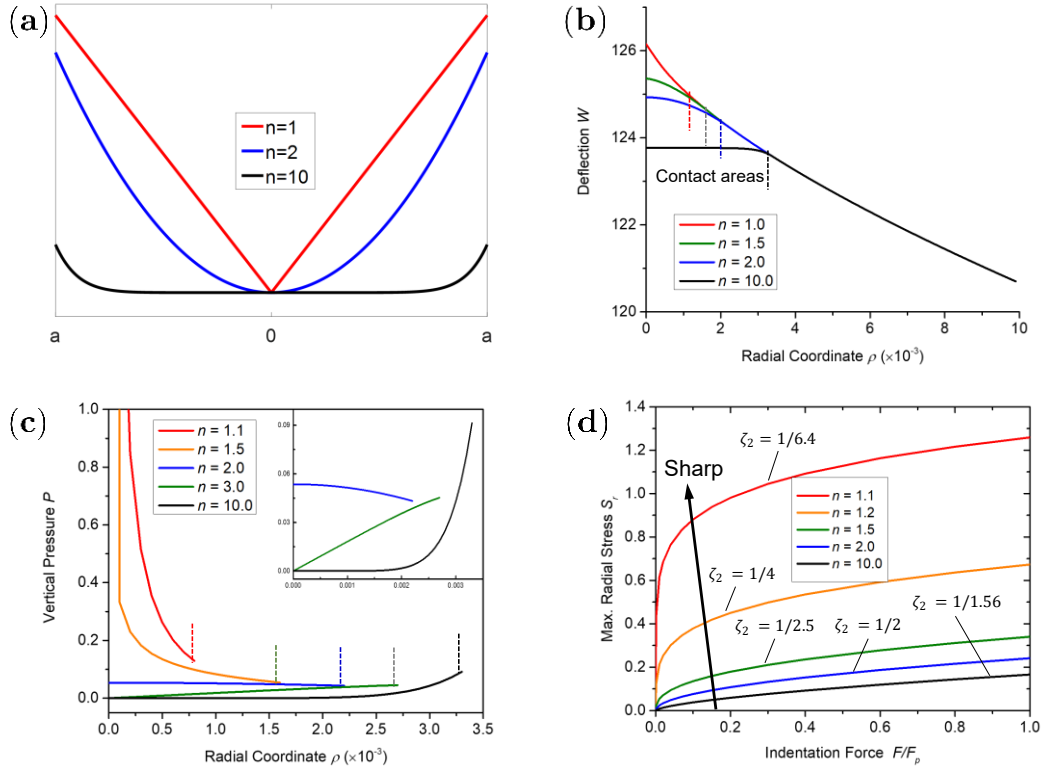

Fig. 2.9. Indenter tips with power-law shapes. (**a**) The tip profiles with different powers. (**b**) The deformed configurations of thin film for different shapes of indenter tip. (**c**) The vertical pressure distributions under the tip for different shapes of indenter tip. (**d**) The evolution of maximum radial stress in the thin film for different shapes of indenter tip.

Fig. 2.9b shows the deflection distribution of the membrane for different shapes of indenter tip. The tip profile has little influence on the deformation outside the contact area if the indentation load is the same. Therefore, the maximum membrane deflection is mainly

determined by the tip profile in these cases. In addition, it can be found from Fig. 2.9b that the contact area increases with the value of n, or decreases with the sharpness of the tip. The pressure distributions in the contact area are shown in Fig. 2.9c. When the tip approaches to be conical (i.e., $n \to 1$), corresponding to a point-load problem, the pressure is singular in the center of the membrane. In experiment, however, plastic zone will form near the tip and help reduce stress concentration. With a small value of n, the maximum pressure occurs in the center of the membrane; while for a blunter tip, the maximum pressure position will move to the edge. As n increases from 1 to 10, the pressure distribution curves transform from a convex to concave shape when n is about 2, and transform to the convex shape again when n continues to increase.

Since no friction is considered between the indenter tip and the membrane, the maximum membrane radial stress always occurs in the center whatever tip profiles are adopted. Fig. 2.9d shows how the maximum stress changes with loading for different tip profiles. During the loading process, the maximum stress increases rapidly in the beginning stage, but the increasing rate slows down as the indentation force gets larger, due to the reason that as the membrane is bulged, the resistance of the membrane to vertical load is enhanced. The curves of maximum stress can be approximately fitted using the scaling law

$$\frac{\bar{\sigma}_r}{E} = \zeta_1 \left(\frac{F}{F_0}\right)^{\zeta_2} \tag{2.23}$$

where ζ_1 and ζ_2 are constants for a given tip profile. Specifically, for the hyperbolic or approximately spherical tip profile (i.e., $n = 2$), the square root relation holds between the maximum radial stress and the indentation force. Besides, for a blunt indenter tip (e.g., $n > 2$), the distribution of maximum radial stress is insensitive to the tip profile and only has small changes when n increases from 2 to 10.

2.6 Summary

Considering the superior mechanical properties and functionality of graphene-based thin films, the possibility of applying GO/rGO films to wearable devices with mosquito bite prevention was explored by combined methods of experiment, theoretical modeling and numerical simulations in this chapter. The fundamental interaction between graphene-based films and the globally important mosquito species, *Aedes aegypti*, was focused as a representative example study.

Live mosquito tests show that dry GO/rGO films can serve as effective molecular barrier to mosquito bite, benefiting from the good impermeability of graphene monolayers and the compact stacking of nanosheets. The skin-associated molecular attractants were trapped beneath these graphene-based thin films and thus unavailable to mosquitos' olfactory and gustatory receptors. However, in wet environments such as films smeared with human sweat or water, the effect of molecular barrier became invalid, and the films failed to protect the skin from mosquito bite.

The results from microneedle penetration test show that rGO films remain some mechanical resistance even in wet environment. To estimate the resistant capability of wet rGO films to mosquito bites quantitatively, the membrane indentation modeling and associated finite element simulations were conducted. It turned out that the freestanding rGO films with thickness of $0.5\mu m$ could serve as a mechanical barrier to mosquito bite, implying that the same films attached on the skin or fabrics are safer from mosquito bite. The wet GO films, however, became hydrogel state and too soft to resist mosquito bites.

The GO and rGO thin films can be potential candidates to the mosquito bite resistant materials used in wearable devices, yet some challenges remain to be solved. For example, the breathability of rGO films is relatively poor even in wet state; wet GO films easily disintegrate under small mechanical loading, though they have good breathability. Methods to increase breathability while remaining mechanical properties and those to enhance mechanical performance while remaining breathability (e.g., crosslinking) need to be developed to solve these problems. Relevant studies will be done in the future.

Chapter 3 Shear Resistant 2D Material Thin Films for Wearable Devices

3.1 Introduction

The experiment parts in this chapter were designed and performed by our collaborator Prof. Robert H. Hurt group (including Cintia Castilho and Yiheng Xie) at Brown University.

It is clearly promising to integrate 2D material thin films in wearable devices considering the excellent properties of these films such as conductivity and breathability. However, the responses of these thin films under complex mechanical loadings are underexplored, which limits the application of 2D material thin films in relevant fields.

When embedded in wearable devices, the 2D material thin films are supported by and attached to the network frames formed by fabrics or other fiber materials. Under stretch, bending and distortion of the wearable devices in daily life, the embedded thin films will be exerted by combined forms of loading. The membrane indentation test exhibits the performance of 2D material thin films in stretching and bending, while it is still unknown how their behavior is under shear loading and how the failure happens on the interfaces with other solids. These questions will be discussed in this chapter through the lap shear test.

On the other hand, the interlayer cohesion energies of few-layer 2D crystal films are reported to be in the range of $50\sim500\ \mathrm{mJ/m^2}$ [130, 131]. By comparison, these values are much lower than the fracture energies of polymers that are typically toughened by covalent bonding and chain entanglement [132, 133]. Therefore, the interlayer toughness is an important limitation to the practical applications of 2D materials. In addition, the interfacial adhesion energy between 2D materials and solid substrate is also of the same significance.

This study will also investigate the cohesive and adhesive (interfacial) failures of multi-layer 2D material films.

3.2 Methods and Models

By adopting the lap shear test where 2D material thin films serve as the adhesive and polymer plates as the adherends, the shear deformation and interfacial failure behavior of the films can be characterized by experimental means. Two representative thin films prepared from liquid phase deposition, GO and $MoSe_2$ films, were adopted in the experiment. A lap shear model with a pre-crack in the adhesive was developed to explain the distinct behavior of GO and $MoSe_2$ films as well as the extraordinary fracture energies of multilayer 2D material thin films compared with their few-layer counterparts.

3.2.1 Characterization and Experiment

The GO and $MoSe_2$ thin films were prepared from aqueous stock suspensions using drop casting method. The GO suspensions were obtained by a modified Hummers' method [120] and the $MoSe_2$ suspensions by organolithium chemical exfoliation [134]. The nanomaterial aqueous suspensions were drop-casted onto a cleaned polyester substrate strip of $5\text{cm} \times 0.5\text{cm}$, and the dimensions of the multilayer film were $2\text{cm} \times 0.5\text{cm}$. Immediately after, an identical polyester strip was placed above the suspension. The GO samples were then left to dry for 48h at room temperature (22°C), or inside an oven at 60°C to 70°C. The $MoSe_2$ samples were left to dry for 48h at room temperature inside a glove box.

The thicknesses of the thin films range from 0.2 to 5μm. Lateral dimensions characterized by SEM are 0.5~2.0μm for GO and $< 0.4\mu\text{m}$ for $MoSe_2$ (Fig. 3.1a, b). The

volume-weighted average lateral sizes are 1.0μm for GO and 0.36μm for $MoSe_2$. Both films have the similar structures as reported before [18].

The overlap region of the polymer substrate strips contains the nanosheet film. The free ends of the two polymer strips were grasped in the tester and stretched uniaxially in constant speeds. Tests were performed at speeds from 0.01 to $1mm/min$, and results show no significant effect of loading speed within this range.

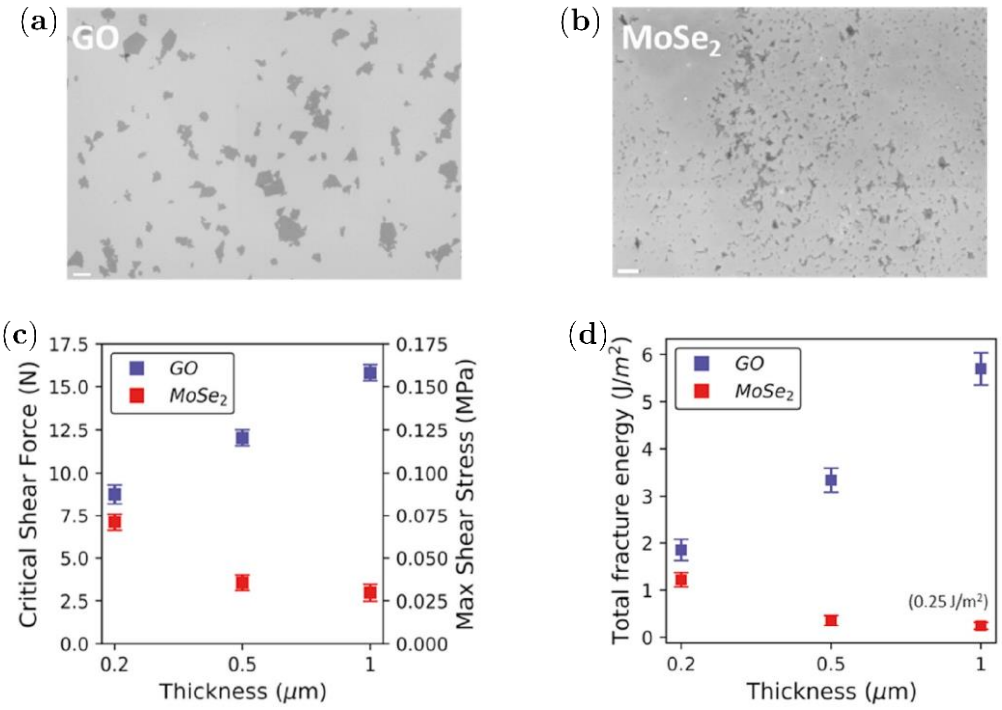

Fig. 3.1. Characterization and lap shear tests of GO and $MoSe_2$ thin films. (**a, b**) SEM images of as-produced GO and $MoSe_2$ nanosheets on silicon surfaces. Scale bar, $1\mu m$. (**c**) Measured critical forces and maximum shear stresses for GO and $MoSe_2$ films of varying thicknesses. Data is presented as mean ± s.e.m. (**d**) Fracture energies for GO and $MoSe_2$ films of varying thicknesses. Data is presented as mean ± s.e.m. All tests were performed at speed of $1mm/min$.

Two failure modes can be identified via the digital optical scanning: the cohesive failure occurred within the thin film and the interfacial failure occurred along the interfaces. In fact, most samples show a mixed mode failure. From the load-displacement data, we can

calculate the fracture energy of the thin film. The results (Fig. 3.1d) show that GO films have basically higher fracture energies than $MoSe_2$ films, probably due to larger aspect ratio of GO nanosheets and more frictional energy dissipation. However, an obvious phenomenon is that the GO and $MoSe_2$ films show the opposite behavior on critical shear force and fracture energy with respect to the film thickness (Fig. 3.1c, d). Besides, the fracture energies of the two films are much larger than interlayer cohesion energies of few-layer 2D crystal films, and close to fracture energies of polymers. This may be due to the energy dissipation and chaotic crack motion during nanosheet film disassembly at the crack tip.

3.2.2 Lap Shear Modeling

To explain the different dependence of GO and $MoSe_2$ films on film thickness and understand the failure mechanics of 2D material films under shear, a lap shear model with a pre-existing edge crack within the adhesive was proposed (Fig. 3.2). Since multilayer 2D material thin films are laminate materials comprising of massive stacking nanosheets, many defects such as voids and wrinkles exist in the films [124, 125], acting as microcracks and being ready to propagate under loading. Therefore, in the mechanical model the edge crack is used to simulate a critical defect (near the location of maximum local stress) in the thin film, which is thought to be responsible for the initiation of failure. Under lap shear loading conditions, stress concentration regions occur in the thin film near the corners attached to the middle part of substrate (denoted by red dots in Fig. 3.2, as opposed to the corners attached to the substrate edge). The edge crack was thus placed in the left half of the thin film on the consideration that cracks usually start to develop first in high stress regions. The distance from edge crack to the nearest film-substrate interface was kept constant based on the assumptions that microcracks are uniformly distributed and crack density is

the same for thin films of different thicknesses. The latter assumption is made because all the samples in experiment were prepared with the same method and in the same environment. Only one end of the thin film needs to be focused since the structure (excluding the edge crack) and boundary conditions are centrosymmetric about the film center. The structural deformation in width direction can be ignored (i.e., the model is assumed to be in plane-strain state), because the width of the structure is much larger than the thicknesses of the thin film and substrates.

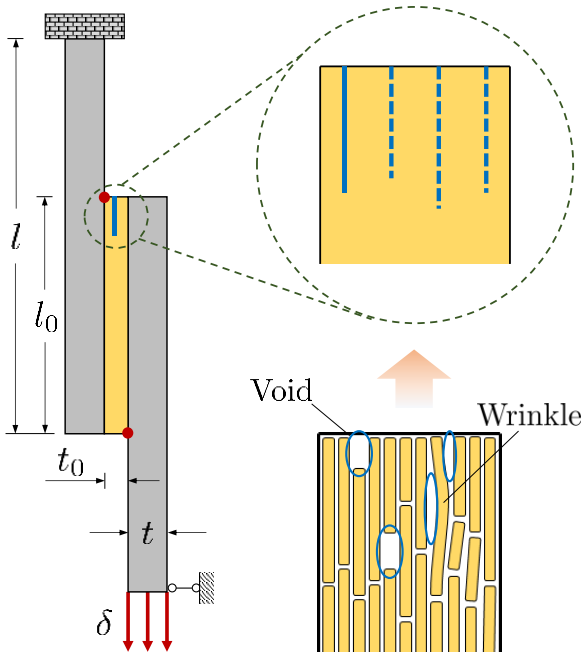

Fig. 3.2. The cracked lap shear model for finite element analysis. Defects like voids and wrinkles of nanosheets in the 2D material thin films act as pre-existing cracks on the edge. The cracks can be assumed to be uniformly distributed. Upon lap shear loading, the edge crack near the stress concentration zone starts to propagate first.

3.3 Finite Element Implementation

Due to the complicity of the cracked lap shear model, explicitly analytical solutions are difficult to seek. Therefore, finite element (FE) simulations were implemented to analyze

the fracture mechanics problem for the 2D material thin films in lap shear and study the effect of film thickness on the behavior of GO and $MoSe_2$ films.

3.3.1 Finite Element Setups

A plane-strain single-lap FE model (Fig. 3.2) was built based on the commercial computer-aided engineering software Abaqus (Dassault Systèmes Simulia Corp., Providence, RI). The geometry of the structure is consistent with that in experiment except that the aspect ratios of thin film and substrates are reduced to $1/50$ of the original ones for the computational efficiency consideration without loss of the essential physics. Reduction in aspect ratio of the structure does not change our conclusions, and its effect will be discussed in subsection 3.4.5.

Table 3.1. Parameters in the mechanical finite element model.

Parameters and description	Normalized parameters (value)
*Length of substrate l	$\bar{l} = l/l_{\mathrm{r}}$ $(= 700)$
Width of substrate w	$\bar{w} = w/l_{\mathrm{r}}$ $(= 100)$
Thickness of substrate t	$\bar{t} = t/l_{\mathrm{r}}$ $(= 100)$
Young's modulus of substrate E_{s}	$\overline{E_{\mathrm{s}}} = E_{\mathrm{s}}/E_{\mathrm{r}}$ $(= 4.48 \times 10^6)$
*Length of thin film l_0	$\overline{l_0} = l_0/l_{\mathrm{r}}$ $(= 400)$
Width of thin film w_0	$\overline{w_0} = w_0/l_{\mathrm{r}}$ $(= 100)$
Thickness of thin film t_0	$\overline{t_0} = t_0/l_{\mathrm{r}}$ $(= 0.2\sim2.0)$
*Film modulus in parallel direction E_{p}	$\overline{E_{\mathrm{p}}} = E_{\mathrm{p}}/E_{\mathrm{r}}$ $(= 2.28 \times 10^6)$
Film modulus in normal direction E_{n}	$\overline{E_{\mathrm{n}}} = E_{\mathrm{n}}/E_{\mathrm{r}}$ $(= \overline{E_{\mathrm{p}}}, 10\overline{E_{\mathrm{p}}}, 100\overline{E_{\mathrm{p}}}$ or $1000\overline{E_{\mathrm{p}}})$
Crack size a	$\bar{a} = a/l_{\mathrm{r}}$ $(= 0.5, 1.0$ or $2.0)$
Crack-to-interface distance d	$\bar{d} = d/l_{\mathrm{r}}$ $(= 0.1)$
*Prescribed displacement δ	$\bar{\delta} = \delta/l_{\mathrm{r}}$ $(= 1.0)$
(Optional) Loading force F	$\bar{F} = F/(E_{\mathrm{r}}\bar{w}l_{\mathrm{r}})$

* Values of the normalized parameters may vary in subsections 3.4.3 and 3.4.5.

Structural and material parameters used in the FE model are listed in Table 3.1. Mechanical properties of polymeric substrates were from the information provided by the vendor and verified through uniaxial tension test, while properties of 2D material thin films were measured through membrane indentation experiment. Unless otherwise stated, mechanical properties of GO films are used for the thin film in the FE model, and the effect of different film properties will be discussed in subsection 3.4.4. In Abaqus, the parameters were normalized using the characteristic length $l_{\mathrm{r}} = 1\mu\mathrm{m}$ and reference modulus $E_{\mathrm{r}} = 1\mathrm{kPa}$. All dimensionless variables are represented by symbols with a bar above.

Both the thin film and substrates were meshed by 4-noded bilinear quadrilaterial, reduced integration, solid elements (CPE4R). At least 4 layers of elements were meshed along the film thickness. The mesh was refined in the film and substrate regions near the edge crack. Translational and rotational degrees of freedom of the edge of the left substrate in Fig. 3.2 were fixed, while for the edge of the right substrate, only transversal movement was fixed, and prescribed displacement was applied in the longitudinal direction.

3.3.1 Results

The catastrophic failure of the thin film is determined by the condition under which cracks in the film start to propagate. In the mechanical model, this condition was assumed to be the failure criterion for brittle materials: $\bar{G} = \overline{G_{\mathrm{c}}}$ [105, 135] where $\bar{G}$ and $\overline{G_{\mathrm{c}}}$ are the energy release rate (ERR) and critical ERR of the edge crack tip, respectively. Here and in other parts, $\overline{(\cdot)}$ stands for dimensionless variables. The assumption of the ERR-based failure criterion is supported the experiment results that the film failure processes exhibit typical brittle failure features. Anisotropic materials are considered for the thin film in FEM

calculations since 2D material thin films generally have a smaller elastic modulus in the normal direction $\overline{E_{\mathrm{n}}}$ compared to that in the parallel direction $\overline{E_{\mathrm{p}}}$ [127]. Different modulus ratios of $\overline{E_{\mathrm{p}}}/\overline{E_{\mathrm{n}}}$ are considered (Fig. 3.3a, b), and in particular, $\overline{E_{\mathrm{p}}}/\overline{E_{\mathrm{n}}} = 1$ represents the case of isotropic film material as reference. The calculated ERRs in all cases in Fig. 3.3a decrease with film thickness when the film is thin, while turn to increase for thicker films. This implies that the critical shear force at catastrophic failure of the thin film first increases and then decreases with film thickness, consistent with the observed experiment results for GO films (Fig. 3.3c). The ERR simulation results also show that compared to the isotropic film, responses of anisotropic thin films are more sensitive to film thickness.

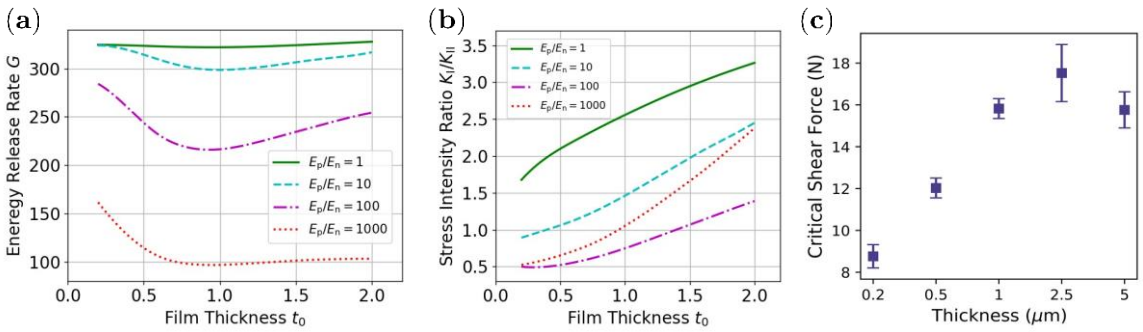

Fig. 3.3. Shear-to-tensile failure mode transition. (**a**) Energy release rates (ERRs) at the crack tip for films of different thicknesses. $\overline{E_p}$ and $\overline{E_n}$ denote elastic moduli of the film in the directions parallel and normal to the film basal plane, respectively. (**b**) Ratios of mode-I and mode-II stress intensities of crack tip for films of different thicknesses. In all cases in (**a, b**), $\overline{E_p}$ was chosen as $2.28GPa$ [21] and the crack size as $\bar{a} = 1.0$. (**c**) Extended data on the critical shear forces for GO films of varying thicknesses. Data is presented as mean ± s.e.m. All tests were performed at testing speed of $1mm/min$.

The upturn trend of the ERR curves in Fig. 3.3a, or the downturn trend of the critical shear force curve for GO film in Fig. 3.3c, can be explained by a shear-to-tensile failure mode transition. The ratio of stress intensities $\overline{K_{\mathrm{I}}}/\overline{K_{\mathrm{II}}}$ (Fig. 3.3b) reflects the relative proportion of the two driving force components (i.e., mode-I and mode-II ERRs) for the crack

propagation, from which we can identify the dominant failure mode in the thin film failure process. The simulation results show that shear failure mode dominates in small film thickness regime, while tensile failure mode becomes more significant when the films are thicker. This failure mode transition can be identified in all cases of anisotropic film materials though is not obvious for the isotropic film material ($\overline{K_{\mathrm{I}}}/\overline{K_{\mathrm{II}}}$ being always greater than 1). Besides, compared with the isotropic film, anisotropic films have a smaller proportion of tensile failure mode, probably due to their weaker stiffness and load-bearing capability in the normal direction.

The modelling identifies two major contributions to the shear-to-tensile failure mode transition as film thickness increases: weakening substrate confinement on the edge crack and increasing rotational deformation near the film edge with film thickness. First, the two substrates confine the film from deforming in the normal direction though allow its shear deformation in the parallel direction. The calculated crack opening profiles (Fig. 3.4a) show that the substrate confinement on the edge crack is weakening as the film thickness increases. Therefore, for very thin films (i.e., film thickness smaller than the typical crack size), the confinement effect of substrate is very strong, which makes the crack fail mainly in shear mode. For thick films (i.e., film thickness greater than the typical crack size), however, the confinement effect of substrate is reduced, and the crack increasingly fails in tensile mode. To better demonstrate the confinement effect of substrate, the lap shear model was reconsidered under the same conditions except the two substrates being set as rigid. In this scenario, we can exclude the influence of elastic deformation of substrate and focus our attention on how the thin film is constrained by the substrates. As shown in Fig 3.5, the driving force of crack tip under rigid substrate $\overline{G_{\mathrm{rigid}}}$ is very high when film thickness is

small, implying that the crack opening is strictly confined. As film thickness increases, however, the driving force decreases dramatically and becomes flat gradually, which clearly characterizes the relaxation of confinement effect of substrate on the edge crack. On the other hand, the shear forces from two substrates are applied on the thin film in the opposite directions and cause rotational deformation of the joint part. The rotational deformation increases with film thickness, resulting in larger load component projected in the normal direction and improved proportion of tensile failure mode.

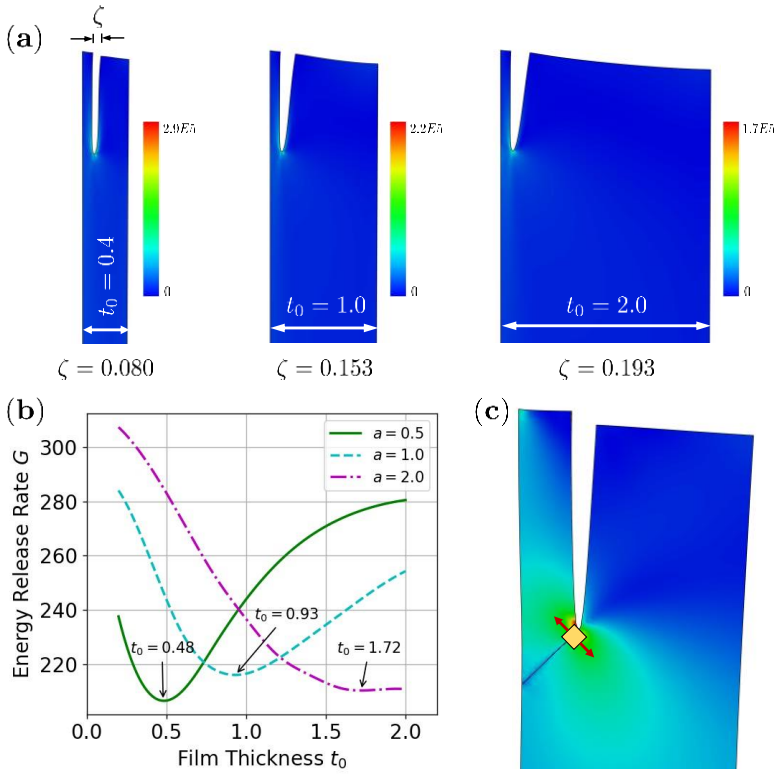

Fig. 3.4. The dependence of failure mode in lap shear test on the film thickness. (**a**) Edge crack openings for films of different thicknesses. The colors indicate von Mises stress distribution in the film. (**b**) Effect of crack size on the crack tip ERR and the shear-to-tensile failure mode transition. The film material with $\overline{E_p}/\overline{E_n} = 100$ was used. (**c**) Crack propagation direction in the film under lap shear loading conditions. The arrows indicate the directions of maximum opening stress in front of the crack tip.

The experimentally observed different critical shear force behavior for GO and $MoSe_2$ films (Fig. 3.1c) can be explained by the shear-to-tensile failure mode transition. The FEM results in Fig. 3.4b show the effect of edge crack size on the crack tip ERR. For a smaller crack size, the critical point of ERR curve moves toward left, implying that the film thickness regime dominated by shear failure mode gets shrunk. This is because small edge cracks (compared with film thickness) cannot be confined by substrate as strictly as larger ones (see subsection 3.4.1) and thus prefer tensile failure. Since we assume that edge crack size is proportional to the feature size of 2D nanosheets (Fig. 3.2), the disparity between lateral dimensions of GO ($\sim 1\mu m$) and $MoSe_2$ ($\sim 0.36\mu m$) nanosheets means that the crack size in $MoSe_2$ film should be much smaller than that in GO film. Therefore, compared with the crack size in $MoSe_2$ film, the thickness of $MoSe_2$ film used in experiment is not small enough to induce a strong confinement effect of substrate. In other words, the failure in $MoSe_2$ films is always dominated by tensile failure mode, and the measured critical shear force always decreases with film thickness in the studied regime in experiment.

Given the lateral dimensions of 2D nanosheets, there always exists an optimum film thickness for the shear stability of 2D material thin films due to the shear-to-tensile failure mode transition. For films composed of small nanosheets, the film thickness should be as small as possible; whereas for those composed of relatively large nanosheets, the optimum thickness should be determined by the proposed model together with lap shear experiments. This optimal shear stability has potential applications in many fields, such as flexible electronics and wearable devices, where 2D material thin films act as adhesive or bridging part between substrates and primarily bear shear forces. One should also note that the present model cannot make quantitative predictions on the shear stability for various kinds of 2D

material thin films, because many other factors, such as intrinsic properties of 2D nanosheet, functional groups, water content [136] and surface roughness [137], can have complex effects that are difficult to be considered in the present model.

The mechanical model with an edge crack in the thin film contains features of cohesive failure observed in experiment, while the post analysis on crack propagation can be used to further explain the phenomenon of interfacial failure (Fig. 3.4c). Since the edge crack is under a mixed mode (mode-I and mode-II) loading, the maximum opening stress direction in front of the crack tip is deflected clockwise from the normal direction, and the crack will propagate toward the film-substrate interface. The subsequent propagation path, however, depends on the sophisticated structural environment around the crack tip, as there will be many new defects created in the film or on the film-substrate interface under loading [138]. Without significant interference of defects and impurities the edge crack front will reach the interface and continue to propagate along the interface, forming interfacial failure of the thin film; otherwise, the crack may propagate following other random paths within the film if defects and weak nanosheet linkages are dense around the crack tip, forming cohesive failure of the thin film.

3.4 Discussion on Shear-to-Tension Transition

The effects of some factors in FE simulations that may influence the fracture behavior of the films will be discussed in this subsection. These factors include the material properties and geometries of the thin film, substrate and edge crack. The shear-to-tensile failure mode transition may also be affected by the choice of these parameters.

3.4.1 Effect of Material Anisotropy

The film is assumed to be anisotropic in the mechanical model due to its weaker properties in the normal direction than in the parallel direction. More specifically, the thin film is considered transversely isotropic, i.e., isotropic within the basal plane while possessing different modulus in the out-of-plane direction. Taking the loading direction as x, the direction along width (inward) as y and the normal direction as z according to the right-hand rule, the constitutive relationship for the transversely isotropic film can be written as:

$$\boldsymbol{\sigma} = \mathbf{C}\boldsymbol{\varepsilon}, \tag{3.1}$$

where $\boldsymbol{\sigma} = \{\sigma_{xx}, \sigma_{yy}, \sigma_{zz}, \tau_{xy}, \tau_{xz}, \tau_{yz}\}^{\mathsf{T}}$ and $\boldsymbol{\varepsilon} = \{\varepsilon_{xx}, \varepsilon_{yy}, \varepsilon_{zz}, \gamma_{xy}, \gamma_{xz}, \gamma_{yz}\}^{\mathsf{T}}$ are stress and strain vectors, respectively. The elastic matrix $\mathbf{C}$ can be expressed as:

$$\mathbf{C} = \begin{bmatrix} \mathbf{d}_{11} & \mathbf{0} \\ \mathbf{0} & \mathbf{d}_{22} \end{bmatrix}^{-1}, \tag{3.2}$$

where

$$\mathbf{d}_{11} = \begin{bmatrix} 1/E_x & -\nu_{yx}/E_x & -\nu_{zx}/E_z \\ -\nu_{xy}/E_x & 1/E_x & -\nu_{zx}/E_z \\ -\nu_{xz}/E_x & -\nu_{xz}/E_x & 1/E_z \end{bmatrix}, \tag{3.3a}$$

$$\mathbf{d}_{22} = \begin{bmatrix} 2(1+\nu_{xy})/E_x & 0 & 0 \\ 0 & 1/G_{xz} & 0 \\ 0 & 0 & 1/G_{xz} \end{bmatrix}. \tag{3.3b}$$

In Eqs. (3.2) and (3.3), $E_x = E_{\mathrm{p}}$ and $E_z = E_{\mathrm{n}}$ are the moduli of the thin film in the parallel and normal directions, respectively; ν_{ij} and ν_{ji} $(ij = xy, xz)$ are Poisson's ratios in i-j plane with $\nu_{ji} = \nu_{ij}E_j/E_i$; and G_{xz} denotes the shear modulus of the thin film in x-z plane.

The elastic matrix $\mathbf{C}$ has five independent components; however, only two (E_x and ν_{xy}) can be determined using the present experimental tools. To investigate the effect of film elastic modulus in the normal direction (E_z), we take different values of $\eta = E_x/E_z$ with

E_x being fixed in FE simulations. For specific η, the values of ν_{xz} and G_{xz} are determined from Table 3.2. Some results have been shown in Fig. 3.3.

Table 3.2. Part of elastic constants of the thin film in FE simulations.

η	1	10	100	1000
ν_{xy}/ν_{xz}	1	2	4	16
$^*G_{xy}/G_{xz}$	1	5	50	500

$^*\ G_{xy} = E_x/2/(1+\nu_{xy})$.

3.4.2 Effect of Substrate Confinement

The edge crack has different opening displacements in thin films with different thicknesses (Fig. 3.4a) due to the weakening confinement effect of the substrates on crack opening. This confinement effect can be best demonstrated by setting the substrates as rigid and focusing on the response of the edge crack. The crack tip ERR with rigid substrates ($\overline{G_{\text{rigid}}}$) is a quantitative measure of the substrate confinement because strict substrate confinement on the crack in the normal direction leads to high ERR under the lap shear loading.

Fig. 3.5 shows the crack tip ERR under rigid substrates for thin film materials of different anisotropy. In all cases, the ERR is much higher for small film thickness than that for relatively large film thicknesses. When the film is very thin, the opening displacement of the crack in the thin film is strictly confined by the rigid substrates, and tensile deformation is thus very difficult to happen; whereas when the film is relatively thick, the substrate confinement will be significantly reduced, and tensile failure mode will gradually become dominant in place of shear failure.

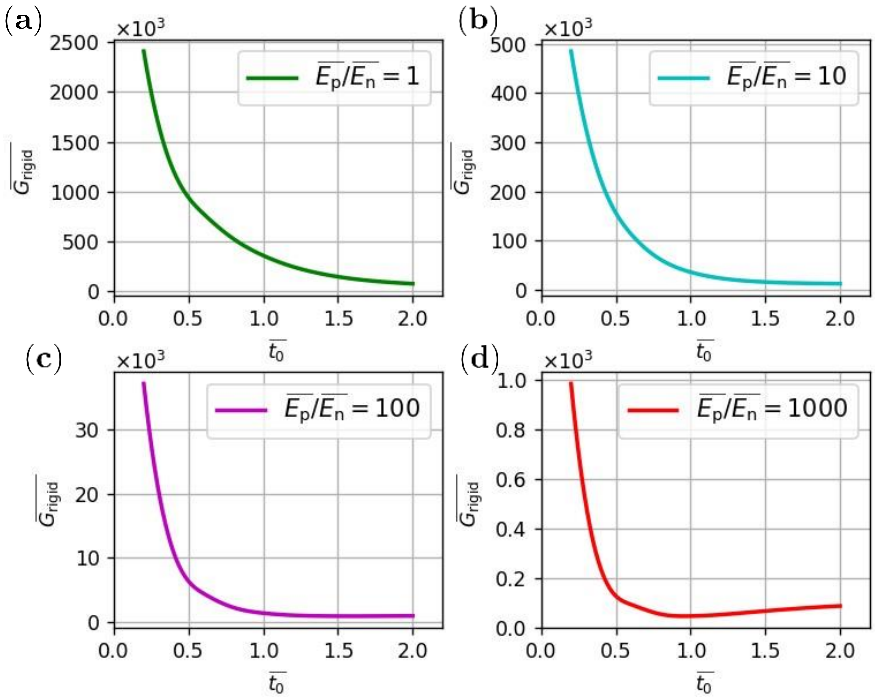

Fig. 3.5. The crack tip ERR for thin films of different anisotropic materials confined between rigid substrates. (**a-d**) The modulus ratio of thin film $\overline{E_p}/\overline{E_n} = 1, 10, 100, 1000$, respectively. In particular, the thin film material is isotropic for the case of $\overline{E_p}/\overline{E_n} = 1$.

In all cases in Fig. 3.5a-d, the substrate confinement decreases dramatically with increasing film thickness in the range of $\overline{t_0} < 0.5$, and changes little as the film thickness continues to increase. Nonetheless, the maximum values of ERR under rigid substrate are prominently different in the four cases. Since the film modulus in the parallel direction $\overline{E_{\mathrm{p}}}$ is fixed, the larger the modulus ratio of $\overline{E_{\mathrm{p}}}/\overline{E_{\mathrm{n}}}$, the weaker the thin film in normal stiffness. Therefore, Fig. 3.5 indicates that for thin films made of weaker materials in the normal direction, the maximum value of $\overline{G_{\mathrm{rigid}}}$ is smaller and the crack opening is less confined by the substrates, presumably due to the larger compliance of the thin film which facilitates larger normal deformation and causes smaller shear driving force near the crack tip.

3.4.3 Effect of Pre-crack Size with Rigid Substrates

Since the nanosheet lateral dimension and crack size of $MoSe_2$ films are much smaller than those of GO films, it is of great interest to study the influence of defect size on the substrate confinement for the two types of thin films and the shear-to-tensile failure mode transition.

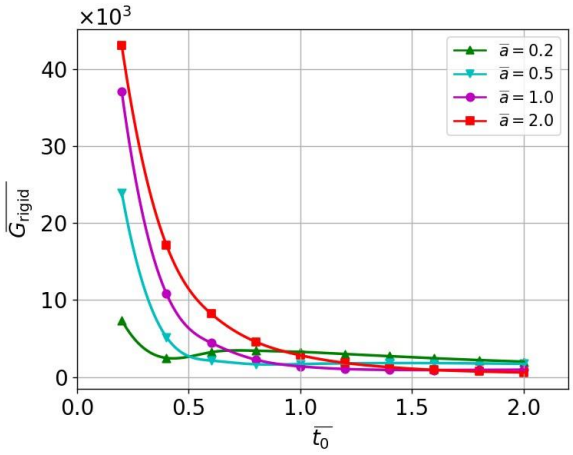

Fig. 3.6. Effect of crack size on crack tip ERR for films between rigid substrates.

The effect of crack size on substrate confinement is shown in Fig. 3.6 by considering edge cracks of different sizes with rigid substrates. In all cases, the substrate confinement (i.e., the crack tip ERR with rigid substrate $\overline{G_{\text{rigid}}}$) is strong for films of small thickness, while much weaker for relatively thicker films. This provides evidence for the general existence of the shear-to-tensile failure mode transition for 2D nanosheets of different lateral dimensions when film thickness changes.

In small film thickness regime (e.g., $\bar{t}_0 < 0.5$ in Fig. 3.6), the substrate confinement on crack opening is much weaker for smaller cracks, because the tensile deformation of small defects (compared with film thickness) in thin films cannot be effectively constrained by the substrates. This is consistent with our conclusion from experiment and simulation that

the thicknesses of $MoSe_2$ films used in experiment are not small enough (compared with defect sizes in film) to induce strong substrate confinement, and thus no shear-to-tensile failure mode transition happens for $MoSe_2$ films in our experiment. For the same reason, in the large film thickness regime in Fig. 3.6, all crack sizes are small by comparison and substrate confinements in all cases become very weak.

3.4.4 Effect of Thin Film Stiffness

Primarily determined by the mechanical and chemical properties of 2D nanosheets (e.g., intrinsic stiffness, and interlayer functional groups), $MoSe_2$ and GO films have some difference in elastic modulus in the parallel direction ($\overline{E_p}$). To demonstrate the effect of this difference, the crack tip ERR was calculated using different film moduli in the parallel direction (Fig. 3.7a).

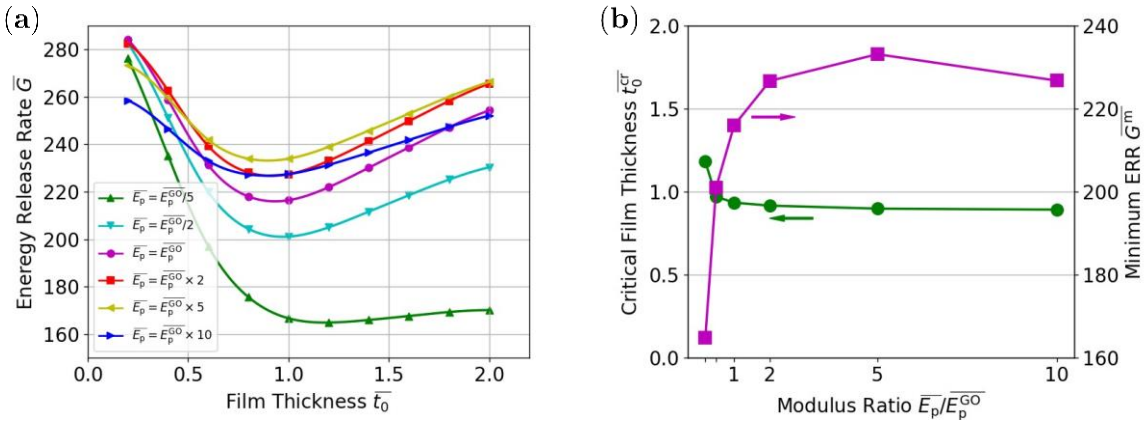

Fig. 3.7. Effect of film modulus in the parallel direction. (**a**) Variation of the ERR of crack tip with film thickness for different film moduli in the parallel direction. Here $\overline{E_p^{GO}}$ denotes the modulus $\overline{E_p}$ of the GO vdW film used in experiment. (**b**) Changes of critical film thickness (left axis) and corresponding ERR (right axis) for different film moduli in the parallel direction.

The crack tip ERRs in all cases in Fig. 3.7a tend to decrease in small film thickness regime while increase in large film thickness regime, indicating that all the corresponding

critical shear forces first increase and then decrease with film thickness. The critical film thickness at which the minimum of the ERR curve locates is closely associated with the shear-to-tensile failure mode transition. From the results shown in Fig. 3.7b, the film modulus in the parallel direction has no significant influence on the failure mode transition in the sense that the critical film thickness changes slightly with the film modulus in the parallel direction.

Fig. 3.7a also shows that when the thin film material is very soft (e.g., the case of $\overline{E_{\mathrm{p}}} = \overline{E_{\mathrm{p}}^{\mathrm{GO}}}/5$), the change in crack tip ERR after the minimum of the curve becomes inconsiderable. Basically, this implies that for soft films as the adhesive, the shear stability and critical shear force will not be reduced significantly above a critical film thickness. This phenomenon has great potential in applications where 2D material thin films are embedded between substrates with rough surfaces. Since the films are prepared by drop-casting and drying the nanosheet suspensions between polymer substrates, the film thickness will also vary if the substrate surfaces are not flat. Nevertheless, if the thin film is soft enough, e.g., with relatively small modulus or porous structure, the average film thickness can be tuned to be above the critical value so that the film shear stability will not be significantly weakened at troughs of the substrate asperity where the film is thickened.

3.4.5 Effect of Overlap Length

In the present study, the aspect ratio of the structure has been reduced to 1/50 that of the experimental sample to ensure precision of calculation and reduce computational cost. However, the reduced aspect ratio is still large enough to preserve the essential features and deformation modes of the original structure. To further demonstrate that the reduced aspect ratio has no significant influence on our conclusions, three additional FE models

with different overlap lengths were built. For each film length or overlap length $\bar{l}_0$, the length of the substrates and the prescribed displacement are adjusted correspondingly. Fig. 3.8 shows the effects of overlap length on the crack tip ERR and the stress intensity ratio at the crack tip.

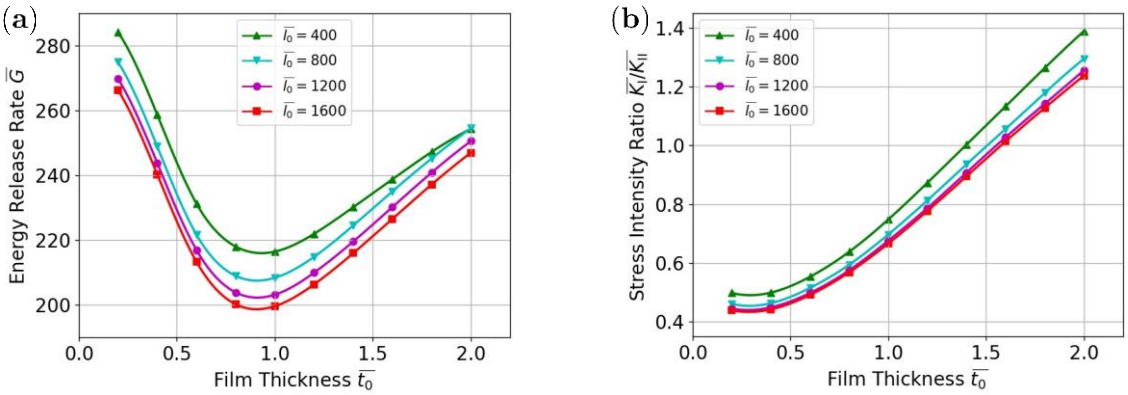

Fig. 3.8. Effect of aspect ratio of film/substrate. (**a**) Variation of the ERR at the crack tip with film thickness for different aspect ratios of the structure. (**b**) Variation of the stress intensity ratio at the crack tip with film thickness for different aspect ratios of the structure.

For different overlap lengths, there exists a minimum in the ERR curve (Fig. 3.8a), implying that the critical shear force should first increase and then decrease with film thickness irrespective of the aspect ratio of the film and substrates. On the other hand, the position of the minimum, i.e., the critical film thickness corresponding to the minimum ERR, only changes slightly (0.91~0.93) in different cases. Therefore, the influence of overlap length on the shear-to-tensile failure mode transition can be negligible. The magnitude of crack tip ERR in different cases, however, is influenced by the overlap length, i.e., the crack tip ERR is relatively low for large overlap lengths. This phenomenon can be explained through the expression of ERR associated with the structural compliance $\bar{C}$:

$$\bar{G} = \frac{1}{2}\bar{F}^2 \frac{\partial \bar{C}}{\partial \bar{a}}, \tag{3.4}$$

where $\bar{F}$ is the load applied on the structure. Since the edge crack remains the same, the structural compliance is less sensitive to the change in crack size $\bar{a}$ (i.e., $\partial \bar{C}/\partial \bar{a}$ decreases) as the lengths of the thin film and substrates increase, resulting in smaller ERR values for larger overlap lengths.

Similarly, the overlap length exhibits insignificant influence on the stress intensity ratio at the crack tip. All curves of $\overline{K_{\mathrm{I}}}/\overline{K_{\mathrm{II}}}$ in Fig. 3.8b keep increasing with film thickness and the magnitude show slight reduction as the overlap lengths increase. This implies that the proportion of shear failure mode (due to $\overline{K_{\mathrm{II}}}$) in the film failure process is increasing slowly as the overlap length increases, presumably due to the larger shear stress zone on the film-substrate interfaces and less rotational deformation of the joint.

3.5 Summary

In addition to the in-plane mechanical properties of multilayer 2D material thin films which have been widely studied, their shear behavior (along the direction parallel to the basal plane of the film) and interfacial interaction with solid substrates are also of significant importance and great interest if the films are applied to wearable devices. In this chapter, the lap shear tests for two types of 2D material thin films, GO and $MoSe_2$, as the adhesives were conducted to study their shear stability and failure behavior under shear.

Both thin film adhesives show brittle failure after a linear loading process. The fracture energies are much higher than the interlayer cohesion energies of few-layer 2D crystal films. The extraordinary fracture energies of multilayer films are associated with the mixed mode of cohesive and interfacial failure, which indicates chaotic and crooked crack

propagation paths in the adhesives of interlocking laminate structure. The critical shear force and fracture energy for both films show obvious dependence on the film thickness. However, the two quantities increase with the thickness of GO film, while decrease with that of $MoSe_2$ film.

A lap shear model with a pre-existing edge crack was proposed and analyzed with finite element method to interpret the results from experiment. The edge crack was used to simulate the interlayer defects in the thin film, which are most likely to initiate fracture under the lap shear loading. The analysis suggests that a shear-to-tensile failure mode transition exists associated with film thickness and crack size. In cases of small film thickness and large crack size, the crack opening is strictly confined by the substrate in the normal direction and shear failure mode is dominant; while in cases of large film thickness and small crack size, the substrate confinement becomes weak and the failure is dominated by tension mode. This shear-to-tensile failure mode transition results in a minimum ERR and a corresponding maximum critical shear force with respect to film thickness. The different dimensions of GO and $MoSe_2$ nanosheets and defect sizes in the films, together with the failure mode transition theory, account for their distinct behavior in experiment.

The mixed mode of cohesive and interfacial failure can also be explained by the proposed model. Under the mixed mode-I and mode-II loading, an edge crack will deflect to the interface between the thin film and substrate when defects are sparse locally, leading to the interfacial failure. However, if there are dense interlayer and intralayer defects near the crack tip, they may guide the crack propagation path to other random directions, leading to the cohesive failure.

Chapter 4 Necking-Affected Controlled Fragmentation of 2D Thin Films for Nanoribbon Fabrication

4.1 Introduction

Graphene nanosheets have drawn a lot of attention due to their high conductivity and potential applications in flexible photovoltaics and electronics used for functional wearable devices. However, the challenge arises that the 2D planar graphene nanosheets have zero energy bandgap. A feasible solution is graphene nanoribbon which is a strip of graphene nanosheet with nanoscale width. The electronic band structure of graphene is changed by introducing lateral confinement on charge carriers in the nanoribbons [110]. Furthermore, the energy bandgap size can be tuned by changing the nanoribbon width.

To synthesize graphene nanoribbons of narrow widths and high quality, various strategies have been explored [139]. These strategies can be divided into top-down and bottom-up schemes. The top-down scheme includes unzipping nanotubes by plasma etching or chemical cutting carbon nanotube, lithographic patterning and plasma etching of graphene nanosheet, and nanoparticle catalyzed cutting. The bottom-up scheme is mainly represented by the CVD and chemical synthesis methods. However, an all-around method is lacking that can produce high-quality, width-tunable graphene nanoribbons in large scale.

Among numerous fabrication methods which mostly adopted chemical routes, a purely mechanical strategy based on cold drawing has recently emerged as a powerful platform to produce structures at micron and sub-micron scales [140-144]. Cold drawing is a mature and widely adopted technique in the shaping of metallic and polymeric materials in industry. The application of cold drawing in polymers started in 1930s when the

mechanical properties of materials were found to improve after being cold drawn. Cold drawing can align polymer chains along the loading direction and make them oriented in a more crystalline manner. For a long time, cold drawing was mostly applied to single materials but recently, this technique has been revisited in composite structures and led to the discovery of “controlled fragmentation" as a particularly promising approach to producing nanostructures of various geometries with a simple and versatile strategy. In the novel cold drawing approach, local necking induced by uniaxial cold drawing of a ductile thermoplastic polymer gives rise to sequential, controlled fragmentation in an attached brittle target material (e.g., a brittle core inside a polymer fiber cladding or a brittle film on a polymer substrate), from which micron-sized rods and ribbons can be obtained. In this chapter, a theory of sequential fragmentation in cold drawing was built to help understand the underlying mechanisms and key control parameters. The theory shows that the fragmentation size depends on the interfacial shear strength, as well as the feature size and stiffness of the target material, and therefore can be reduced potentially toward nanoscale via increasing interfacial interaction and decreasing geometrical dimensions such as the core radius or film thickness.

4.2 Necking of Ductile Materials

In contrast to the common perception that necking and fracture are mostly to be avoided in material engineering, the discovery of controlled fragmentation by cold drawing has opened up a new research direction, where a combination of necking and fracture are being used to the benefit of fabricating desired micro- and nanostructures. In this process, a neck, with reduced sizes in the perpendicular directions to the loading, initiates in some ductile

materials like thermoplastic polymers upon uniaxial stretching and propagates the state to the distance without changing the shoulder profile (Fig. 4.1a). Studies of plastic necking in a material under tension can date back to the work of Considère [145], who proposed the critical condition for the onset of localization. Bridgman [146] pointed out the nonlinearity in necking problem and solved for the nonuniform stress distributions at the necking zone by adopting an approximate arcuated profile for the neck. On the other hand, with the development of computers and computational mechanics, numerical approaches such as finite element methods were used to investigate the deformation and evolution process of the necking zone in plastic materials under large strain [147-149].

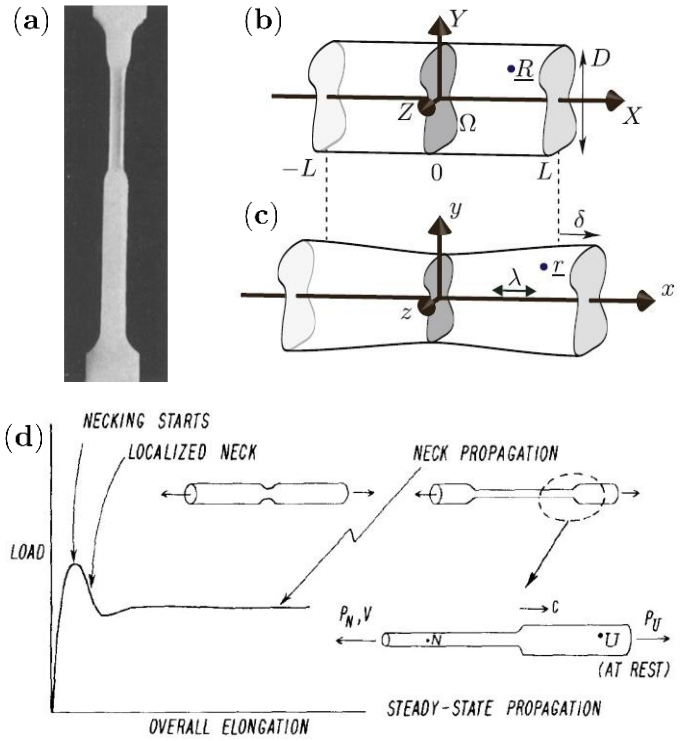

Fig. 4.1. Necking initiation and propagation in ductile materials. (**a**) Multiple-order necking in a polymeric bar [146]. (**b, c**) Reference and deformed configurations adopted in 1D models for slender solids [163]. (**d**) Overall load-elongation behavior in a tensile test from necking initiation till steady-state propagation [165].

The incipience of the necking phenomenon, as an important implication to material failure, was usually thought by engineers to occur when the tensile load reaches a maximum. From the stability point of view, the theory of bifurcation and uniqueness in plastic solids due to Hill [150] was used to determine the onset conditions of necking in nonlinear elastic [151] and elastic-plastic materials [152, 153] under tension, which could slightly deviate from those determined by the maximum load criterion. For incompressible elastic-plastic materials, it was shown that the strain at the maximum load serves as the lower bound to that determined from bifurcation, and the difference is smaller for slenderer specimens [153]. Specific interests on stability of necking under tension were also paid on elastic-plastic cylinders with circular cross-section [154] and arbitrary simply connected cross-section [155], as well as plain-strain sheets under uniaxial [156, 157] and biaxial [158] loadings.

Alternatively, approximate one-dimensional (1D) models focusing on slender solids [159, 160] were developed for nonlinear elastic specimens to study the (post-) bifurcation conditions leading to necking (Fig. 4.1b, c). Coleman and Newman [161] estimated the error due to such approximation to be the order of the fourth power of the specimen thickness, and derived the solutions exhibiting configurations with either a completely formed neck or periodic necks. Mielke [162] used the central manifold theorem to construct an asymptotically exact dimensional reduction approach from 2D or 3D continuum mechanics, which was later applied to prismatic solids possessing arbitrary cross-section and made of an orthotropic material [163]. Furthermore, the effect of rate-dependence of material behavior on necking retardation was studied numerically for viscoplastic materials [164] under the dimensional reduction modeling framework.

For some nonlinear elastic and elastic-plastic materials, failure may not immediately occur upon necking; instead, under continuous drawing the necking state can propagate over the entire specimen without any damage induced in the specimen (Fig. 4.1d). In both axisymmetric [165] and plane strain [166] scenarios, the steady-state neck propagation conditions for nonlinear elastic solids were derived from the continuity conditions of mass, momentum and energy, while fully three-dimensional analysis was necessary to determine the propagation state of the neck in inelastic solids. Specifically, in quasi-static, elastic case, neck propagation models showed that the deformation and stress states on both sides of necking zone are only related to the difference in strain energy in the two regions and thus can be solved merely from the knowledge of material constitutive relations (see details below). The evolution of specimen profile and stress/strain distributions during the entire loading history have been obtained based on finite element computation [167].

4.3 Sequential Controlled Fragmentation by Cold Drawing

Benefiting from the steady-state necking propagation in ductile materials, Shabahang et al. developed a nanostructure fabrication strategy by using simple uniaxial tension of the composite fiber systems containing thermoplastic polymers as the cladding and brittle materials like silicon and glass as the core [140]. Upon the cold drawing applied on the fiber cladding, the neck will form, grow and propagate from some location to the entire fiber. It can be observed that sequential fragmentation occurs in the fiber core along with continuing drawing of the fiber. What is of great interest is that the position of each fragmentation is always located near the necking zone (a region with the shoulder profile around the necking front). Therefore, the fragmentation follows the necking front to propagate over the entire fiber

and thus can be controlled by controlling the necking state, such as moving speed and terminating position. After dissolving the polymer cladding, large number of nanorods formed by the sequential fragmentation can be obtained.

This strategy is facile and versatile in that the cross-section of the fiber can be fabricated into many shapes in addition to the common circular one. For example, the cladding cross-section can be rectangular with brittle thin film materials as the core embedded in the cladding [140]. Upon continuing drawing, progressive fragmentation with necking propagation fractures the intact thin film into many small ribbons with microscale width. This process can be approximately described by a model which is equivalent in principle to the axisymmetric model for the circular cross-section fiber.

The fiber cold drawing system can also be modified into the film-substrate configuration for the fabrication of micro/nano scale ribbons [140, 141, 144]. This approach is suitable for monolayer or few-layer 2D material thin films since these synthesized films are usually deposited on a substrate. As opposed to the core-cladding fiber system, the film-substrate system may lead to irregular crack propagation along the width direction, probably due to asymmetric substrate confinement on the thin film. By coating the thin film with another polymer layer (e.g., PMMA layer), ordered fragmentation can be achieved [141, 144]. In this way, monolayer graphene ribbons with width of $\sim 0.93\mu m$ can be obtained by cold drawing of the polycarbonate substrate. Therefore, both the rectangular fiber and the film-substrate systems can be utilized with the cold drawing method to fabricate 2D material ribbons in nanoscale by further reducing the ribbon width.

Despite the systematic experiment works on the necking-induced controlled fragmentation, a theory of the cold drawing process is lacking considering the interfacial

interactions between a necking ductile material and an attached brittle target material. In the present study, we develop such a theory for two important systems, namely the axisymmetric core-cladding system and the plane-strain film-substrate system, to understand the underlying mechanisms and key control parameters for the controlled fragmentation induced by necking. It is revealed that controlled fragmentation is facilitated by a reversal shear lag effect which results in a peak tension in the target material near the necking zone. The peak tension moving with neck propagation produces the sequential fragmentation, instead of random fracture expected in a conventional shear lag model. Furthermore, the fragmentation size is shown to depend on the interfacial shear strength, as well as the feature size and stiffness of the target material. Our theory suggests potential approaches to reducing the size of fragmented components via increasing interfacial interaction and decreasing geometrical dimensions such as the core radius or film thickness. This insight may guide the development of a technological platform for large-scale manufacturing of structures in the nanoscale.

4.4 Necking-Affected Shear Lag Models

We develop axisymmetric and plane-strain cold drawing models for two systems: a circular fiber with concentric core-cladding structure, and a thin film supported by a substrate, as shown in Figs. 4.2 and 4.3, respectively. The fiber core and the thin film are both linear elastic materials with brittle fracture behavior characterized by the tensile strength σ_s, while the cladding and substrate are ductile materials that are prone to necking under drawing. For the sake of simplicity, the radius of the brittle core is assumed to remain constant and the change in thickness of the thin film is also neglected in our analysis. The theory of

controlled fragmentation for the axisymmetric core-cladding system will be introduced in detail, and then extended to the film-substrate system.

Without loss of generality, we assume that the neck propagation is in steady state, with a fully formed neck after the necking front. Fragmentation in otherwise scenarios will be discussed later. Since no relative interfacial displacement can be identified far ahead of the necking front in the unnecked region, the infinitely long models can be truncated to the point in the vicinity of which the two solids are well bonded. The cross-section of the core or thin film is free from loading at the end corresponding to the position of the last fragmentation.

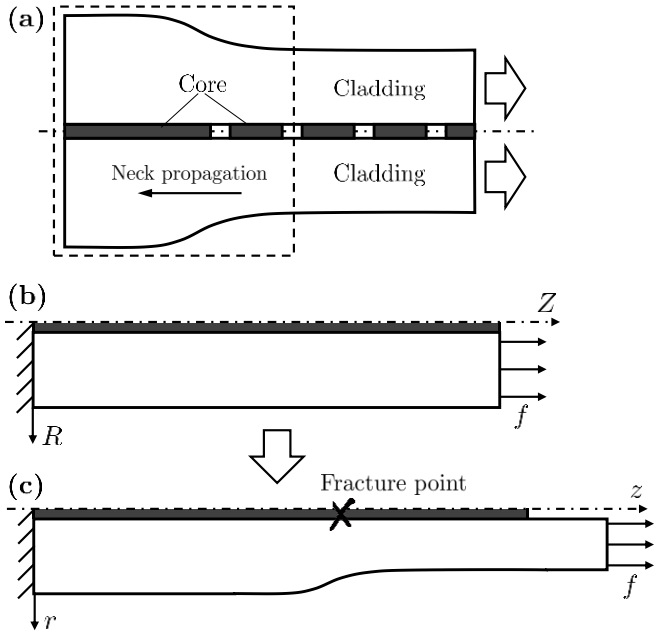

Fig. 4.2. Cold-drawing of a core-cladding circular fiber system. (**a**) Fragmentation of the fiber core near the necking zone in the cladding. The dashed rectangle shows the part on which the axisymmetric cold drawing model is based. (**b-c**) The initial and deformed configurations of the core-cladding system.

In our model, shear sliding is allowed along the interface, and interfacial shear stress τ^{int} is assumed to follow a rigid-perfectly plastic constitutive law which, in the case of a very thin core or film, behaves approximately as

$$\tau^{\mathrm{int}} = \begin{cases} 0, & |\delta| = 0, \\ \dfrac{\delta}{|\delta|}\tau_0, & |\delta| > 0, \end{cases} \tag{4.1}$$

where δ is the relative interfacial sliding, and τ_0 the interfacial shear strength.

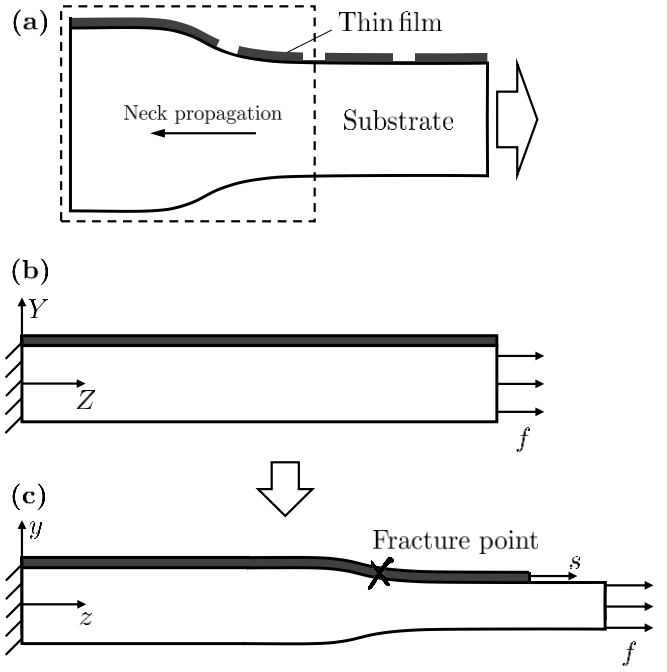

Fig. 4.3. Cold-drawing of a film-substrate system. (**a**) Fragmentation of the thin film near the necking zone in the substrate. The dashed rectangle shows the part on which the plane-strain cold drawing model is based. (**b-c**) The initial and deformed configurations of the film-substrate system.

4.4.1 Deformation of Ductile Cladding/Substrate

In steady-state necking of an incompressible, nonlinearly elastic solid, the cladding in the fiber system and the substrate in the thin film system can be divided into a necked region with uniform stretch λ^{u} and an unnecked region with uniform stretch λ^{n}, connected by a

transition zone. Although a homogeneous solid requires the true stress-strain constitutive curve to be increasing monotonically before ultimate failure, the engineering stress-strain curve could present a local maximum near the onset of necking. The latter will then exhibit an upturn induced by increasing hardening (Fig. 4.4), which forces the necking state to propagate toward the unnecked region.

Under quasi-static uniaxial drawing, the necking state taking incompressibility condition into account can be described by [165, 166, 168]:

$$\tilde{\sigma}(\lambda^{\mathrm{n}} - \lambda^{\mathrm{u}}) = U^{\mathrm{n}} - U^{\mathrm{u}}, \tag{4.2}$$

where $\tilde{\sigma}$ denotes the engineering stress or nominal stress in the necking material, and U^{n} and U^{u} are strain energy densities in the necked and unnecked regions, respectively, with

$$U = \int_1^{\lambda} \tilde{\sigma}\, \mathrm{d}\lambda. \tag{4.3}$$

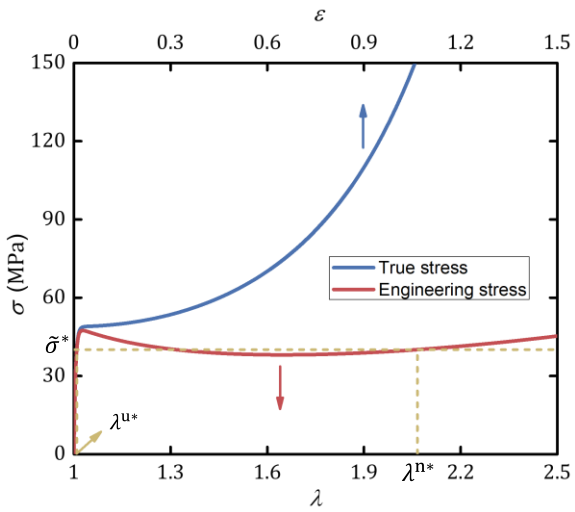

Fig. 4.4. Constitutive relation of an example material subject to ductile necking.

The true stress-strain constitutive relation of a nonlinear elastic polymeric material, for example, can take the form [169]:

$$\sigma = k\left[1 - \exp\left(-\frac{\varepsilon}{\varepsilon_v}\right)\right]\exp(h\varepsilon^2), \tag{4.4}$$

where k, h, and ε_v are material constants, and the values $k = 48.93\text{MPa}$, $h = 1.0$ and $\varepsilon_v = 0.05$ are used in the numerical examples below. By inserting the relationships $\sigma = \lambda\tilde{\sigma}$ and $\varepsilon = \ln\lambda$ into Eq. (4.4) we obtain the corresponding form of the constitutive law in terms of engineering stress and stretch. With this form, the engineering stress $\tilde{\sigma}^*$ and associated stretches $\lambda^{\mathrm{u}*}$ and $\lambda^{\mathrm{n}*}$ in steady-state neck propagation, as shown in Fig. 4.4, can be solved from Eqs. (4.2) and (4.3). For convenience, the superscript '*' will be omitted below.

The deformation state in the necking zone can be approximately obtained with the assumption that any cross-section in the necking material remains flat in the deformed configuration. Taking the core-cladding system as example, we note that the constant volume condition requires that for an infinitesimal portion of the core in the necking zone,

$$\pi(R_2^2 - R_1^2)\mathrm{d}\hat{Z} = \pi[(r_2^{\mathrm{t}})^2 - r_1^2]\left(\hat{\lambda}^{\mathrm{t}}\mathrm{d}\hat{Z}\right), \tag{4.5}$$

where R_1 and R_2 denote the inner and outer radii of the cladding in the initial configuration, respectively, whereas the corresponding lowercase letters denote quantities in the deformed configuration. As shown in Fig. 4.2b, c, $\hat{Z}$ and $\hat{z}$ are the positions of a point in the cladding in the initial and deformed configurations, respectively, with the superscript $'\mathrm{t}'$ denoting the transition zone and the hat accent referring to quantities associated with the cladding. Note that we have assumed that the core radius remains constant, i.e., $r_1 = R_1$. A modified expression based on the form due to Hutchinson and Neale [165] is adopted in the present work to describe the profile of a neck:

$$r_2^{\mathrm{t}}(Z) = \frac{r_2^{\mathrm{u}} + r_2^{\mathrm{n}}}{2} + \frac{r_2^{\mathrm{u}} - r_2^{\mathrm{n}}}{2} \tanh\left[-\frac{6}{l_{AB}}\left(Z - \frac{\hat{Z}_A + \hat{Z}_B}{2}\right)\right], \tag{4.6}$$

where $l_{AB} = \hat{Z}_B - \hat{Z}_A$ is the size of the necking zone AB shown in Fig. 4.5. In Eq. (4.6), r_2^{u} and r_2^{n} denote the deformed outer radii of the cladding in unnecked and necked regions, respectively, and can be obtained from the constant volume conditions in the corresponding regions:

$$r_2^{\mathrm{u}} = \sqrt{R_1^2 + \frac{R_2^2 - R_1^2}{\hat{\lambda}^{\mathrm{u}}}}, \qquad r_2^{\mathrm{n}} = \sqrt{R_1^2 + \frac{R_2^2 - R_1^2}{\hat{\lambda}^{\mathrm{n}}}}. \tag{4.7}$$

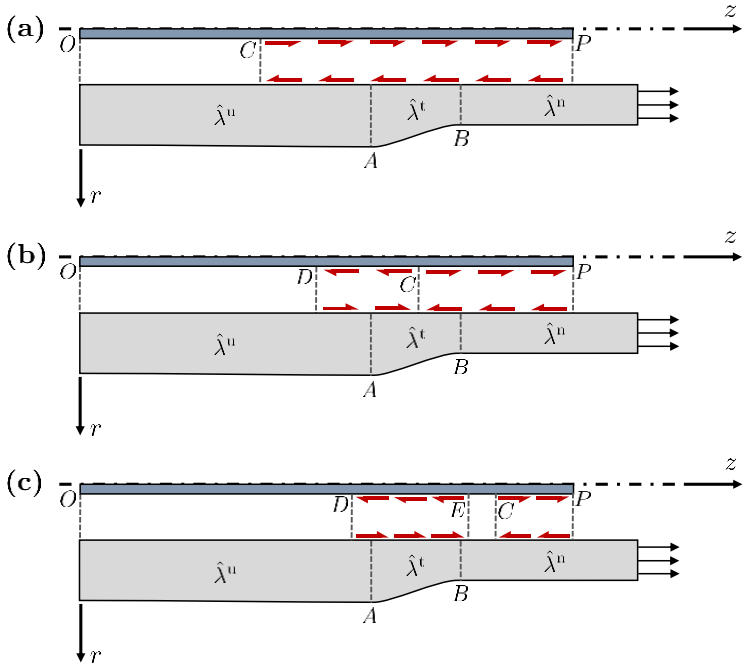

Fig. 4.5. Schematics of interfacial shear distributions (red arrows) in the core-cladding system for different values of the characteristic size l_{cc}. (**a**) The case of large l_{cc} with unnecked sticking zone OC and shear lag zone CP. (**b**) The case of intermediate l_{cc} with unnecked sticking zone OD, reversal shear lag zone DC and shear lag zone CP. (**c**) The case of small l_{cc} with unnecked sticking zone OD, reversal shear lag zone DE, necked sticking zone EC and shear lag zone CP. The dashed lines indicate the boundary of two adjacent zones or regions.

With the values of $\hat{\lambda}^{\mathrm{u}}$, $\hat{\lambda}^{\mathrm{n}}$ as well as Eqs. (4.5) and (4.6), the deformation of the cladding can be calculated as

$$\hat{z}(\hat{Z}) = \int_0^{\hat{Z}} \hat{\lambda}\, \mathrm{d}\hat{Z}. \tag{4.8}$$

In the present theory the deformation of the cladding is assumed to be free from the influence of interaction with the core, as the core is much thinner than the cladding. Nevertheless, the core-cladding interaction plays crucial roles in accumulating axial tension and inducing fracture in the core, which will be discussed later.

4.4.2 The Case of Large Characteristic Size

In the axisymmetric core-cladding fiber system, the drawing force is applied on the terminating cross-sections of the cladding, and tensile stress in the core is accumulated through interfacial shear, resembling a shear lag behavior. The interfacial shear distribution, however, could be different from that in the conventional shear lag model due to the presence of necking zone in the cladding. However, like in the conventional shear lag model, the interfacial deformation will decay far away from the loading end and necking zone. To estimate the size of the decay region of interfacial deformation, a characteristic size for the core-cladding fiber system can be defined as

$$l_{\mathrm{cc}} = \frac{R_1 E}{2\tau_0}, \tag{4.9}$$

where E is the Young's modulus of the core. Basically, the characteristic size l_{cc} is related to the overall stiffnesses of the core and the strength of interfacial interaction.

When the characteristic size l_{cc} is so large that the interfacial sliding zone spans over a range CP (Fig. 4.5a) which extends beyond the necking zone, the stress state in the core

can be described by the conventional shear lag model. For an infinitesimal portion of the core in the shear lag zone CP, we have

$$\mathrm{d}\sigma_z \cdot \pi r_1^2 = -\tau_0 \cdot 2\pi r_1 \mathrm{d}z, \tag{4.10}$$

where Z and z denote the positions of a point in the core in the initial and deformed configurations, respectively, and σ_z the Cauchy normal stress in the core in the axial direction. Since we have neglected the change in core radius after deformation, the Cauchy stress σ_z can be approximately replaced by the first Piola-Kirchhoff stress P_z. Therefore,

$$\mathrm{d}z = \lambda \mathrm{d}Z = \exp\left(\frac{P_z}{E}\right)\mathrm{d}Z, \tag{4.11}$$

where λ and ε_z are the stretch and axial true strain in the core, respectively. Combining Eqs. (4.10) and (4.11) and integrating the result in CP yield

$$\sigma_z = P_z = -E \ln\left(1 - \frac{L - Z}{l_{\mathrm{cc}}}\right), \tag{4.12}$$

where L denotes the length of the truncated fiber. The stretch in the core can be readily obtained as

$$\lambda = \left(1 - \frac{L - Z}{l_{\mathrm{cc}}}\right)^{-1}. \tag{4.13}$$

From Eq. (4.13), the stretch in the sliding zone of the core is zero at the end $Z = L$ and increases to the maximum at point C.

In the sticking zone OC, stress and stretch in the core remain constant since there is no interfacial shear transferring. Therefore, from continuity conditions of stress and deformation we obtain

$$\sigma_z = P_z = -E \ln\left(1 - \frac{L - Z_C}{l_{\mathrm{cc}}}\right), \tag{4.14}$$

$$\lambda = \left(1 - \frac{L - Z_C}{l_{\mathrm{cc}}}\right)^{-1} = \hat{\lambda}^{\mathrm{u}}. \tag{4.15}$$

Solving Eq. (4.15) yields

$$Z_C = L - \left(1 - \frac{1}{\hat{\lambda}^{\mathrm{u}}}\right) l_{\mathrm{cc}}. \tag{4.16}$$

With the use of Eqs. (4.13) and (4.15), the deformed configuration of the core can be calculated through

$$z(Z) = \int_0^Z \lambda \, \mathrm{d}Z. \tag{4.17}$$

Note that the point C must be in the unnecked region as any nonuniform deformation in the cladding is not allowed in the sticking zone OC with the use of interfacial constitutive law in Eq. (4.1). Consequently, the condition $Z_C \leq Z_A$ should be satisfied, resulting in

$$l_{\mathrm{cc}} \geq \frac{\hat{\lambda}^{\mathrm{u}}(L - Z_A)}{\hat{\lambda}^{\mathrm{u}} - 1}, \tag{4.18}$$

which gives a lower bound to the characteristic size l_{cc} associated with the interfacial distribution shown in Fig. 4.5a.

4.4.3 The Case of Intermediate Characteristic Size

It is easy to verify that the equality in Eq. (4.18) holds when point C moves to the boundary A, i.e., $Z_C = Z_A$, which means that the sticking zone coincides entirely with the unnecked region in the cladding. As l_{cc} decreases from the critical value in Eq. (4.18), the model will have no solution leading to interfacial shear distribution of the form in Fig. 4.5a. Instead, a "reversal shear lag" zone DC near the neck appears between the original sticking zone and sliding zone, as shown in Fig. 4.5b. Within the reversal shear lag zone DC, the direction of interfacial shear is opposite to that in the shear lag zone CP. The point D must be in the

unnecked region for the same reason as that associated with Eq. (4.18), and the constraint on the point C will be discussed below.

In the shear lag zone CP, the stress and stretch distributions are governed by the same equations as Eqs. (4.12) and (4.13). In the reversal shear lag zone DC, however, the equilibrium equation needs to be modified by changing the direction of interfacial shear in Eq. (4.10):

$$\mathrm{d}\sigma_z \cdot \pi r_1^2 = \tau_0 \cdot 2\pi r_1 \mathrm{d}z. \tag{4.19}$$

Combining Eqs. (4.10) and (4.19) and integrating the result in DC yield

$$\sigma_z = P_z = -E \ln\left(1 - \frac{L + Z - 2Z_C}{l_{\mathrm{cc}}}\right), \tag{4.20}$$

$$\lambda = \left(1 - \frac{L + Z - 2Z_C}{l_{\mathrm{cc}}}\right)^{-1}. \tag{4.21}$$

In the sticking zone OD, the stress and stretch are constant and can be determined based on continuity conditions of stress and deformation as

$$\sigma_z = P_z = -E \ln\left(1 - \frac{L + Z_D - 2Z_C}{l_{\mathrm{cc}}}\right), \tag{4.22}$$

$$\lambda = \left(1 - \frac{L + Z_D - 2Z_C}{l_{\mathrm{cc}}}\right)^{-1} = \hat{\lambda}^{\mathrm{u}}. \tag{4.23}$$

Solving Eq. (4.23) yields

$$Z_D = 2Z_C - L + \left(1 - \frac{1}{\hat{\lambda}^{\mathrm{u}}}\right) l_{\mathrm{cc}}. \tag{4.24}$$

With the use of Eqs. (4.13), (4.21) and (4.23), the deformed configuration of the core can be obtained through Eq. (4.17). Finally, the continuity condition of deformation on point C needs to be applied to determine the only unknown Z_C left, i.e.,

$$z(Z_C) = \hat{z}\left(\hat{Z}_C\right). \tag{4.25}$$

Note that point C is allowed to be located either in the necking zone AB or in the necked region of the cladding, depending on the value of the characteristic size l_{cc}.

The upper limit of l_{cc} can be obtained by the constraints $Z_D \le Z_A \le Z_C$ which lead to

$$l_{\mathrm{cc}} \le \frac{\hat{\lambda}^{\mathrm{u}}(L - Z_A)}{\hat{\lambda}^{\mathrm{u}} - 1}, \tag{4.26}$$

while the lower limit is determined by the constraint $\lambda(Z_C) \le \hat{\lambda}^{\mathrm{n}}$ which gives

$$l_{\mathrm{cc}} \ge l_{\mathrm{cc}}^{*}, \tag{4.27}$$

where l_{cc}^{*} is solved from Eq. (4.25) by inserting $Z_C = L - l_{\mathrm{cc}}\left(1 - 1/\hat{\lambda}^{\mathrm{n}}\right)$. Comparing Eqs. (4.18) and (4.26), we can find that the transition of interfacial shear distribution from Fig. 4.5a to Fig. 4.5b is continuous as the value of l_{cc} changes appropriately.

4.4.4 The Case of Small Characteristic Size

When the characteristic size l_{cc} continues to decrease from the critical value in Eq. (4.27), the model will have no solution leading to interfacial shear distribution of the form in Fig. 4.5b. In this case, another sticking zone EC will emerge in the necked region of the cladding, as shown in Fig. 4.5c, and is named as the necked sticking zone to be distinguished from the region OD, which we refer to as the unnecked sticking zone.

In the shear lag zone CP, the stress and stretch distributions are governed by the same equations as Eqs. (4.12) and (4.13). In the necked sticking zone EC, the stress and stretch are constant and can be determined based on continuity conditions of stress and deformation as

$$\sigma_z = P_z = -E \ln\left(1 - \frac{L - Z_C}{l_{\mathrm{cc}}}\right), \tag{4.28}$$

$$\lambda = \left(1 - \frac{L - Z_C}{l_{\mathrm{cc}}}\right)^{-1} = \hat{\lambda}^{\mathrm{n}}. \tag{4.29}$$

Solving Eq. (4.29) yields

$$Z_C = L - \left(1 - \frac{1}{\hat{\lambda}^{\mathrm{n}}}\right) l_{\mathrm{cc}}. \tag{4.30}$$

In the reversal shear lag zone DE, the equilibrium equation is the same as Eq. (4.19). Therefore, combining Eqs. (4.10) and (4.19) and integrating the result in DE yield

$$\sigma_z = P_z = -E \ln\left(1 + \frac{Z_C + Z_E - Z - L}{l_{\mathrm{cc}}}\right), \tag{4.31}$$

$$\lambda = \left(1 + \frac{Z_C + Z_E - Z - L}{l_{\mathrm{cc}}}\right)^{-1}. \tag{4.32}$$

In the unnecked sticking zone OD, the stress and stretch are constant and can be determined based on continuity conditions of stress and deformation as

$$\sigma_z = P_z = -E \ln\left(1 + \frac{Z_C + Z_E - Z_D - L}{l_{\mathrm{cc}}}\right), \tag{4.33}$$

$$\lambda = \left(1 + \frac{Z_C + Z_E - Z_D - L}{l_{\mathrm{cc}}}\right)^{-1} = \hat{\lambda}^{\mathrm{u}}. \tag{4.34}$$

Solving Eq. (4.34) yields

$$Z_D = Z_E - \left(\frac{1}{\hat{\lambda}^{\mathrm{u}}} - \frac{1}{\hat{\lambda}^{\mathrm{n}}}\right) l_{\mathrm{cc}}. \tag{4.35}$$

With the use of Eqs. (4.13), (4.29), (4.32) and (4.34), the deformed configuration of the core can be obtained through Eq. (4.17). Finally, the continuity condition of deformation on either point C or point E, i.e.,

$$z(Z_C) = \hat{z}\left(\hat{Z}_C\right) \text{ or } z(Z_E) = \hat{z}\left(\hat{Z}_E\right), \tag{4.36}$$

needs to be combined with Eq. (4.35) to determine the two unknowns Z_D and Z_E left.

For the interfacial shear distribution in Fig. 4.5c, it can be proven that the upper bound of l_{cc}^* is reached when the necked sticking zone is degenerated, i.e., $Z_C = Z_E$. By comparison with Eq. (4.27), it can be concluded that the transition of interfacial shear distribution

from Fig. 4.5b to Fig. 4.5c is continuous as the value of l_{cc} changes appropriately. Determining the lower bound, however, is a tricky task and can be done by numerical methods. It should be noted that, when the characteristic size l_{cc} is smaller than a critical value, no solution exists for this axisymmetric cold drawing problem with the use of the rigid-perfectly plastic interfacial constitutive law in Eq. (4.1). More sophisticated interfacial constitutive laws enable the model to enlarge effective spectrum of l_{cc} and thus expand the solution space, which will be discussed in subsection 4.5.3.

4.4.5 Plane-Strain Film-Substrate Model

The plane-strain film-substrate system bears essential similarities to the axisymmetric core-cladding system in the senses that necking occurs in the ductile material and load is transmitted through interfacial shear. Yet, in the film-substrate system necking may influence the interface and result in deformation of the interface in the normal direction (Fig. 4.3), different from the case in core-cladding system where the interface always remains straight. Therefore, to better describe the configuration of the thin film and deformation of the interface, we adopt a curved axis s along the midplane of the deformed thin film in the plane-strain model, as shown in Fig. 4.3c.

For an incompressible, nonlinear elastic material, the constant volume condition applied to an infinitesimal portion of the substrate in the necking zone requires

$$2T_2 \mathrm{d}\hat{Z} = 2t_2^{\mathrm{t}}\left(\hat{\lambda}^{\mathrm{t}}\mathrm{d}\hat{Z}\right), \tag{4.37}$$

where T_2 and t_2 denote the half thicknesses of the substrate in the initial and deformed configurations, respectively. The superscript $'\mathrm{t}'$ denotes the transition zone and the hat accent refers to quantities associated with the substrate. Note that the width of the substrate

is assumed to be unity in the plane-strain model. Similar to Eq. (4.6), the deformed half thickness of the substrate can be expressed as

$$t_2^{\mathrm{t}}(Z) = \frac{t_2^{\mathrm{u}} + t_2^{\mathrm{n}}}{2} + \frac{t_2^{\mathrm{u}} - t_2^{\mathrm{n}}}{2} \tanh\left[-\frac{6}{l_{AB}}\left(\hat{Z} - \frac{\hat{Z}_A + \hat{Z}_B}{2}\right)\right], \tag{4.38}$$

where t_2^{u} and t_2^{n} are the deformed half thicknesses of the substrate in the unnecked and necked regions, respectively, and can be obtained from volume constant conditions, in analogy to Eq. (4.37), in corresponding regions as

$$t_2^{\mathrm{u}} = \frac{T_2}{\hat{\lambda}^{\mathrm{u}}}, \qquad t_2^{\mathrm{n}} = \frac{T_2}{\hat{\lambda}^{\mathrm{n}}}. \tag{4.39}$$

To calculate interfacial displacement on the deformed interface, it is necessary to map the position of points on the substrate surface to the curved axis s of the thin film:

$$\hat{s}(\hat{Z}) = \int_0^{\hat{Z}} \frac{\mathrm{d}\hat{s}}{\mathrm{d}\hat{Z}}\,\mathrm{d}\hat{Z} = \int_0^{\hat{Z}} \sqrt{\left(\frac{\mathrm{d}\hat{z}}{\mathrm{d}\hat{Z}}\right)^2 + \left(\frac{\mathrm{d}t_2^{\mathrm{t}}}{\mathrm{d}\hat{Z}}\right)^2}\,\mathrm{d}\hat{Z}, \tag{4.40}$$

where $\mathrm{d}\hat{z}/\mathrm{d}\hat{Z} = \hat{\lambda}$ is the stretch in the substrate.

The film thickness is assumed to be so small that the bending effect due to out-of-plane deformation in the necking zone can be neglected. Therefore, a characteristic size in the plane-strain film-substrate model, like that in the core-cladding model, can be defined as

$$l_{\mathrm{fs}} = \frac{T_1 E}{\tau_0}, \tag{4.41}$$

where T_1 and E denote the initial thickness and Young's modulus of the thin film, respectively. Analytical solutions to the film-substrate system cold drawing problem are similar in forms to those in subsections 4.4.2-4.4.4, and details in the results are provided in Appendix A.

4.5 Results and Discussion

4.5.1 Strength-Governed Controlled Fragmentation

Typically, the controlled fragmentation technique is applied to the pair of brittle core and ductile cladding in the core-cladding system, and the pair of brittle thin film and ductile substrate in the film-substrate system. Considering the micro- and even nano-scale feature sizes of the core/thin film, the fracture process is likely governed by the material strength because of the flaw tolerance effect [170-172]. In the conventional shear lag model where the maximum tension is reached within a wide region, the fracture position is random and non-deterministic. This is also the situation for cold drawing models of the core-cladding and film-substrate systems with large characteristic size, as shown in Fig. 4.6a.

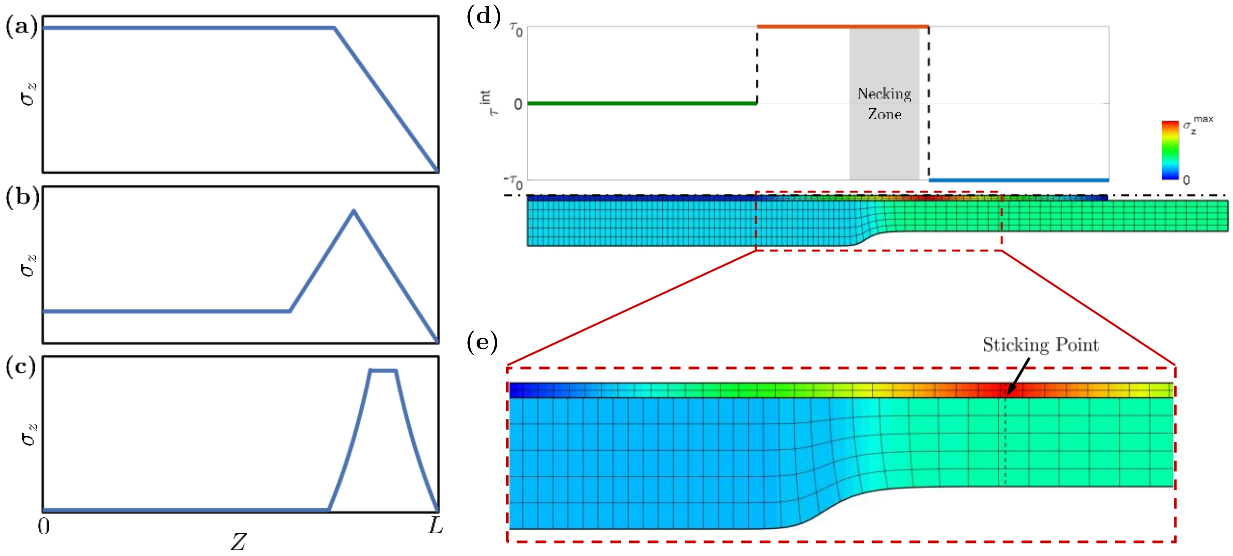

Fig. 4.6. Results of axial tension in the core from the cold drawing theory. (**a-c**) Example axial tension distributions in the core for (a) large l_{cc}, (**b**) intermediate l_{cc} and (**c**) small l_{cc}. (**d**) Distributions of interfacial shear (the upper) and axial tension (the lower) in the deformed configuration with intermediate l_{cc}. (**e**) The enlarged view of the parts near the necking zone showing the peak tension on the sticking point.

However, when the characteristic size is intermediate, there exists a peak tension in the core/thin film near the neck (Fig. 4.6b). The presence of the peak tension is attributed to the reversal shear lag effect discussed in subsection 4.4.2 and marks the most dangerous position in the target material to fracture. We may take the deformed configuration of the core-cladding system (Fig. 4.6d, e) as example to better understand the underlying mechanism. According to the stress solutions Eqs. (4.12), (4.20) and (4.22), the peak tension occurs at the junction of the shear lag and reversal shear lag zones, which is a sticking point. On the right side of the sticking point, the cladding has a larger deformation and moves toward the right relative to the core; whereas on the left side of the sticking point, the cladding accumulates less displacement due to the unnecked region and moves toward the left relative to the core. The core on the sticking point is therefore stretched toward the two sides, inducing peak tension therein. It should be noted that, the position of the peak tension is not necessarily in the necking zone, but can also occur in the necked region (e.g., in Fig. 4.6d, e, the necking zone boundary is at $Z = 70$ while the peak tension is at $Z = 71.22$). In the latter case, the distance to the necking zone is associated with the difference of deformation in the necked and unnecked regions. Basically, a large deformation difference makes the positions of peak tension and resulting fragmentation close to the necking zone, which was also observed in experiment [140, 144].

Furthermore, the deformation difference in the necked and unnecked regions of the cladding is responsible for the reduction of tension in the reversal shear lag zone. If the stretch in necked region $\hat{\lambda}^{\mathrm{n}}$ approaches that in unnecked region $\hat{\lambda}^{\mathrm{u}}$, the distributions of interfacial shear and axial tension will degenerate to those predicted by the conventional shear lag model.

The position of the peak tension moves with the necking front, and the tension value also increases due to the accumulation through interfacial shear in the enlarged necked region. Finally, the core will fracture once the peak tension reaches the material strength of the core. Upon continuing loading on the cladding, the fracture process repeats, and sequential fragmentation can be obtained.

For the cold drawing systems with relatively small characteristic size, the reversal shear lag effect still holds. However, between the shear lag and reversal shear lag zones arises the necked sticking zone where the tension is maximum over the core, as shown in Fig. 4.6c. Like the case with large characteristic size, the fracture position locates in the necked sticking zone and is non-deterministic. Nevertheless, the fragmentation size can be bounded from above by the sum of lengths of the necked sticking and shear lag zones.

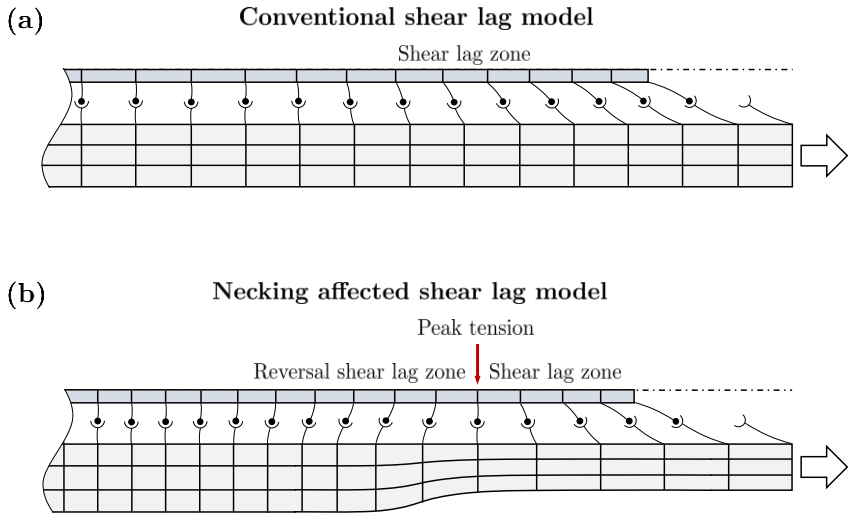

Fig. 4.7. Schematic illustration of (**a**) unnecked and (**b**) necked core-cladding systems with intermediate characteristic size. The interfacial spacing is exaggerated to show interfacial deformation. The arrow in (**b**) indicates the position of peak tension in the core.

Therefore, in the core-cladding system without necking (Fig. 4.7a), the deformation of the cladding is never less than that of the core, and interfacial deformation is governed by a single shear lag zone. As aforementioned, the tension in the shear lag zone keeps increasing as the distance to the loading end, and then saturates and forms a plateau which is wide in size for slender systems. Small inclusions or slight nonuniform distribution of defects in the core will lead to random fracture when the plateau tension reaches the material strength. Uncontrolled fragmentation will continue to happen in the previously fractured components under ongoing loading. In contrast, the simultaneous presence of a shear lag and a reversal shear lag zones in the system with necking (Fig. 4.7b) produces a tension peak around which the interfacial forces are "drawing" the core toward two sides. In the reversal shear lag zone, the core has a larger deformation compared with the cladding, originating from the drastic deformation change of the necking material around the neck. The reversal shear lag effect changes the increasing trend of tensile stress in the shear lag zone, preventing the formation of a tension plateau as in the conventional shear lag model and facilitating the controlled fragmentation.

4.5.2 Determination of Fragmentation Size

Based on the results on tensile stress distribution in the target materials, only the fragmentation sizes in cold drawing systems with intermediate characteristic sizes are deterministic. For given strength of the core or thin film material, σ_{s}, the position of the peak tension (i.e., the point C in Fig. 4.5b) can be solved from Eq. (4.25) and the fragmentation size can be calculated as

$$l_{\mathrm{frag}} = L - Z_C. \tag{4.42}$$

For convenience, we still take the core-cladding system as example in the following. In fact, if Eqs. (4.26) and (4.27) for l_{cc} have been satisfied, the fragmentation size can also be obtained by directly solving $\sigma_z(Z_C) = \sigma_{\mathrm{s}}$ from Eq. (4.12), which yields

$$l_{\mathrm{frag}} = l_{\mathrm{cc}}\left[1 - \exp\left(-\frac{\sigma_{\mathrm{s}}}{E}\right)\right]. \tag{4.43}$$

For brittle materials, the value of σ_{s}/E is a small number, so Eq. (4.43) can be approximated by

$$l_{\mathrm{frag}} \approx l_{\mathrm{cc}}\frac{\sigma_s}{E}\left(1 - \frac{\sigma_s}{2E}\right). \tag{4.44}$$

Eqs. (4.43) and (4.44) imply that the fragmentation size is proportional to the characteristic size when stiffness and strength of the core material are given. Considering the form of l_{cc} in Eq. (4.9), this suggests that the fragmentation size can be reduced via increasing interfacial interaction and decreasing the core radius. On the other hand, Eq. (4.44) can be rewritten as

$$l_{\mathrm{frag}} \approx \frac{R_1\sigma_s}{2\tau_0}\left(1 - \frac{\sigma_s}{2E}\right), \tag{4.45}$$

from which we can see that core materials with lower stiffness also facilitate smaller fragmentation size obtained by cold drawing. It might be inefficient, however, to change the fragmentation size using the effect of material modulus, as the value of $\sigma_s/(2E)$ is usually much smaller than 1 in experiment.

To validate the cold drawing theory developed in this work, we implemented finite element (FE) simulations in Abaqus to compare with the analytical results. Three sets of numerical examples were considered for both the core-cladding and film-substrate systems. In the core-cladding system, for example, we changed the interfacial shear strength (Set 1), core radius (Set 2) and Young's modulus of the core (Set 3), respectively, while kept the

other parameters unchanged in each set. In all examples, the user subroutine UINTER provided by Abaqus was used to apply the rigid-perfectly plastic interfacial constitutive law in Eq. (4.1). Tensile strengths of the core material and thin film material were assumed as $\sigma_s^{\text{core}} = 1.5$ GPa and $\sigma_s^{\text{film}} = 30$ GPa, respectively. Other relevant parameters used in theoretical calculation and FE simulations are listed in Table 4.1.

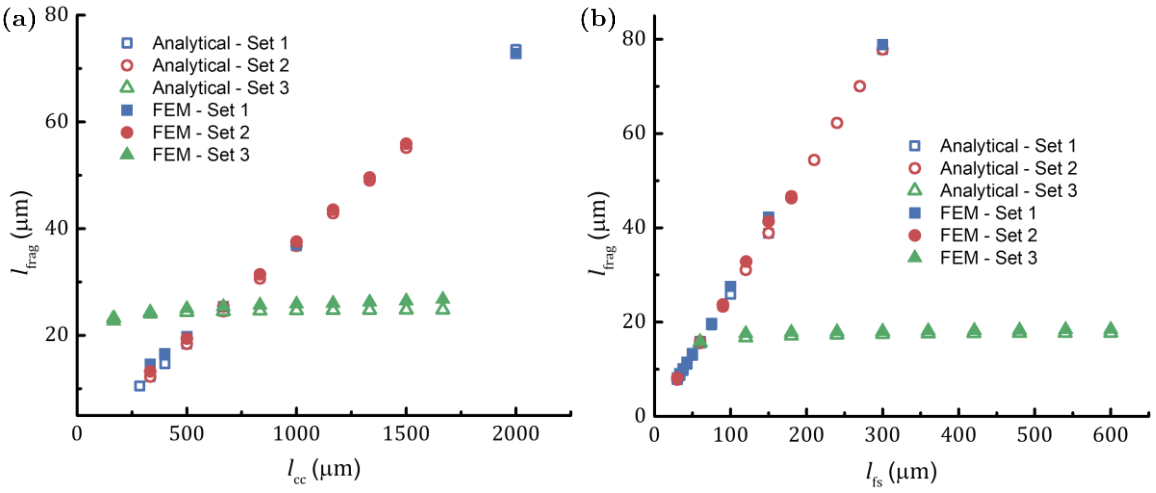

Fig. 4.8. Dependence of fragmentation size on characteristic sizes in the (**a**) core-cladding and (**b**) film-substrate systems with intermediate l_{cc} and l_{fs}.

The fragmentation sizes predicted by the cold drawing theory show excellent fit with FE results, as shown in Fig. 4.8. With the same stiffness and strength of the core material in Sets 1 and Sets 2, the fragmentation size turns out to be linear in l_{cc} for the core-cladding system, and in l_{fs} for the film-substrate system, consistent with the approximate solution in Eq. (4.44). For Sets 3, although the values of l_{cc} and l_{fs} change proportionally with Young's moduli of the core and thin film, respectively, the fragmentation size remains almost the same due to the insensitivity to material modulus predicted by Eq. (4.45).

Table 4.1. Relevant parameters adopted in the numerical examples.

Core-cladding	Set 1	Set 2	Set 3	Film-substrate	Set 1	Set 2	Set 3
τ_0 (MPa)	/	30	30	τ_0 (MPa)	/	0.1	0.1
R_1 (μm)	1.0	/	1.0	T_1 (nm)	0.3	/	0.6
E (GPa)	40	40	/	E (GPa)	100	100	/
R_2 (μm)	10	10	10	T_2 (μm)	50	50	50
L (μm)	160	160	160	L (μm)	1000	1000	1000
σ_s (GPa)	1.5	1.5	1.5	σ_s (GPa)	30	30	30

The corresponding forms of Eqs. (4.44) and (4.45) for the film-substrate system should read as

$$l_{\text{frag}} \approx l_{\text{fs}} \frac{\sigma_s}{E}\left(1-\frac{\sigma_s}{2E}\right) = \frac{T_1\sigma_s}{\tau_0}\left(1-\frac{\sigma_s}{2E}\right). \tag{4.46}$$

Therefore, the fragmentation size in the film-substrate system can be reduced effectively by increasing interfacial interaction between the thin film and substrate and decreasing the film thickness.

In practical applications, in order to reduce fragmentation size toward the nanoscale, one choice is decreasing the core radius in core-cladding system or the film thickness in film-substrate system by improving sample preparation techniques. On the other hand, interfacial shear strength can be enhanced through at least two strategies to obtain smaller rods and ribbons. For the film-substrate system, one can select polymer substrates having stronger adhesion with the film, or use surface treatment techniques to attach functional groups or create surface patterns on the polymer substrates to alter adhesion with the film. Similar techniques could be used on the core-cladding system as well.

4.5.3 Effect of Interfacial Interaction Models

In this subsection, we will briefly discuss the effect of different interfacial interaction models from the rigid-perfectly plastic one in Eq. (4.1). The interfacial interaction is usually governed by a linear elastic law when the interfacial sliding is small. In the cases where large sliding in included, the linear elastic law can be replaced by an elastic-perfectly plastic version (inset in Fig. 4.9), which can approximate the linear elastic law by a very narrow elastic stage and approximate the rigid-perfectly plastic law by a very wide elastic stage. In this elastic-plastic law, the shear strength τ_0 is reached at the interface when the interfacial shear displacement is δ_0.

Fig. 4.9 shows the FE simulation results for the film-substrate system with different values of δ_0. Specifically, the case with $\delta_0 = 0$ corresponds to the rigid-perfectly plastic constitutive law described in Eq. (4.1). The results show that interfacial interactions with reasonable portion of elasticity do not essentially influence the linear scaling of fragmentation size with the characteristic size. The three curves of different δ_0 in Fig. 4.9 possess slopes very close to each other, implying that the sensitivity of fragmentation size on the characteristic size is only related to interfacial and material properties and independent of the form of interfacial constitutive law. Compared to the rigid-perfectly plastic law, any elastic stage in the elastic-plastic law will basically weaken the interfacial interaction, leading to a larger fragmentation size under the same conditions.

For an elastic-plastic interfacial constitutive law, the interfacial shear distribution is continuously changing at junction points of two neighbor zones such as point C, D and E in Fig. 4.5. In this case, the analytical solution of the interfacial shear distribution to the cold drawing theory will be more sophisticated than the present one, for example, alternate

shear lag and reversal shear lag zones probably occur near the necking zone to accommodate rapid changes in interfacial deformation. This situation can become even more complicated if nonlinearity in the elastic stage or damage process is included in the interfacial constitutive law. Therefore, the present cold drawing model with the rigid-perfectly plastic constitutive law should be regarded as a low-order approximation to the problem, yet it can provide crucial insights for the controlled fragmentation in cold drawing.

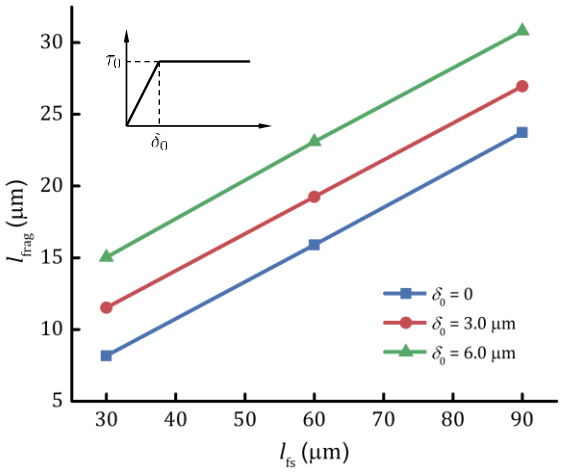

Fig. 4.9. Effect of interfacial sliding parameter δ_0 on fragmentation size in the film-substrate system with intermediate l_{fs}. The inset: the elastic-plastic interfacial constitutive law.

4.6 Summary

Graphene nanoribbons have tunable energy bandgap via ribbon width and can be potentially applied to flexible photovoltaics and electronics used for functional wearable devices. The necking-induced controlled fragmentation, achieved by the cold drawing of composite fiber or film-substrate system, is promising for the large-scale manufacturing of graphene nanoribbons. This manufacturing strategy was also found to be suitable for nanoribbons of other 2D materials.

In this study, the necking-affected shear lag models were developed for the cold drawing of the axisymmetric core-cladding fiber system and plane-strain film-substrate system, respectively. The models revealed how the fragmentations in the two systems occur in a controlled way upon cold drawing. For appropriate characteristic sizes determined by interfacial and target material properties, a reversal shear lag zone appears near the necking zone, resulting in a peak tension which increases with the neck propagation and induces fragmentation when the ultimate strength is reached. Our cold drawing models show that the fragmentation size should scale with a characteristic size for given material stiffness and strength, suggesting that feature size of the fragmented components can be reduced toward nanoscale via increasing interfacial interaction and decreasing geometrical dimensions such as the core radius or film thickness.

For the sake of simplicity, we have assumed in the cold drawing theory that the neck propagation has reached a steady state with a fully formed neck after the necking front. Under some conditions such as extremely strong interfacial interaction, however, the fragmentation size can be so small that the fragmentation happens before the loading end is fully necked. Nevertheless, in these cases sequential fragmentation behavior can still be induced by the peak tension due to the reversal shear lag effect. Another simplification in the theory is that constitutive relation of the ductile necking material is not considered directly in the system balance but affects the fragmentation size through stretches in the necked and unnecked regions. Accordingly, the effect of properties of the necking material, which could be of concern when the necking material can be replaced by alternatives or its mechanical properties tuned in experiment, cannot be seen explicitly and can only be studied numerically using the cold drawing theory.

Chapter 5 Conclusions and Perspectives

5.1 Concluding Remarks

The mechanics of 2D material thin films (including monolayer and multilayer films) was investigated in this dissertation for the potential applications in wearable devices. Specifically, the applications in aspects of health and nanofabrication technologies were focused. These studies help understand the behavior of 2D material thin films in different mechanical environments, the underlying mechanisms and the primary parameters influencing the performance of these films in practical applications.

In Chapter 1, the basic material properties, synthesis methods, characterization approaches and numerical tools for both monolayer and multilayer 2D material thin films were introduced. Monolayer films can be synthesized by top-down methods or bottom-up methods, while multilayer films, which are composed of large amount of interlocked monolayer nanosheets, are usually prepared from solutions/suspensions by drop-casting, spin-coating or vacuum filtration. The common approaches to characterizing 2D material thin films in experiment and corresponding modeling include uniaxial tension test, bulge test (blister test), membrane indentation test, lap shear test, peeling test, among others. These tests can be combined with established mathematical models to determine the film properties such as elastic modulus, strength, fracture energy, and interfacial properties. The numerical tools available for studies of 2D material thin films include atomistic simulations, phase field calculation and finite element methods.

In Chapter 2, the potential application of multilayer graphene-based thin films in mosquito bite prevention, featured by functional wearable devices, was explored. Both GO and

rGO thin films with thickness of 0.5~5.0μm were tested in dry and wet states through the live mosquito biting test. The two films in dry state serve as molecular barriers and protect the skin from mosquito bite effectively. In wet environment, however, the molecular barrier effect fails. The wet GO film, which has good breathability, converts to mechanically soft hydrogel and becomes nonprotective. However, the results from microneedle penetration test, micromechanical modeling and finite element simulation show that, the wet rGO film thicker than 0.5μm can act as mechanical barrier to resist mosquito bite.

In Chapter 3, the shear stability and interfacial failure behavior of GO and $MoSe_2$ thin films were studied considering the frequent shear loading exerted on the embedded films in wearable devices. The lap shear test was adopted to measure the critical shear force and fracture energy for GO and $MoSe_2$ adhesives. The mixed interfacial and cohesive failure mode was observed in both adhesives, indicating the presence of chaotic crack propagation paths which account for the extraordinary fracture energies of the multilayer films. This failure mode is also supported by the developed lap shear model with a pre-existing edge crack in the adhesive. The model also proposes a shear-to-tensile failure mode transition that occurs as the adhesive thickness and crack size change. This transition explains the different dependence of the critical shear force of GO and $MoSe_2$ films on film thickness, which turns out to result from the different dimensions of nanosheets and different edge crack sizes in the two films.

In Chapter 4, a necking-affected shear lag theory was developed for the controlled fragmentation of monolayer 2D material thin films to fabricate nanoribbons useful in developing flexible electronics in wearable devices. Based on this theory, an axisymmetric core-cladding fiber model and a plane-strain film-substrate model were developed to reveal the

mechanism through which the necking in the ductile material facilitates sequential fragmentation in the brittle material. It shows that a peak tension occurs in the brittle material near the neck due to the reversal shear lag effect. The peak tension, whose location moves with neck propagation, leads to the sequential fragmentation. Fragmentation size can be controlled by the interfacial interaction and geometrical dimensions of the brittle material such as the core radius or film thickness.

5.2 Future Works

The present studies focus on different 2D material thin films, from monolayer to multilayer, and cover different types of applications of the films, from health issues on mosquito bite prevention to nanofabrication technologies. However, some problems remain to be further investigated and solved.

For the graphene-based thin films with mosquito bite prevention, rGO in wet state can serve as mechanical barrier, but its breathability is poor due to the hydrophobicity and reduced interlayer spacing compared with GO. Therefore, the current rGO films need to be modified to increase the breathability while maintain or even enhance the mechanical strength. On the other hand, GO in wet state becomes mechanically soft to resist mosquito bite, yet it has excellent breathability. Considering the two problems, a possible solution is to keep the graphene nanosheets partially oxidized and apply crosslinking methods to strengthen the thin film.

The crosslinking methods dope some types of molecules, ions or microscopic components into 2D material thin films to form an interacted network. Basically, there are three crosslinking strategies for 2D material thin films. (1) Doping metal ions. A small amount

of divalent alkaline earth metal ions (Mg^{2+} and Ca^{2+}) can tightly bind to carboxylic acid groups at the edges of 2D nanosheets and effectively enhance the strength of the thin film [61, 173]. (2) Doping polymer molecules. Polymer can induce esterification reactions which create strong crosslinks between nanosheets. There are many options for polymer crosslinkers such as poly(vinyl alcohol) (PVA) [62] and polydopamine (PDA) [174, 175], among others [176-178]. An important parameter that influences crosslinking degree is the length of the polymer chain, as too short chains may not bridge adjacent nanosheets while too long chains cannot induce sufficient esterification [63]. (3) Doping one-dimensional (1D) materials. 1D materials (e.g., carbon nanotube, Ag nanowire, etc.) can be introduced to reinforce 2D materials through enhanced shear interaction and entanglement forces [64, 65, 179]. To obtain strong and breathable films, the appropriate crosslinking method still needs further investigation to be determined.

For the 2D material thin films under lap shear loading, the present study proposed a shear-to-tensile failure mode transition to reveal the dependence of critical shear force on film thickness and crack size. As the preliminary research on shear stability of multilayer 2D material thin films, the effect of different nanosheet sizes was only studied by preparing two types of 2D materials (GO and $MoSe_2$), rather than by changing the nanosheet sizes by experimental means for the same type of 2D material. The latter experiment scheme, if done appropriately, may provide more convincing evidence to support the transition theory.

For the controlled fragmentation induced by necking, the mechanism facilitated by the reversal shear lag effect may be also applied to other cold drawing systems, beyond the core-cladding and film-substrate systems, to produce micro- and nano- structures of diverse morphology. For example, fragmented tubular components can be hopefully obtained by

coating the target material on a fiber core, followed by preparing a core-coating-cladding sandwiched system, cold drawing the system and etching out the core and cladding. Compared with the simple core-cladding system, the sandwiched system needs more elaborate interface engineering to control the sequential fragmentation. In addition, cold drawing of multilayer thin film is a similar topic in the plane-strain system and has potential applications in fields such as preparation of nanoribbons of 2D heterostructure [113].

Appendix A Solutions to Film-Substrate Cold Drawing Model

Like the core-cladding model, the film-substrate model should also be discussed in three cases according to the value of the characteristic size l_{fs} defined in Eq. (4.41). The deformed configurations refer to those for the core-cladding system in Fig. 4.5, with the only difference that the film in the film-substrate system is curved and compliant to the necked substrate surface.

For the case of large characteristic size, the balance of an infinitesimal portion of the thin film in CP reads

$$\mathrm{d}\sigma_z \cdot t_1 = -\tau_0 \cdot \mathrm{d}s, \tag{A.1}$$

where t_1 denotes the deformed film thickness, and s the curved axis along the midplane of the deformed thin film. In the plane-strain model, the width of the thin film has been assumed to be unity. The solution can be obtained by combining Eqs. (A.1) and (4.11) as

$$\sigma_z = P_z = -E \ln\left(1 - \frac{L - Z}{l_{\mathrm{fs}}}\right), \qquad \lambda = \left(1 - \frac{L - Z}{l_{\mathrm{fs}}}\right)^{-1}. \tag{A.2}$$

In the sticking zone OC,

$$\sigma_z = P_z = -E \ln\left(1 - \frac{L - Z_C}{l_{\mathrm{fs}}}\right), \qquad \lambda = \left(1 - \frac{L - Z_C}{l_{\mathrm{fs}}}\right)^{-1}. \tag{A.3}$$

Then the continuity condition of deformation $\lambda_{OC} = \hat{\lambda}^{\mathrm{u}}$ yields

$$Z_C = L - \left(\frac{\hat{\lambda}^{\mathrm{u}} - 1}{\hat{\lambda}^{\mathrm{u}}}\right) l_{\mathrm{fs}}. \tag{A.4}$$

With the use of Eqs. (A.2) and (A.3), the deformed configuration of the thin film can be calculated through Eq. (4.17). In addition, the condition $Z_C \leq Z_A$ yields

$$l_{\mathrm{fs}} \geq \frac{\hat{\lambda}^{\mathrm{u}}(L - Z_A)}{\hat{\lambda}^{\mathrm{u}} - 1}. \tag{A.5}$$

For the case of intermediate characteristic size, solutions of stress and stretch distributions in the shear lag zone CP are the same as Eq. (A.2). In the reversal shear lag zone DC, with the condition $\mathrm{d}\sigma_z/\mathrm{d}s = \tau_0/t_1$ derived from the equilibrium, we can obtain

$$\sigma_z = P_z = -E \ln\left(1 - \frac{L + Z - 2Z_C}{l_{\mathrm{fs}}}\right), \qquad \lambda = \left(1 - \frac{L + Z - 2Z_C}{l_{\mathrm{fs}}}\right)^{-1}. \tag{A.6}$$

In the sticking zone OD,

$$\sigma_z = P_z = -E \ln\left(1 - \frac{L + Z - 2Z_C}{l_{\mathrm{fs}}}\right), \qquad \lambda = \left(1 - \frac{L + Z_D - 2Z_C}{l_{\mathrm{fs}}}\right)^{-1}. \tag{A.7}$$

The continuity condition of deformation $\lambda_{OD} = \hat{\lambda}^{\mathrm{u}}$ yields

$$Z_D = 2Z_C - L + \left(\frac{\hat{\lambda}^{\mathrm{u}} - 1}{\hat{\lambda}^{\mathrm{u}}}\right) l_{\mathrm{fs}}. \tag{A.8}$$

With the use of Eqs. (A.2), (A.6) and (A.7), the deformed configuration of the thin film can be calculated through Eq. (4.17). The only unknown Z_C left can be calculated by

$$s(Z_C) = \hat{s}\left(\hat{Z}_C\right), \tag{A.9}$$

where $\hat{s}$ is the coordinate of points on substrate surface in the curved axis s. The limits of the characteristic size can be obtained from the conditions $Z_D \leq Z_A \leq Z_C$ and $\lambda(Z_C) \leq \hat{\lambda}^{\mathrm{n}}$ as

$$l_{\mathrm{fs}}^{*} \leq l_{\mathrm{fs}} \leq \frac{\hat{\lambda}^{\mathrm{u}}(L - Z_A)}{\hat{\lambda}^{\mathrm{u}} - 1}, \tag{A.10}$$

where l_{fs}^{*} is solved from Eq. (A.9) by inserting $Z_C = L - l_{\mathrm{fs}}\left(1 - 1/\hat{\lambda}^{\mathrm{n}}\right)$.

For the case of small characteristic size, solutions of stress and stretch distributions in the shear lag zone CP are the same as Eq. (A.2). In the necked sticking zone EC,

$$\sigma_z = P_z = -E \ln\left(1 - \frac{L - Z_C}{l_{\mathrm{fs}}}\right), \qquad \lambda = \left(1 - \frac{L - Z_C}{l_{\mathrm{fs}}}\right)^{-1}. \tag{A.11}$$

The continuity condition of deformation $\lambda_{EC} = \hat{\lambda}^{\mathrm{n}}$ yields

$$Z_C = L - \left(1 - \frac{1}{\hat{\lambda}^{\mathrm{n}}}\right) l_{\mathrm{fs}}. \tag{A.12}$$

In the reversal shear lag zone DE,

$$\sigma_z = P_z = -E \ln\left(1 + \frac{Z_C + Z_E - Z - L}{l_{\mathrm{fs}}}\right), \tag{A.13a}$$

$$\lambda = \left(1 + \frac{Z_C + Z_E - Z - L}{l_{\mathrm{fs}}}\right)^{-1}. \tag{A.13b}$$

In the unnecked sticking zone OD,

$$\sigma_z = P_z = -E \ln\left(1 + \frac{Z_C + Z_E - Z_D - L}{l_{\mathrm{fs}}}\right), \tag{A.14a}$$

$$\lambda = \left(1 + \frac{Z_C + Z_E - Z_D - L}{l_{\mathrm{fs}}}\right)^{-1}. \tag{A.14b}$$

The continuity condition of deformation $\lambda_{OD} = \hat{\lambda}^{\mathrm{u}}$ yields

$$Z_D = Z_E - \left(\frac{1}{\hat{\lambda}^{\mathrm{u}}} - \frac{1}{\hat{\lambda}^{\mathrm{n}}}\right) l_{\mathrm{fs}}. \tag{A.15}$$

With the use of Eqs. (A.2), (A.11), (A.13) and (A.14), the deformed configuration of the thin film can be calculated through Eq. (4.17). The two unknowns Z_D and Z_E left need to be determined from the continuity condition of deformation

$$z(Z_C) = \hat{z}\left(\hat{Z}_C\right) \text{ or } z(Z_E) = \hat{z}\left(\hat{Z}_E\right), \tag{A.16}$$

together with Eq. (A.15). The upper limit of the characteristic size is

$$l_{\mathrm{fs}} \le l_{\mathrm{fs}}^{*}. \tag{A.17}$$

Bibliography

[1] Roduner, E. (2006). Size matters: why nanomaterials are different. *Chemical Society Reviews*, 35(7), 583-592.

[2] Bauer, J., Schroer, A., Schwaiger, R., & Kraft, O. (2016). Approaching theoretical strength in glassy carbon nanolattices. *Nature Materials*, 15(4), 438-443.

[3] Novoselov, K. S., Geim, A. K., Morozov, S. V., Jiang, D., Zhang, Y., Dubonos, S. V., ... & Firsov, A. A. (2004). Electric field effect in atomically thin carbon films. *Science*, 306(5696), 666-669.

[4] Novoselov, K. S., Geim, A. K., Morozov, S., Jiang, D., Katsnelson, M. I., Grigorieva, I., ... & Firsov, A. A. (2005). Two-dimensional gas of massless Dirac fermions in graphene. *Nature*, 438(7065), 197-200.

[5] Lee, C., Wei, X., Kysar, J. W., & Hone, J. (2008). Measurement of the elastic properties and intrinsic strength of monolayer graphene. *Science*, 321(5887), 385-388.

[6] Compton, O. C., & Nguyen, S. T. (2010). Graphene oxide, highly reduced graphene oxide, and graphene: versatile building blocks for carbon‐based materials. *Small*, 6(6), 711-723.

[7] Chhowalla, M., Shin, H. S., Eda, G., Li, L. J., Loh, K. P., & Zhang, H. (2013). The chemistry of two-dimensional layered transition metal dichalcogenide nanosheets. *Nature Chemistry*, 5(4), 263.

[8] Zhang, L., Xia, J., Zhao, Q., Liu, L., & Zhang, Z. (2010). Functional graphene oxide as a nanocarrier for controlled loading and targeted delivery of mixed anticancer drugs. *Small*, 6(4), 537-544.

[9] Zhang, T., Li, X., & Gao, H. (2015). Fracture of graphene: a review. *International Journal of Fracture*, 196(1-2), 1-31.

[10] Huang, J. Q., Zhuang, T. Z., Zhang, Q., Peng, H. J., Chen, C. M., & Wei, F. (2015). Permselective graphene oxide membrane for highly stable and anti-self-discharge lithium–sulfur batteries. *ACS Nano*, 9(3), 3002-3011.

[11] Anasori, B., Lukatskaya, M. R., & Gogotsi, Y. (2017). 2D metal carbides and nitrides (MXenes) for energy storage. *Nature Reviews Materials*, 2(2), 1-17.

[12] Jang, H., Park, Y. J., Chen, X., Das, T., Kim, M. S., & Ahn, J. H. (2016). Graphene‐based flexible and stretchable electronics. *Advanced Materials*, 28(22), 4184-4202.

[13] Chen, W., Chen, S., Qi, D. C., Gao, X. Y., & Wee, A. T. S. (2007). Surface transfer p-type doping of epitaxial graphene. *Journal of the American Chemical Society*, 129(34), 10418-10422.

[14] Cao, Y., Fatemi, V., Fang, S., Watanabe, K., Taniguchi, T., Kaxiras, E., & Jarillo-Herrero, P. (2018). Unconventional superconductivity in magic-angle graphene superlattices. *Nature*, 556(7699), 43-50.

[15] Nair, R. R., Wu, H. A., Jayaram, P. N., Grigorieva, I. V., & Geim, A. K. (2012). Unimpeded permeation of water through helium-leak–tight graphene-based membranes. *Science*, 335(6067), 442-444.

[16] Joshi, R. K., Carbone, P., Wang, F. C., Kravets, V. G., Su, Y., Grigorieva, I. V., ... & Nair, R. R. (2014). Precise and ultrafast molecular sieving through graphene oxide membranes. *Science*, 343(6172), 752-754.

[17] Chen, L., Shi, G., Shen, J., Peng, B., Zhang, B., Wang, Y., ... & Xu, G. (2017). Ion sieving in graphene oxide membranes via cationic control of interlayer spacing. *Nature*, 550(7676), 380-383.

[18] Dikin, D. A., Stankovich, S., Zimney, E. J., Piner, R. D., Dommett, G. H., Evmenenko, G., ... & Ruoff, R. S. (2007). Preparation and characterization of graphene oxide paper. *Nature*, 448(7152), 457-460.

[19] Lee, C., Wei, X., Li, Q., Carpick, R., Kysar, J. W., & Hone, J. (2009). Elastic and frictional properties of graphene. *Physica Status Solidi (b)*, 246(11-12), 2562-2567.

[20] Bistritzer, R., & MacDonald, A. H. (2011). Moiré bands in twisted double-layer graphene. *Proceedings of the National Academy of Sciences*, 108(30), 12233-12237.

[21] Castilho, C. J., Li, D., Liu, M., Liu, Y., Gao, H., & Hurt, R. H. (2019). Mosquito bite prevention through graphene barrier layers. *Proceedings of the National Academy of Sciences*, 116(37), 18304-18309.

[22] Naguib, M., Kurtoglu, M., Presser, V., Lu, J., Niu, J., Heon, M., ... & Barsoum, M. W. (2011). Two-dimensional nanocrystals produced by exfoliation of Ti_3AlC_2. *Advanced Materials*, 23(37), 4248-4253.

[23] Naguib, M., Come, J., Dyatkin, B., Presser, V., Taberna, P. L., Simon, P., ... & Gogotsi, Y. (2012). MXene: a promising transition metal carbide anode for lithium-ion batteries. *Electrochemistry Communications*, 16(1), 61-64.

[24] Shams, S. S., Zhang, R., & Zhu, J. (2015). Graphene synthesis: A review. *Materials Science-Poland*, 33(3), 566-578.

[25] Yan, Y., Nashath, F. Z., Chen, S., Manickam, S., Lim, S. S., Zhao, H., ... & Pang, C. H. (2020). Synthesis of graphene: Potential carbon precursors and approaches. *Nanotechnology Reviews*, 9(1), 1284-1314.

[26] Paton, K. R., Varrla, E., Backes, C., Smith, R. J., Khan, U., O'Neill, A., ... & Coleman, J. N. (2014). Scalable production of large quantities of defect-free few-layer graphene by shear exfoliation in liquids. *Nature Materials*, 13(6), 624-630..

[27] Hernandez, Y., Nicolosi, V., Lotya, M., Blighe, F. M., Sun, Z., De, S., ... & Coleman, J. N. (2008). High-yield production of graphene by liquid-phase exfoliation of graphite. *Nature Nanotechnology*, 3(9), 563-568.

[28] Nuvoli, D., Valentini, L., Alzari, V., Scognamillo, S., Bon, S. B., Piccinini, M., ... & Mariani, A. (2011). High concentration few-layer graphene sheets obtained by liquid phase exfoliation of graphite in ionic liquid. *Journal of Materials Chemistry*, 21(10), 3428-3431.

[29] Viculis, L. M., Mack, J. J., Mayer, O. M., Hahn, H. T., & Kaner, R. B. (2005). Intercalation and exfoliation routes to graphite nanoplatelets. *Journal of Materials Chemistry*, 15(9), 974-978.

[30] Cui, X., Zhang, C., Hao, R., & Hou, Y. (2011). Liquid-phase exfoliation, functionalization and applications of graphene. *Nanoscale*, 3(5), 2118-2126.

[31] Parvez, K., Li, R., Puniredd, S. R., Hernandez, Y., Hinkel, F., Wang, S., ... & Mullen, K. (2013). Electrochemically exfoliated graphene as solution-processable, highly conductive electrodes for organic electronics. *ACS Nano*, 7(4), 3598-3606.

[32] Abdolhosseinzadeh, S., Asgharzadeh, H., & Kim, H. S. (2015). Fast and fully-scalable synthesis of reduced graphene oxide. *Scientific Reports*, 5(1), 1-7.

[33] Alam, S. N., Sharma, N., & Kumar, L. (2017). Synthesis of graphene oxide (GO) by modified Hummers method and its thermal reduction to obtain reduced graphene oxide (rGO). *Graphene*, 6(1), 1-18.

[34] Choucair, M., Thordarson, P., & Stride, J. A. (2009). Gram-scale production of graphene based on solvothermal synthesis and sonication. *Nature Nanotechnology*, 4(1), 30.

[35] Kim, K. S., Zhao, Y., Jang, H., Lee, S. Y., Kim, J. M., Kim, K. S., ... & Hong, B. H. (2009). Large-scale pattern growth of graphene films for stretchable transparent electrodes. *Nature*, 457(7230), 706-710.

[36] Amini, S., Garay, J., Liu, G., Balandin, A. A., & Abbaschian, R. (2010). Growth of large-area graphene films from metal-carbon melts. *Journal of Applied Physics*, 108(9), 094321.

[37] Sutter, P. (2009). How silicon leaves the scene. *Nature Materials*, 8(3), 171-172.

[38] Mannix, A. J., Kiraly, B., Hersam, M. C., & Guisinger, N. P. (2017). Synthesis and chemistry of elemental 2D materials. *Nature Reviews Chemistry*, 1(2), 1-14.

[39] Meng, L., Wang, Y., Zhang, L., Du, S., Wu, R., Li, L., ... & Gao, H. J. (2013). Buckled silicene formation on Ir (111). *Nano Letters*, 13(2), 685-690.

[40] Zhou, J., Lin, J., Huang, X., Zhou, Y., Chen, Y., Xia, J., ... & Liu, Z. (2018). A library of atomically thin metal chalcogenides. *Nature*, 556(7701), 355-359.

[41] Ugeda, M. M., Bradley, A. J., Shi, S. F., Felipe, H., Zhang, Y., Qiu, D. Y., ... & Crommie, M. F. (2014). Giant bandgap renormalization and excitonic effects in a monolayer transition metal dichalcogenide semiconductor. *Nature Materials*, 13(12), 1091-1095.

[42] Shivayogimath, A., Thomsen, J. D., Mackenzie, D. M., Geisler, M., Stan, R. M., Holt, A. J., ... & Booth, T. J. (2019). A universal approach for the synthesis of two-dimensional binary compounds. *Nature Communications*, 10(1), 1-7.

[43] Pacile, D., Meyer, J. C., Girit, Ç. Ö., & Zettl, A. J. A. P. L. (2008). The two-dimensional phase of boron nitride: Few-atomic-layer sheets and suspended membranes. *Applied Physics Letters*, 92(13), 133107.

[44] Zhi, C., Bando, Y., Tang, C., Kuwahara, H., & Golberg, D. (2009). Large-scale fabrication of boron nitride nanosheets and their utilization in polymeric composites with improved thermal and mechanical properties. *Advanced Materials*, 21(28), 2889-2893.

[45] Park, J. H., Choi, S. H., Zhao, J., Song, S., Yang, W., Kim, S. M., ... & Lee, Y. H. (2016). Thickness-controlled multilayer hexagonal boron nitride film prepared by plasma-enhanced chemical vapor deposition. *Current Applied Physics*, 16(9), 1229-1235.

[46] Jang, A. R., Hong, S., Hyun, C., Yoon, S. I., Kim, G., Jeong, H. Y., ... & Shin, H. S. (2016). Wafer-scale and wrinkle-free epitaxial growth of single-orientated multilayer hexagonal boron nitride on sapphire. *Nano Letters*, 16(5), 3360-3366.

[47] Shifa, T. A., Wang, F., Liu, K., Xu, K., Wang, Z., Zhan, X., ... & He, J. (2016). Engineering the Electronic Structure of 2D WS_2 Nanosheets Using Co Incorporation as $Co_xW_{(1-x)}S_2$ for Conspicuously Enhanced Hydrogen Generation. *Small*, 12(28), 3802-3809.

[48] Karande, S. D., Kaushik, N., Narang, D. S., Late, D., & Lodha, S. (2016). Thickness tunable transport in alloyed WSSe field effect transistors. *Applied Physics Letters*, 109(14), 142101.

[49] Wang, X., Du, K., Liu, Y. Y. F., Hu, P., Zhang, J., Zhang, Q., ... & Xiong, Q. (2016). Raman spectroscopy of atomically thin two-dimensional magnetic iron phosphorus trisulfide ($FePS_3$) crystals. *2D Materials*, 3(3), 031009.

[50] Gogotsi, Y. (2015). Transition metal carbides go 2D. *Nature Materials*, 14(11), 1079-1080.

[51] Moon, I. K., Lee, J., Ruoff, R. S., & Lee, H. (2010). Reduced graphene oxide by chemical graphitization. *Nature Communications*, 1(1), 1-6.

[52] Zheng, J. C., Zhang, L., Kretinin, A. V., Morozov, S. V., Wang, Y. B., Wang, T., ... & Novoselov, K. S. (2016). High thermal conductivity of hexagonal boron nitride laminates. *2D Materials*, 3(1), 011004.

[53] Fu, L., Wang, T., Yu, J., Dai, W., Sun, H., Liu, Z., ... & Lin, C. T. (2017). An ultrathin high-performance heat spreader fabricated with hydroxylated boron nitride nanosheets. *2D Materials*, 4(2), 025047.

[54] Venugopal, G., Krishnamoorthy, K., Mohan, R., & Kim, S. J. (2012). An investigation of the electrical transport properties of graphene-oxide thin films. *Materials Chemistry and Physics*, 132(1), 29-33.

[55] Zhao, C., Xing, L., Xiang, J., Cui, L., Jiao, J., Sai, H., ... & Li, F. (2014). Formation of uniform reduced graphene oxide films on modified PET substrates using drop-casting method. *Particuology*, 17, 66-73.

[56] Watcharotone, S., Dikin, D. A., Stankovich, S., Piner, R., Jung, I., Dommett, G. H., ... & Ruoff, R. S. (2007). Graphene− silica composite thin films as transparent conductors. *Nano Letters*, 7(7), 1888-1892.

[57] Becerril, H. A., Mao, J., Liu, Z., Stoltenberg, R. M., Bao, Z., & Chen, Y. (2008). Evaluation of solution-processed reduced graphene oxide films as transparent conductors. *ACS Nano*, 2(3), 463-470.

[58] Eda, G., Fanchini, G., & Chhowalla, M. (2008). Large-area ultrathin films of reduced graphene oxide as a transparent and flexible electronic material. *Nature Nanotechnology*, 3(5), 270-274.

[59] Pham, V. H., Cuong, T. V., Hur, S. H., Shin, E. W., Kim, J. S., Chung, J. S., & Kim, E. J. (2010). Fast and simple fabrication of a large transparent chemically-converted graphene film by spray-coating. *Carbon*, 48(7), 1945-1951.

[60] Zhu, J., & He, J. (2012). Assembly and benign step-by-step post-treatment of oppositely charged reduced graphene oxides for transparent conductive thin films with multiple applications. *Nanoscale*, 4(11), 3558-3566.

[61] Park, S., Lee, K. S., Bozoklu, G., Cai, W., Nguyen, S. T., & Ruoff, R. S. (2008). Graphene oxide papers modified by divalent ions—enhancing mechanical properties via chemical cross-linking. *ACS Nano*, 2(3), 572-578.

[62] Huang, H. D., Ren, P. G., Chen, J., Zhang, W. Q., Ji, X., & Li, Z. M. (2012). High barrier graphene oxide nanosheet/poly (vinyl alcohol) nanocomposite films. *Journal of Membrane Science*, 409, 156-163.

[63] Jia, Z., & Wang, Y. (2015). Covalently crosslinked graphene oxide membranes by esterification reactions for ions separation. *Journal of Materials Chemistry A*, 3(8), 4405-4412.

[64] Hacopian, E. F., Yang, Y., Ni, B., Li, Y., Li, X., Chen, Q., ... & Lou, J. (2018). Toughening graphene by integrating carbon nanotubes. *ACS Nano*, 12(8), 7901-7910.

[65] Liu, B. T., & Kuo, H. L. (2013). Graphene/silver nanowire sandwich structures for transparent conductive films. *Carbon*, 63, 390-396.

[66] Zhang, P., Ma, L., Fan, F., Zeng, Z., Peng, C., Loya, P. E., ... & Lou, J. (2014). Fracture toughness of graphene. *Nature Communications*, 5(1), 1-7.

[67] Cao, K., Feng, S., Han, Y., Gao, L., Ly, T. H., Xu, Z., & Lu, Y. (2020). Elastic straining of freestanding monolayer graphene. *Nature Communications*, 11(1), 1-7.

[68] Cao, K., Yang, H., Gao, L., Han, Y., Feng, J., Yang, H., ... & Lu, Y. (2020). In situ mechanical characterization of silver nanowire/graphene hybrids films for flexible electronics. *International Journal of Smart and Nano Materials*, 11(3), 265-276.

[69] Li, P., Cao, K., Jiang, C., Xu, S., Gao, L., Xiao, X., & Lu, Y. (2019). In situ tensile fracturing of multilayer graphene nanosheets for their in-plane mechanical properties. *Nanotechnology*, 30(47), 475708.

[70] Koenig, S. P., Boddeti, N. G., Dunn, M. L., & Bunch, J. S. (2011). Ultrastrong adhesion of graphene membranes. *Nature Nanotechnology*, 6(9), 543.

[71] Bunch, J. S., Verbridge, S. S., Alden, J. S., Van Der Zande, A. M., Parpia, J. M., Craighead, H. G., & McEuen, P. L. (2008). Impermeable atomic membranes from graphene sheets. *Nano Letters*, 8(8), 2458-2462.

[72] Berry, V. (2013). Impermeability of graphene and its applications. *Carbon*, 62, 1-10.

[73] Boddeti, N. G., Liu, X., Long, R., Xiao, J., Bunch, J. S., & Dunn, M. L. (2013). Graphene blisters with switchable shapes controlled by pressure and adhesion. *Nano Letters*, 13(12), 6216-6221.

[74] Liu, X., Boddeti, N. G., Szpunar, M. R., Wang, L., Rodriguez, M. A., Long, R., ... & Bunch, J. S. (2013). Observation of pull-in instability in graphene membranes under interfacial forces. *Nano Letters*, 13(5), 2309-2313.

[75] Lloyd, D., Liu, X., Boddeti, N., Cantley, L., Long, R., Dunn, M. L., & Bunch, J. S. (2017). Adhesion, stiffness, and instability in atomically thin MoS_2 bubbles. *Nano Letters*, 17(9), 5329-5334.

[76] Wood, J. D., Harvey, C. M., & Wang, S. (2017). Adhesion toughness of multilayer graphene films. *Nature Communications*, 8(1), 1-7.

[77] Hencky, H. J. Z. M. P. (1915). Uber den Spannungszustand in kreisrunden Platten mit verschwindender Biegungssteifigkeit. *Zeitschrift fur Mathematik und Physik*, 63, 311-317.

[78] Bhatia, N. M., & Nachbar, W. (1968). Finite indentation of an elastic membrane by a spherical indenter. *International Journal of Non-Linear Mechanics*, 3(3), 307-324.

[79] Begley, M. R., & Mackin, T. J. (2004). Spherical indentation of freestanding circular thin films in the membrane regime. *Journal of the Mechanics and Physics of Solids*, 52(9), 2005-2023.

[80] Komaragiri, U., Begley, M. R., & Simmonds, J. G. (2005). The mechanical response of freestanding circular elastic films under point and pressure loads. *Journal of Applied Mechanics*, 72(2), 203-212.

[81] Vella, D., & Davidovitch, B. (2017). Indentation metrology of clamped, ultra-thin elastic sheets. *Soft Matter*, 13(11), 2264-2278.

[82] Jin, C., Davoodabadi, A., Li, J., Wang, Y., & Singler, T. (2017). Spherical indentation of a freestanding circular membrane revisited: analytical solutions and experiments. *Journal of the Mechanics and Physics of Solids*, 100, 85-102.

[83] Yang, W. H., & Hsu, K. H. (1971). Indentation of a circular membrane. *Journal of Applied Mechanics*, 227-230.

[84] Scott, O. N., Begley, M. R., Komaragiri, U., & Mackin, T. J. (2004). Indentation of freestanding circular elastomer films using spherical indenters. *Acta Materialia*, 52(16), 4877-4885.

[85] Frank, I. W., Tanenbaum, D. M., van der Zande, A. M., & McEuen, P. L. (2007). Mechanical properties of suspended graphene sheets. *Journal of Vacuum Science & Technology B*, 25(6), 2558-2561.

[86] Zhou, L., Wang, Y., & Cao, G. (2013). van der Waals effect on the nanoindentation response of free standing monolayer graphene. *Carbon*, 57, 357-362.

[87] Goland, M., & Reissner, E. (1944). The stresses in cemented joints. *Journal of Applied Mechanics*, 17-27.

[88] Hahn, K. (1961). Stress distribution in adherends of bonded lap joints. *Res. Report SM*, 40010.

[89] Hart-Smith, L. J. (1973). Adhesive-bonded single-lap joints. *National Aeronautics and Space Administration, Technical Report*.

[90] Tsai, M. Y., & Morton, J. (1994). A note on peel stresses in single-lap adhesive joints. *Journal of Applied Mechanics*, 61, 712-715.

[91] Peng, Y., & Deng, K. (2015). Study on the mechanical properties of the novel Sn–Bi/Graphene nanocomposite by finite element simulation. *Journal of Alloys and Compounds*, 625, 44-51.

[92] Salom, C., Prolongo, M. G., Toribio, A., Martínez-Martínez, A. J., de Cárcer, I. A., & Prolongo, S. G. (2018). Mechanical properties and adhesive behavior of epoxy-graphene nanocomposites. *International Journal of Adhesion and Adhesives*, 84, 119-125.

[93] Han, S., Meng, Q., Pan, X., Liu, T., Zhang, S., Wang, Y., ... & Araby, S. (2019). Synergistic effect of graphene and carbon nanotube on lap shear strength and electrical conductivity of epoxy adhesives. *Journal of Applied Polymer Science*, 136(42), 48056.

[94] Castilho, C. J., Li, D., Xie, Y., Gao, H., & Hurt, R. H. (2021). Shear failure in supported two-dimensional nanosheet van der Waals thin films. *Carbon*, 173, 410-418.

[95] Kendall, K. (1975). Thin-film peeling-the elastic term. *Journal of Physics D: Applied Physics*, 8(13), 1449.

[96] Kim, K. S., & Aravas, N. (1988). Elastoplastic analysis of the peel test. *International Journal of Solids and Structures*, 24(4), 417-435.

[97] Aravas, N., Kim, K. S., & Loukis, M. J. (1989). On the mechanics of adhesion testing of flexible films. *Materials Science and Engineering: A*, 107, 159-168.

[98] Roenbeck, M. R., Wei, X., Beese, A. M., Naraghi, M., Furmanchuk, A. O., Paci, J. T., ... & Espinosa, H. D. (2014). In situ scanning electron microscope peeling to quantify surface energy between multiwalled carbon nanotubes and graphene. *ACS Nano*, 8(1), 124-138.

[99] Fang, Z., Li, X., Shi, W., Li, Z., Guo, Y., Chen, Q., ... & Wei, X. (2020). Interlayer Binding Energy of Hexagonal MoS_2 as Determined by an In Situ Peeling-to-Fracture Method. *The Journal of Physical Chemistry C*, 124(42), 23419-23425.

[100] Rezaee, M., Tsai, L. C., Elyasigorji, A., Haider, M. I., Yazdi, A., & Salowitz, N. P. (2021). Quantification of the mechanical strength of thermally reduced graphene oxide layers on flexible substrates. *Engineering Fracture Mechanics*, 243, 107525.

[101] Choudhary, K., Kalish, I., Beams, R., & Tavazza, F. (2017). High-throughput identification and characterization of two-dimensional materials using density functional theory. *Scientific Reports*, 7(1), 1-16.

[102] Genoese, A., Genoese, A., Rizzi, N. L., & Salerno, G. (2019). Buckling analysis of single-layer graphene sheets using molecular mechanics. *Frontiers in Materials*, 6, 26.

[103] Zhang, J., Xu, F., Hong, Y., Xiong, Q., & Pan, J. (2015). A comprehensive review on the molecular dynamics simulation of the novel thermal properties of graphene. *RSC Advances*, 5(109), 89415-89426.

[104] Chen, L. Q. (2002). Phase-field models for microstructure evolution. *Annual Review of Materials Research*, 32(1), 113-140.

[105] Francfort, G. A., & Marigo, J. J. (1998). Revisiting brittle fracture as an energy minimization problem. *Journal of the Mechanics and Physics of Solids*, 46(8), 1319-1342.

[106] Bourdin, B., Francfort, G. A., & Marigo, J. J. (2000). Numerical experiments in revisited brittle fracture. *Journal of the Mechanics and Physics of Solids*, 48(4), 797-826.

[107] Meca, E., Lowengrub, J., Kim, H., Mattevi, C., & Shenoy, V. B. (2013). Epitaxial graphene growth and shape dynamics on copper: phase-field modeling and experiments. *Nano Letters*, 13(11), 5692-5697.

[108] Li, J., Ni, B., Zhang, T., & Gao, H. (2018). Phase field crystal modeling of grain boundary structures and growth in polycrystalline graphene. *Journal of the Mechanics and Physics of Solids*, 120, 36-48.

[109] Hansen-Dörr, A. C., Wilkens, L., Croy, A., Dianat, A., Cuniberti, G., & Kästner, M. (2019). Combined molecular dynamics and phase-field modelling of crack propagation in defective graphene. *Computational Materials Science*, 163, 117-126.

[110] Han, M. Y., Özyilmaz, B., Zhang, Y., & Kim, P. (2007). Energy band-gap engineering of graphene nanoribbons. *Physical Review Letters*, 98(20), 206805.

[111] Li, X., Wang, X., Zhang, L., Lee, S., & Dai, H. (2008). Chemically derived, ultrasmooth graphene nanoribbon semiconductors. *Science*, 319(5867), 1229-1232.

[112] Ruffieux, P., Cai, J., Plumb, N. C., Patthey, L., Prezzi, D., Ferretti, A., ... & Fasel, R. (2012). Electronic structure of atomically precise graphene nanoribbons. *ACS Nano*, 6(8), 6930-6935.

[113] Yunus, R. M., Endo, H., Tsuji, M., & Ago, H. (2015). Vertical heterostructures of MoS_2 and graphene nanoribbons grown by two-step chemical vapor deposition for high-gain photodetectors. *Physical Chemistry Chemical Physics*, 17(38), 25210-25215.

[114] Lundström, J. O. (1999). Mosquito-borne viruses in western Europe: A review. *Journal of Vector Ecology: Journal of the Society for Vector Ecology*, 24(1), 1-39.

[115] Teo, J., Tan, S. Y. Y., Liu, Y., Tay, M., Ding, Y., Li, Y., ... & Yang, L. (2014). Comparative genomic analysis of malaria mosquito vector-associated novel pathogen *Elizabethkingia anophelis*. *Genome Biology and Evolution*, 6(5), 1158-1165.

[116] McBride, C. S. (2016). Genes and odors underlying the recent evolution of mosquito preference for humans. *Current Biology*, 26(1), R41-R46.

[117] Hallem, E. A., Fox, A. N., Zwiebel, L. J., & Carlson, J. R. (2004). Mosquito receptor for human-sweat odorant. *Nature*, 427(6971), 212-213.

[118] Barnard, D. R. (2002). Chemical analysis of human skin emanations: comparison of volatiles from humans that differ in attraction of Aedes aegypti (Diptera: Culicidae). *Journal of the American Mosquito Control Association*, 8(3), 186-195.

[119] Weill, M., Lutfalla, G., Mogensen, K., Chandre, F., Berthomieu, A., Berticat, C., ... & Raymond, M. (2003). Insecticide resistance in mosquito vectors. *Nature*, 423(6936), 136-137.

[120] Hummers Jr, W. S., & Offeman, R. E. (1958). Preparation of graphitic oxide. *Journal of the American Chemical Society*, 80(6), 1339-1339.

[121] Spitz Steinberg, R., Cruz, M., Mahfouz, N. G., Qiu, Y., & Hurt, R. H. (2017). Breathable vapor toxicant barriers based on multilayer graphene oxide. *ACS Nano*, 11(6), 5670-5679.

[122] Lomax, G. R. (2007). Breathable polyurethane membranes for textile and related industries. *Journal of Materials Chemistry*, 17(27), 2775-2784.

[123] Pei, S., Zhao, J., Du, J., Ren, W., & Cheng, H. M. (2010). Direct reduction of graphene oxide films into highly conductive and flexible graphene films by hydrohalic acids. *Carbon*, 48(15), 4466-4474.

[124] Lin, X., Shen, X., Zheng, Q., Yousefi, N., Ye, L., Mai, Y. W., & Kim, J. K. (2012). Fabrication of highly-aligned, conductive, and strong graphene papers using ultralarge graphene oxide sheets. *ACS Nano*, 6(12), 10708-10719.

[125] Wang, C., Frogley, M. D., Cinque, G., Liu, L. Q., & Barber, A. H. (2013). Deformation and failure mechanisms in graphene oxide paper using in situ nanomechanical tensile testing. *Carbon*, 63, 471-477.

[126] Kong, X. Q., & Wu, C. W. (2009). Measurement and prediction of insertion force for the mosquito fascicle penetrating into human skin. *Journal of Bionic Engineering*, 6(2), 143-152.

[127] Ranjbartoreh, A. R., Wang, B., Shen, X., & Wang, G. (2011). Advanced mechanical properties of graphene paper. *Journal of Applied Physics*, 109(1), 014306.

[128] Ramasubramanian, M. K., Barham, O. M., & Swaminathan, V. (2008). Mechanics of a mosquito bite with applications to microneedle design. *Bioinspiration & Biomimetics*, 3(4), 046001.

[129] Wan, K. T., Guo, S., & Dillard, D. A. (2003). A theoretical and numerical study of a thin clamped circular film under an external load in the presence of a tensile residual stress. *Thin Solid Films*, 425(1-2), 150-162.

[130] Mostaani, E., Drummond, N. D., & Fal'Ko, V. I. (2015). Quantum Monte Carlo calculation of the binding energy of bilayer graphene. *Physical Review Letters*, 115(11), 115501.

[131] Tang, D. M., Kvashnin, D. G., Najmaei, S., Bando, Y., Kimoto, K., Koskinen, P., ... & Golberg, D. (2014). Nanomechanical cleavage of molybdenum disulphide atomic layers. *Nature Communications*, 5(1), 1-8.

[132] Cole, P. J., Cook, R. F., & Macosko, C. W. (2003). Adhesion between immiscible polymers correlated with interfacial entanglements. *Macromolecules*, 36(8), 2808-2815.

[133] Zhao, B., & Kwon, H. J. (2011). Adhesion of polymers in paper products from the macroscopic to molecular level—an overview. *Journal of Adhesion Science and Technology*, 25(6-7), 557-579.

[134] Wang, Z., von dem Bussche, A., Qiu, Y., Valentin, T. M., Gion, K., Kane, A. B., & Hurt, R. H. (2016). Chemical dissolution pathways of MoS2 nanosheets in biological and environmental media. *Environmental Science & Technology*, 50(13), 7208-7217.

[135] Griffith, A. A. (1921). VI. The phenomena of rupture and flow in solids. *Philosophical Transactions of the Royal Society of London. Series A*, 221(582-593), 163-198.

[136] Compton, O. C., Cranford, S. W., Putz, K. W., An, Z., Brinson, L. C., Buehler, M. J., & Nguyen, S. T. (2012). Tuning the mechanical properties of graphene oxide paper and its associated polymer nanocomposites by controlling cooperative intersheet hydrogen bonding. *ACS Nano*, 6(3), 2008-2019.

[137] Gao, W., & Huang, R. (2011). Effect of surface roughness on adhesion of graphene membranes. *Journal of Physics D: Applied Physics*, 44(45), 452001.

[138] Jiang, T., Huang, R., & Zhu, Y. (2014). Interfacial sliding and buckling of monolayer graphene on a stretchable substrate. *Advanced Functional Materials*, 24(3), 396-402.

[139] Ma, L., Wang, J., & Ding, F. (2013). Recent progress and challenges in graphene nanoribbon synthesis. *ChemPhysChem*, 14(1), 47-54.

[140] Shabahang, S., Tao, G., Kaufman, J. J., Qiao, Y., Wei, L., Bouchenot, T., ... & Abouraddy, A. F. (2016). Controlled fragmentation of multimaterial fibres and films via polymer cold-drawing. *Nature*, 534(7608), 529-533.

[141] Chen, M., Xia, J., Zhou, J., Zeng, Q., Li, K., Fujisawa, K., ... & Wei, L. (2017). Ordered and atomically perfect fragmentation of layered transition metal dichalcogenides via mechanical instabilities. *ACS Nano*, 11(9), 9191-9199.

[142] Xu, K., Wang, Z., Tan, C. F., Kang, N., Chen, L., Ren, L., ... & Hong, M. (2017). Uniaxially stretched flexible surface plasmon resonance film for versatile surface enhanced Raman scattering diagnostics. *ACS Applied Materials & Interfaces*, 9(31), 26341-26349.

[143] Li, K., Zhang, N., Zhang, T., Wang, Z., Chen, M., Wu, T., ... & Wei, L. (2018). Formation of ultra-flexible, conformal, and nano-patterned photonic surfaces via polymer cold-drawing. *Journal of Materials Chemistry C*, 6(17), 4649-4657.

[144] Chen, M., Wang, Z., Ge, X., Wang, Z., Fujisawa, K., Xia, J., ... & Wei, L. (2020). Controlled fragmentation of single-atom-thick polycrystalline graphene. *Matter*, 2(3), 666-679.

[145] Considère, M. (1885). Mémoire sur l'emploi du fer et de l'acier dans les constructions. *Vue Ch. Dunod*.

[146] Bridgman, P. W. (1943). The stress distribution at the neck of a tension specimen. *In 25th Annual Convention of the Society, Chicago*.

[147] Chen, W. H. (1971). Necking of a bar. *International Journal of Solids and Structures*, 7(7), 685-717.

[148] Needleman, A. (1972). A numerical study of necking in circular cylindrical bar. *Journal of the Mechanics and Physics of Solids*, 20(2), 111-127.

[149] Norris Jr, D. M., Moran, B., Scudder, J. K., & Quinones, D. F. (1978). A computer simulation of the tension test. *Journal of the Mechanics and Physics of Solids*, 26(1), 1-19.

[150] Hill, R. (1958). A general theory of uniqueness and stability in elastic-plastic solids. *Journal of the Mechanics and Physics of Solids*, 6(3), 236-249.

[151] Wesolowski, Z. (1963). The axially symmetric problem of stability loss of an elastic bar subject to tension. *Arch. Mech. Stos*, 15, 383-395.

[152] Cheng, S. Y., Ariaratnam, S. T., & Dubey, R. N. (1971). Axisymmetric bifurcation in an elastic-plastic cylinder under axial load and lateral hydrostatic pressure. *Quarterly of Applied Mathematics*, 29(1), 41-51.

[153] Miles, J. P. (1971). Bifurcation in plastic flow under uniaxial tension. *Journal of the Mechanics and Physics of Solids*, 19(2), 89-102.

[154] Hutchinson, J. W., & Miles, J. P. (1974). Bifurcation analysis of the onset of necking in an elastic/plastic cylinder under uniaxial tension. *Journal of the Mechanics and Physics of Solids*, 22(1), 61-71.

[155] Scherzinger, W., & Triantafyllidis, N. (1998). Asymptotic analysis of stability for prismatic solids under axial loads. *Journal of the Mechanics and Physics of Solids*, 46(6), 955-1007.

[156] Hill, R., & Hutchinson, J. W. (1975). Bifurcation phenomena in the plane tension test. *Journal of the Mechanics and Physics of Solids*, 23(4-5), 239-264.

[157] Triantafyllidis, N., Scherzinger, W. M., & Huang, H. J. (2007). Post-bifurcation equilibria in the plane-strain test of a hyperelastic rectangular block. *International Journal of Solids and Structures*, 44(11-12), 3700-3719.

[158] Stören, S., & Rice, J. R. (1975). Localized necking in thin sheets. *Journal of the Mechanics and Physics of Solids*, 23(6), 421-441.

[159] Antman, S. S. (1973). Nonuniqueness of equilibrium states for bars in tension. *Journal of Mathematical Analysis and Applications*, 44(2), 333-349.

[160] Owen, N. (1987). Existence and stability of necking deformations for nonlinearly elastic rods. *Archive for Rational Mechanics and Analysis*, 98(4), 357-383.

[161] Coleman, B. D., & Newman, D. C. (1988). On the rheology of cold drawing. I. Elastic materials. *Journal of Polymer Science Part B: Polymer Physics*, 26(9), 1801-1822.

[162] Mielke, A. (2006). Hamiltonian and Lagrangian flows on center manifolds: with applications to elliptic variational problems. *Springer*.

[163] Audoly, B., & Hutchinson, J. W. (2016). Analysis of necking based on a one-dimensional model. *Journal of the Mechanics and Physics of Solids*, 97, 68-91.

[164] Audoly, B., & Hutchinson, J. W. (2019). One-dimensional modeling of necking in rate-dependent materials. *Journal of the Mechanics and Physics of Solids*, 123, 149-171.

[165] Hutchinson, J. W., & Neale, K. W. (1983). Neck propagation. *Journal of the Mechanics and Physics of Solids*, 31(5), 405-426.

[166] Fager, L. O., & Bassani, J. L. (1986). Plane strain neck propagation. *International Journal of Solids and Structures*, 22(11), 1243-1257.

[167] Neale, K. W., & Tuğcu, P. (1985). Analysis of necking and neck propagation in polymeric materials. *Journal of the Mechanics and Physics of Solids*, 33(4), 323-337.

[168] Tuğcu, P., & Neale, K. W. (1987). Necking and neck propagation in polymeric materials under plane-strain tension. *International Journal of Solids and Structures*, 23(7), 1063-1085.

[169] G'sell, C., Aly-Helal, N. A., & Jonas, J. J. (1983). Effect of stress triaxiality on neck propagation during the tensile stretching of solid polymers. *Journal of Materials Science*, 18(6), 1731-1742.

[170] Gao, H., Ji, B., Jäger, I. L., Arzt, E., & Fratzl, P. (2003). Materials become insensitive to flaws at nanoscale: lessons from nature. *Proceedings of the National Academy of Sciences*, 100(10), 5597-5600.

[171] Gao, H., Wang, X., Yao, H., Gorb, S., & Arzt, E. (2005). Mechanics of hierarchical adhesion structures of geckos. *Mechanics of Materials*, 37(2-3), 275-285.

[172] Gao, H., & Chen, S. (2005). Flaw tolerance in a thin strip under tension. *Journal of Applied Mechanics*, 72, 732-737.

[173] Jiang, X., Ma, Y., Li, J., Fan, Q., & Huang, W. (2010). Self-assembly of reduced graphene oxide into three-dimensional architecture by divalent ion linkage. *The Journal of Physical Chemistry C*, 114(51), 22462-22465.

[174] Zhang, M., Mao, Y., Liu, G., Liu, G., Fan, Y., & Jin, W. (2020). Molecular bridges stabilize graphene oxide membranes in water. *Angewandte Chemie International Edition*, 59(4), 1689-1695.

[175] Tian, Y., Cao, Y., Wang, Y., Yang, W., & Feng, J. (2013). Realizing ultrahigh modulus and high strength of macroscopic graphene oxide papers through crosslinking of mussel‐inspired polymers. *Advanced Materials*, 25(21), 2980-2983.

[176] Shen, J., Liu, G., Huang, K., Jin, W., Lee, K. R., & Xu, N. (2015). Membranes with fast and selective gas‐transport channels of laminar graphene oxide for efficient CO_2 capture. *Angewandte Chemie*, 127(2), 588-592.

[177] Goh, K., Heising, J. K., Yuan, Y., Karahan, H. E., Wei, L., Zhai, S., ... & Chen, Y. (2016). Sandwich-architectured poly (lactic acid)–graphene composite food packaging films. *ACS Applied Materials & Interfaces*, 8(15), 9994-10004.

[178] Chang, T. H., Li, K., Yang, H., & Chen, P. Y. (2018). Multifunctionality and Mechanical Actuation of 2D Materials for Skin-Mimicking Capabilities. *Advanced Materials*, 30(47), 1802418.

[179] Yan, Z., Peng, Z., Casillas, G., Lin, J., Xiang, C., Zhou, H., ... & Tour, J. M. (2014). Rebar graphene. *ACS Nano*, 8(5), 5061-5068.